QUANTUM CONTROL OF CHARGE CARRIER DYNAMICS IN LAYERED SEMICONDUCTOR HETEROSTRUCTURES

By

KEVIN L. SHUFORD

A DISSERTATION PRESENTED TO THE GRADUATE SCHOOL
OF THE UNIVERSITY OF FLORIDA IN PARTIAL FULFILLMENT
OF THE REQUIREMENTS FOR THE DEGREE OF
DOCTOR OF PHILOSOPHY

UNIVERSITY OF FLORIDA

2003

Copyright 2003

by

Kevin L. Shuford

To my family

ACKNOWLEDGMENTS

I would like to begin by thanking the Department of Chemistry at the University of Florida for the opportunity to continue my education. In addition, I want to praise the Quantum Theory Project for creating such a wonderful working environment. This is a tight-knit group, where everyone contributes to the engaging atmosphere including Professors, Scientists, Post Docs, Staff, Students, and Student Assistants. I have learned an enormous amount from all, and have benefited greatly from being a part of it. I want to acknowledge my undergraduate research advisor, Dr. Michael Messina, for sparking my interest in theoretical Chemistry. His quick wit and unique personality are a pleasure to all who know him. I owe a huge amount of gratitude to my current research advisor, Dr. Jeffrey Krause. I thank him for his guidance, patience, and confidence in me. His keen scientific insight and pleasant demeanor have produced an enjoyable working relationship for the last 5 years. I also extend thanks to all of the current and past members of the Krause Group for their support and useful suggestions, especially Vladimir Malinovsky. I would like to thank the remaining members of my supervisory committee Dr. N. Yngve Öhrn, Dr. Erik Deumens, Dr. John Reynolds, and Dr. David Reitze.

Next, I acknowledge all of the people whose personal interactions have helped me navigate this journey. First and foremost, I thank my parents Charles and Cheryll Shuford for their constant support, guidance, and encouragement. I also thank my siblings Pamela Thompson and Jennifer Lucas and their families. I would like to acknowledge several close friends. I thank Mary Anita Morgan, David Whetstone, Joel Brantham, Mike Braswell, Deirdre Houston, and especially Robert James and his wife Keyra for their companionship and assistance throughout the years. I thank

all who compose my sizeable support base in Florida. Special thanks go to Edward and Sheila Crapo, as well as Edward and Whitney Augustine, for their unwavering acceptance and friendship through trying times. I would like to acknowledge Thomas Wood, Donna Ernest, and Dr. Tamir Ellis for putting up with me (I know it has not been easy). Lastly, I want to extend special thanks to Richard and Judith Parker for the hospitality, and numerous useful discussions.

The things that I have accomplished would not be possible without wonderful people surrounding me in both my personal life, and academic career. I appreciate them all, and am deeply thankful.

TABLE OF CONTENTS

page

ACKNOWLEDGMENTS iv

ABSTRACT viii

CHAPTER

1 INTRODUCTION 1

1.1 Controlling Dynamics with Laser Fields 1
1.2 Quantum Control 2
1.3 Nanostructures 3
1.4 Technological Importance and Applications 5
1.5 Control in the Solid State 6

2 OVERVIEW OF QUANTUM CONTROL 7

2.1 Tannor-Rice Method 7
2.2 Brumer-Shapiro Method 13
2.3 Optimal Control Theory 20
2.4 Local Control 26
2.5 Closed Loop Procedures 27
2.6 Stimulated Raman Adiabatic Passage 30
2.7 Other Molecular Control Objectives 36
2.8 Control in Semiconductors 38

3 PRELIMINARY STUDIES 43

3.1 Carrier States and Dynamics 43
3.2 Control Theory 48
3.3 Controlling Carriers in a Double Well 50
3.4 Tests of Robustness 52
3.5 Chirped Laser Pulses in a Superlattice 59
3.6 Conclusions 67

4 COULOMB EFFECTS 69

4.1 Theoretical Model 70
4.2 Test System 74
4.3 Dynamics in Complex Systems 74
4.4 Conclusions 80

5 TERAHERTZ EMISSION 83

5.1 Review of the Perturbative Solution 84
5.2 Tunable THz Emission 87
5.3 Signal Interference Effects 90
5.4 Applications for THz Emission 94
5.5 Conclusions 102

6 ADIABATIC PASSAGE 104

6.1 Methodology 106
6.2 Theoretical Considerations 107
6.3 Passage Between Quantum Wells 109
6.4 Conclusions 119

7 COULOMB EFFECTS REVISITED 121

7.1 New Exciton Model 121
7.2 Static Effects 125
7.3 Effects on Dynamics 130
7.4 Conclusions 136

8 CONCLUSIONS AND FUTURE WORK 138

APPENDIX

A QUANTUM WELL BASICS 143

B POPULATION INVERSION IN TWO-LEVEL SYSTEMS 145

C PROPAGATION METHODS 148

C.1 Second-Order Differencing 148
C.2 Split Operator Method 149

D GENETIC ALGORITHMS 150

E INTERBAND TRANSITIONS 152

F PULSE CHIRPING LIMITATIONS 155

REFERENCES 158

BIOGRAPHICAL SKETCH 168

Abstract of Dissertation Presented to the Graduate School
of the University of Florida in Partial Fulfillment of the
Requirements for the Degree of Doctor of Philosophy

QUANTUM CONTROL OF CHARGE CARRIER DYNAMICS IN LAYERED SEMICONDUCTOR HETEROSTRUCTURES

By

Kevin L. Shuford

August 2003

Chair: Jeffrey L. Krause
Major Department: Chemistry

This dissertation presents theoretical studies of charge carrier dynamics in layered semiconductor heterostructures. Carrier dynamics are investigated by solving the Schrödinger equation numerically on a grid. Control methods are used to discover laser pulses that actively manipulate and control dynamics in quantum well systems. Results indicate that a wide array of possible target objectives can be achieved successfully using simple, experimentally feasible electric fields.

A tailored laser pulse can drive an electronic wave packet to maximum overlap with a target distribution at a specified time. A genetic algorithm is used to determine the optimal parameters of the excitation pulse. The robustness of the results is analyzed by considering fluctuations in the dc field, two types of sample defects, and environmental coupling. In all cases studied, the genetic algorithm can re-optimize the laser field to achieve the control objective.

The effects of Coulomb interactions with regard to controlling wave packets in quantum wells are investigated. The goal is to clarify the extent that the attraction between electrons and holes affects control. The primary effect is to modify the energy splittings, which induces small changes in oscillation period and frequency of

the wave packet. The results show that the interaction does not substantially affect the control, yet can alter dynamics in some cases.

Quantum wells are sources of controllable radiation. Oscillating wave packets in the conduction band typically radiate in the Terahertz frequency regime. The frequency and amplitude of the radiation is tunable by altering excitation conditions. Terahertz fields can be designed by controlling the characteristics of the emission, and used as excitation sources for other applications.

Electronic population can be switched adiabatically between quantum wells. A time-dependent dc field guides an initial state along a smooth path to a target state. The general requirements for adiabaticity are determined. Successfully meeting the requirements produces a pure state that evolves adiabatically to the final state. This procedure provides an effective method for adiabatic passage with smooth transitions, selectivity, and reversibility.

CHAPTER 1
INTRODUCTION

1.1 Controlling Dynamics with Laser Fields

Dynamics can be defined as the study of motion with reference to the causes. This statement does not specify what is moving, how far it moves, or the time scale over which the movement occurs. Dynamics describes planetary motion occurring over days, an airplane flying through the sky over the course of hours, or a bullet fired from a gun taking only a fraction of a second. All of these objects are macroscopic, and hence their dynamics are readily observable. Very small bodies, such as molecular species, also display dynamics, though short time scales often make their observation difficult. Molecules are constantly translating, vibrating, and rotating over time scales of a trillionth of a second, or shorter. Only recently have experiments been able to observe the dynamics of molecules at this microscopic level in real time. Watching the interaction of molecular species with each other and the environment is an appealing idea. However, any scientist would like not only to observe, but to interpret the events, and to make accurate predictions. Perhaps the most gratifying scenario is to select a desired outcome, speculate how to achieve it, and alter the dynamics to accomplish this goal. Successfully achieving the goal demonstrates a detailed knowledge of the relevant possibilities, as well as a thorough understanding of the dynamical processes occurring.

A particularly interesting concept to a chemist is to control the products formed in reactions. Indeed, chemical synthesis accomplishes this general criterion, and throughout the years experimentalists have discovered numerous ways to yield almost any chemical species imaginable. This form of control relies heavily on statistical properties of a many-body system to push the reaction in a desired direction. The

particle interactions are mainly incoherent, and offer little knowledge of the system dynamics on a molecular level. Often, the mechanistic information is speculative, and a detailed understanding of the process cannot be achieved. An alternate approach is to control the molecular dynamics in a more active manner. For example, one could excite the system with an electric field to modify dynamics. This process allows the experimenter to vary the properties of the external perturbation, such as intensity and frequency, and greatly influence the effects on the system. The laser field creates well-defined phase relationships, and eliminates the randomness of incoherent interactions, largely reducing the statistical nature of the problem. This allows a wider range of control over the outcome, and gives a clear description of the dynamics involved. Laser fields furnish a unique opportunity to produce results that may normally be unattainable, such as driving a reaction product to high yield, or eliminating side reactions completely.

1.2 Quantum Control

A new field has emerged in the last 20 years known as quantum control. As the name implies, this field encompasses controlling dynamics on a level where quantum mechanics is applicable. Quantum control research uses external fields to alter system behavior in a coherent fashion. Problems are typically addressed in an inverse fashion. A target or goal is selected, and then one searches for the tailored electric field that drives the system to that control objective. Various methods are used to find the optimal laser fields including simple intuition, direct determination, constrained optimization procedures, and genetic search routines. All of these methods have had some success discovering fields that control system dynamics. In recent years, however genetic-style algorithms have dominated experimental work.

The earliest formal attempts at controlling molecular dynamics are located in the Russian literature in the 1970s.[1] Since then, chemists have become interested in the possibility of using laser fields to guide chemical reactions. In particular, suppression

or enhancement of product branching ratios has been a central theme. Initially, theoretical predictions proposing such schemes were met with heated opposition. Early experimental attempts at bond-selective chemistry were largely unsuccessful because of rapid energy redistribution, and were essentially expensive methods of heating molecules. However, in recent years, advances in laser technology have spurred a resurgence in the field. It is now possible to create intense, shaped laser pulses on a femtosecond time scale. In addition, experimental techniques such as phase locking allow well-defined phase relationships between pulses in a sequence. Armed with these highly advanced tools, experimentalists have been able to verify many of the theoretical predictions, and as a result have validated the field.

1.3 Nanostructures

Solid state research in nanostructures has received much attention in recent years, producing thousands of articles and books on the subject. A nanostructure is any system that has physical dimensions on the order of tens of nanometers (1 nm = 1 billionth of a meter). Structures of this size often exhibit properties consistent with their reduced dimensionality. The charge carriers are confined energetically by the material potentials, and respond differently than they would in three free dimensions. Nanostructures present some fundamental, dynamical effects not observed before their introduction. Quantum wells and superlattices are two closely related nanostructures that have been studied extensively.

A quantum well is created by growing a semiconductor layer between two layers of a different semiconductor. Typically, the two materials have similar lattice constants, and a significant difference in their band gaps. Because of the different energy gaps between valence and conduction bands, the charge carriers experience an effective potential resembling that of a square well in the growth direction. Perpendicular dimensions are engineered to be much larger than the growth dimension, and the carriers experience no potential from the material layers in these directions. This

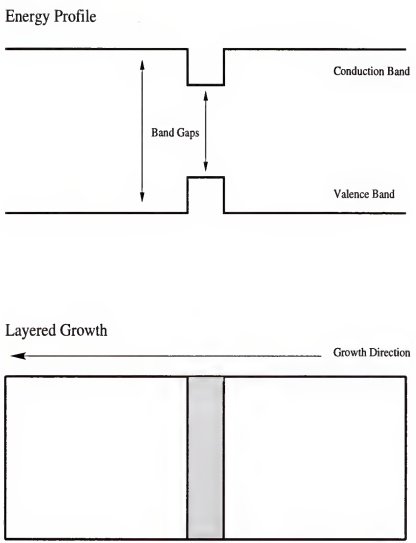

Figure 1–1: Cross section of a semiconductor heterostructure. The energy profile varies because of the layered growth of the materials. The shaded region corresponds to the material with the smaller band gap.

confines the charge carriers only in the growth direction, and leaves them essentially free in the perpendicular dimensions (Figure 1–1). It is currently possible to grow very thin material layers, and create quantum wells adjacent to each other. This structure is known as a double well. Adding several more quantum wells in a similar fashion leads to a more complicated structure called a superlattice. In such structures, a significant overlap exists between the wave functions in adjacent wells, and the characteristic energy levels typically group together into $N-$level minibands, where N is the number of wells in the system.

1.4 Technological Importance and Applications

The properties of quantum confined systems vary greatly from that of the bulk. Advances in laser technology coupled with improved sample quality has led to the experimental observation of numerous exotic effects. Some examples include resonant tunneling,[2,3] Stark localization,[4,5] coherent oscillations[6–9] leading to THz emission,[10–13] Fano resonances,[14] and Rabi oscillations.[15,16] These are impressive demonstrations of the ability to create and observe coherent, quantum mechanical effects in the solid state.

The phenomena exhibited by quantum-confined systems are of interest in both basic and applied research. These devices provide a medium to observe fundamental quantum mechanical concepts, and offer the potential for numerous applications. For example, carefully engineered structures have already been used as tunable emitters such as the Quantum Cascade Laser,[17] and detectors such as the Quantum Well Infrared Photodetector.[18,19] Possible applications for Terahertz emission include medical imaging, package inspection, and quality control,[20,21] while IR photodetectors have been used for environmental sensing useful for firefighting, volcanology, astronomy, and defense.[22] Other applications include ultrafast switches, which are imperative to advance the field of communications.[23,24] More speculative applications include using quantum well systems as registers for encoding and manipulating quantum information.[25,26] In fact, schemes using adiabatic passage to perform qubit rotation and quantum searches have been proposed recently.[27,28] As noted above, the observation of these exotic effects, and implementation in useful devices is quite significant. The development of the field could produce new devices, and improve existing ones such as modulating and switching devices, detectors, rectifiers, transistors, and quantum well lasers.

1.5 Control in the Solid State

To date, research in quantum control has primarily been demonstrated in the gas phase. However, several studies based on controlling dynamics in the solid state have been reported recently. Most of these works use the novel properties of quantum wells, wires, or dots. Quantum confined systems provide a unique opportunity because the sample dimensions and energy profile can be fabricated for a particular application (Appendix A). Existing experimental techniques such as Molecular Beam Epitaxy produce high-quality samples with great accuracy. Technological advances in semiconductor growth have achieved smoothing down to essentially the atomic scale. In addition, the composition of semiconductor materials can be adjusted to yield a desired energy profile. This allows one to customize the potential felt by charge carriers. In essence, structures can be designed to better accomplish a target objective.

Quantum confined systems are a logical area for research in quantum control. Solid state systems provide tests of existing molecular control methods, most of which assume long dephasing times prevalent in the gas phase. More research in the solid state encourages further developments in the field of quantum control, and increases the overall applicability of control methods to media other than gas. In addition, the current trend to miniaturize components of devices is not likely to change until the physical limitations of materials are reached. Future device design will no doubt use the unique properties of confined systems. Controlling carrier dynamics is a central theme in such devices, and quantum control research has previously developed methods to accomplish this task. Therefore both areas, quantum control and applied solid state science, would benefit from future research based on control in the solid state.

CHAPTER 2
OVERVIEW OF QUANTUM CONTROL

This chapter is an introduction to the fairly new field of quantum control. It is not meant to be an exhaustive review of all subjects researched in the past 20 years. The following sections cover many of the more notable control schemes, and provide numerous citations where further information can be obtained. Whenever possible, experimental results supporting the theoretical work are provided. Most of this chapter addresses atoms or molecules in the gas phase. However, Section 2.8 includes some recent examples of control in the solid state, specifically semiconductors.

2.1 Tannor-Rice Method

Early control methods are simply a matter of pulse timing. Several research groups have suggested using multiple laser pulses to achieve a desired result after attempts using a single laser field were largely unsuccessful. One of the first control methods attempted is a theoretical scheme proposed by Tannor and Rice.[29,30] The goal of their work is to control the branching ratio of a chemical reaction. The salient features of their methodology are described below.

The ground state potential energy surface representing the reaction has a central minimum, and two exit channels. It describes a stable reactant that can exit either channel, and form different products through reactions similar to

$$\mathrm{ABC} \rightarrow \mathrm{AB} + \mathrm{C} \qquad \text{and} \qquad \mathrm{ABC} \rightarrow \mathrm{A} + \mathrm{BC}. \tag{2.1}$$

The primary objective is to control the amount of one product relative to the other. In essence, the goal is to increase the probability that molecule ABC will choose a particular reaction pathway. Complete success of this task suppresses one product totally, and produces the other exclusively.

The Tannor-Rice method consists of using two laser pulses separated by a delay time. The two-photon procedure couples an excited state surface to the ground surface described previously. The delay time between pulses is varied to achieve product selectivity. The excited surface is chosen such that it contains certain desirable characteristics beneficial to the procedure. Specifically, it has a displaced energy minima, and coordinates rotated relative to the ground state surface. The Tannor-Rice scheme first excites the initial state to the excited surface with a short laser pulse. The promoted state is not an eigenstate on this surface, and begins to evolve according to the forces exerted upon it. At a later time, a second laser pulse sends the population back to the ground surface, where it can exit either channel, or remain confined in the bound region. The underlying concept of the pump-dump procedure is to time the laser pulses such that the wave packet on the excited surface is returned to the ground surface beyond any barriers that hinder the departure out of the desired reaction channel.

Control of the product ratio is achieved solely by varying the delay time between the laser pulses. Classical mechanics is used to interrogate the system, in hopes of finding a delay time that will achieve selectivity successfully. The authors state that Ehrenfast's theorem[31] and numerous works by Heller and co-workers[32–35] ensure that the quantum wave packet follows classical equations of motion for any potential, if the state remains sufficiently localized. Therefore, the less computationally intensive method of classical trajectories is used as a guide to determine the appropriate delay time between laser pulses for a quantum mechanical calculation. The procedure is as follows. A particle is placed on the excited surface directly above the minimum of the ground surface, and then allowed to evolve. After a time delay, the trajectory undergoes a vertical transition back to the ground surface conserving both position and momentum. The trajectory continues to evolve, either exiting a certain channel, oscillating in the minimum, or dissociating completely.

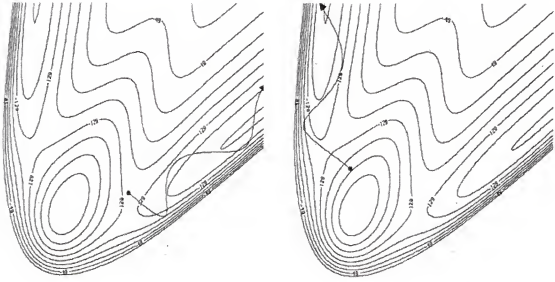

A B

Figure 2–1: Classical trajectories on the ground surface following a vertical transition from an excited surface. A) Trajectory exits from Channel 1; B) Trajectory exits from Channel 2. Reprinted with permission from D. J. TANNOR, R. KOSLOFF, AND S. A. RICE, J. CHEM. PHYS. **85**, 5805 (1986). Copyright 1986, American Institute of Physics.

Initial studies use a harmonic potential as the excited surface. Figure 2–1 shows examples of the particle evolution upon returning to the ground surface. This plot displays a contour plot of the surface, and the path of a classical particle. Panel A shows the particle exiting from Channel 1, while in Panel B the particle exits from Channel 2. The only difference in the simulated excitation conditions is the delay time between pulses. The trajectory in Panel B spends more time on the excited surface before being projected down. This allows the particle to land in an area on the ground surface that is favorable for exit Channel 2 rather than Channel 1. Figure 2–2 displays the probability of exit out of Channel 1 or 2 as a function of time. Note that the probabilities are step functions, and there is no overlap between them. The particle exits from either Channel 1 or 2, and at some times neither. The arrows indicate time periods when the classical trajectory favors a particular channel

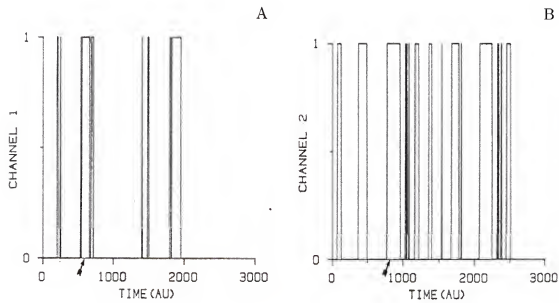

Figure 2–2: Probability a trajectory will exit from a certain channel. A) Exit probability from Channel 1; B) Exit probability from Channel 2. Arrows indicate time periods when a trajectory favors exit from a particular channel. Reprinted with permission from D. J. TANNOR, R. KOSLOFF, AND S. A. RICE, J. CHEM. PHYS. **85**, 5805 (1986). Copyright 1986, American Institute of Physics.

significantly. These delay times are used for the quantum mechanical calculation described below.

The fully-coupled quantum mechanical calculation uses the information gleaned from the classical trajectory method. The envelope of the laser pulses is adjusted to ensure complete population transfer between surfaces (Appendix B). The wave packet is propagated on a grid with a Second Order Differencing Method (Appendix C). The classical trajectory predicts 600 atomic units (au) to be a favorable delay time for exit from Channel 1. The wave packet dynamics using this delay time between pulses are shown in Figure 2–3. At 600 au the wave packet density is returned to the ground surface, and later exits out of Channel 1. Not all of the density exits, however the very large percentage that does follows the path predicted by the classical trajectory. A delay time of 825 au sends the wave packet out of exit Channel 2 as shown in Figure 2–4. Again, nearly all of the wave packet leaves the desired channel, and

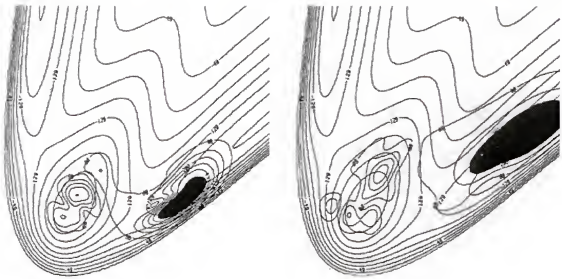

A B

Figure 2–3: Ground state surface and wave packet dynamics. A) $t = 800$ au; B) $t = 1000$ au. Filled areas represent regions where most of the wave packet is localized. The wave packet follows the classical trajectory, and exits from Channel 1. Reprinted with permission from D. J. TANNOR, R. KOSLOFF, AND S. A. RICE, J. CHEM. PHYS. **85**, 5805 (1986). Copyright 1986, American Institute of Physics.

follows the classical trajectory. These results indicate complete control of selectivity, and validate the use of classical trajectories as a predictive tool for these conditions.

Tannor and Rice have also studied the effects on selectivity with different excited state potential surfaces. As mentioned previously, they find that when using a harmonic potential as the intermediate, essentially 100% selectivity of product formation can be achieved. More complex potentials substantially decrease the performance. This is attributed to a failure of the classical trajectory to predict wave packet motion accurately on anharmonic excited states. In many cases, the wave packet spreads significantly, and hence is not adequately represented by a single classical trajectory. To find the correct pulse sequence in these instances, ensembles of classical trajectories are run to compare more directly with quantum results. While some differences in dynamics are revealed, the branching ratios show definite similarities. The authors conclude that the correspondence is not perfect, however classical trajectories are a

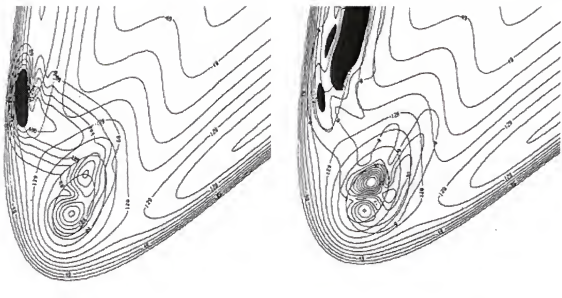

A B

Figure 2–4: Ground state surface and wave packet dynamics. A) $t = 1000$ au; B) $t = 1200$ au. Filled areas represent regions where most of the wave packet is localized. The wave packet follows the classical trajectory, and exits from Channel 2. Reprinted with permission from D. J. TANNOR, R. KOSLOFF, AND S. A. RICE, J. CHEM. PHYS. **85**, 5805 (1986). Copyright 1986, American Institute of Physics.

useful predictive tool, and in all cases at least some selectivity is attainable using the Tannor-Rice method.

Several experiments have used variations of the Tannor-Rice method to control product formation. They are not direct reproductions, but do use multiple pulses and the delay time between them as the means of control. Gerber and co-workers[36] have shown that a two-photon procedure can alter the ratio of product formation between Na^+ and Na_2^+. The initial Na_2 state is localized in the ground surface potential well. This state is excited by the pump laser pulse to an excited double-well potential creating a coherent superposition of vibrational states. The laser frequency excites population high enough on the potential curve such that the wave packet can traverse the double-well barrier. After a selected time delay, a probe pulse excites the wave packet to both the ionic ground state, which produces Na_2^+, and to a dissociative state, which produces Na^+. The major product is Na_2^+. However, when the wave

packet is allowed to move to the outer turning point on the double-well potential, the amount of Na^+ is doubled. The product ratio is altered by the pump-probe delay time and the position of the vibrational wave packet. Gerber and co-workers[37] have also developed a three-photon procedure to control the products. This process uses different intermediate states and laser frequencies, yet produces similar results.

Nobel Prize winner Ahmed Zewail is a leader in ultrafast spectroscopy and method development. He and co-workers have also performed experiments using timing methods to control product formations. In one example, Zewail et al.[38] use a pulse sequence to control the amount of product formed in the bimolecular reaction

$$Xe + I_2 \rightarrow XeI + I. \tag{2.2}$$

The delay time between two laser pulses affects the yield of XeI. The pump pulse creates a wave packet of vibrational levels on the B state of molecular I_2. The superposition state oscillates on the excited curve until a probe pulse further excites it to a higher lying state. The probe pulse excites population above the reaction threshold, and creates the product when the wave packet is located spatially at the outer turning point. Because of the oscillation on the B state of Iodine, a modulation of product yield is observed. The chemiluminescence signal originating from the XeI product is most intense when the wave packet is at a point that corresponds to the appropriate internuclear separation. The wave packet position and the delay time between pulses control the yield of a certain product. Zewail and co-workers[39] have also studied the NaI system. Again, they show that a well-timed pulse sequence can alter the product yield.

2.2 Brumer-Shapiro Method

Brumer and Shapiro have developed a control scheme based on interference effects using continuous wave (CW) lasers. Their goal, similar to that of Tannor and Rice, is to control the product formation in unimolecular reactions. The scheme

excites a molecule above the dissociation limit to an energy E, where it fragments into several possible channels. Therefore, there exists a set of degenerate continuum eigenstates, which each correlate to a particular product species. The underlying theme is to create multiple pathways from an initial state to the same final state. For example, two coherent paths occurring simultaneously have a total probability of the form

$$|A_1|^2 + |A_2|^2 + 2\mathrm{Re}\left(A_1^* A_2\right), \tag{2.3}$$

where A_i is the probability amplitude in path i. The first two terms are independent of each other. The cross term describes the interference between two competing pathways. This is analogous to the Young double-slit experiment, in which the interference between beams creates regions of reduced and enhanced probability of observation. Brumer and Shapiro suggest using the interference term to control the probability of exit from a certain product channel. In particular, they show that it is possible to enhance a preselected product state of a chemical reaction by manipulating the relative intensities and phases of the lasers.

Brumer and Shapiro have refined several schemes in a perturbative framework to create the interference necessary for control. Some of their early work investigates the photodissociation of CH_3I.[40,41] The relevant product channels are

$$CH_3I \rightarrow CH_3 + I\ (^2P_{3/2}) \qquad \text{and} \qquad CH_3I \rightarrow CH_3 + I^*\ (^2P_{1/2}). \tag{2.4}$$

A two-state wave packet on the ground surface is chosen as the initial state. The superposition state is excited simultaneously by two lasers. The laser frequencies are chosen to match the resonant transition from each component eigenstate of the wave packet to a predetermined energy above the dissociation barrier. Using a wave packet as the initial state creates the two pathways needed to control product formation. The Schrödinger equation supplies an expression for the probability of exit from a particular product channel. In the case of two products, the product formation ratio

is the probability of exit from Channel 1 divided by the probability of exit from Channel 2. Brumer and Shapiro find that reaction control is possible by adjusting the amplitudes of the excitation lasers, and thus varying the composition of the initial wave packet. Essentially all of the product formed can be directed to desired channel by altering only these variables.

A more celebrated Brumer-Shapiro control scheme[42] uses a pure ground state, and two CW lasers with frequencies ω_1 and ω_3, where $\omega_3 = 3\omega_1$. The system consists of an initial eigenstate on the ground surface, and continuum eigenstates that correlate asymptotically to certain molecular arrangements (product channels). The isolated molecule is excited to the continuum on the upper surface by both lasers. The basic premise is that the simultaneous excitation with different frequencies provides two routes that can interfere, and thus control the products. Brumer and Shapiro suggest the (ω_1, ω_3) scheme to control the dissociation of IBr, where possible products are

$$\mathrm{IBr} \rightarrow \mathrm{I} + \mathrm{Br}\ (^2\mathrm{P}_{3/2}) \qquad \text{and} \qquad \mathrm{IBr} \rightarrow \mathrm{I} + \mathrm{Br}^*\ (^2\mathrm{P}_{1/2}). \tag{2.5}$$

Controlling the branching ratio of this photodissociation reaction is significant because excitation with wavelengths < 526 nm yields mostly Br^*.[42] Figure 2–5 shows the potential energy curves and a schematic of the procedure. The ground state is exited by both lasers to the $^3\Pi_o^+$ curve (dashed horizontal line). Following photoexcitation, a "diabatic-like" dissociation occurs yielding Br^*, or an "adiabatic-like" dissociation occurs giving Br. The products produced depend on the properties of the excitation source.

Once again, Brumer and Shapiro use a perturbative approach to calculate the probability to produce a particular reaction product. The total probability to exit from a reaction channel resembles the form mentioned previously in Equation (2.3). Specifically,

$$P_{total} = P_1 + P_3 + P_{13}, \tag{2.6}$$

where P_1 is the probability of producing products due to ω_1 (three photons), P_3 is the probability of producing products due to ω_3 (single photon), and P_{13} is the cross term due to interference between the paths. P_3 is proportional to the amplitude of the ω_3 laser multiplied by the dipole matrix element squared. P_1 is proportional to the amplitude of the ω_1 laser multiplied by the matrix element squared containing the three-photon operator. The cross term is proportional to both laser amplitudes modulated by the cosine of the relative phase. An expression for the product ratio contains the probability for exit from Channel 1 divided by the probability of exit from Channel 2. Two parameters are defined, $x \propto (E_1/E_3)$ and $\theta_3 - 3\theta_1$. These parameters refer to the field amplitudes of the ω_1 and ω_3 lasers, and the relative phase difference between the laser fields.

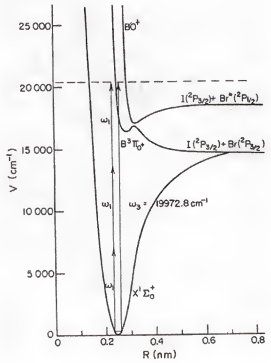

Figure 2–5: IBr potential curves relevant to the (ω_1, ω_3) photodissociation scheme described in the text. The lasers simultaneously excite the initial state to the dashed line, where the population can exit two product channels to form Br* and Br. Reprinted with permission from C. K. CHAN, P. BRUMER, AND M. SHAPIRO, J. CHEM. PHYS. **94**, 2688 (1991). Copyright 1991, American Institute of Physics.

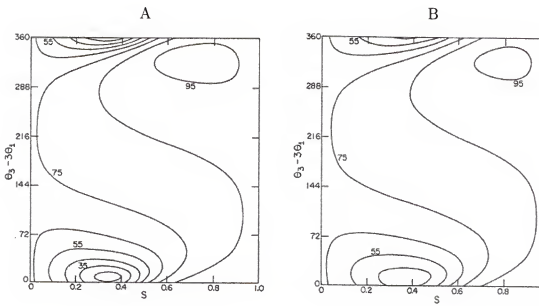

Figure 2–6: Contour plot of the yield of Br*. S is the amplitude parameter, $x^2/(1+x^2)$, and $\theta_3 - 3\theta_1$ is the relative phase. A) Initial state specified as $J = 1$, $M = 0$; B) Initial states are $J = 1$, and all three values of M. Reprinted with permission from C. K. CHAN, P. BRUMER, AND M. SHAPIRO, J. CHEM. PHYS. **94**, 2688 (1991). Copyright 1991, American Institute of Physics.

This work by Brumer and Shapiro shows that by altering variables accessible to experimentalists, x and $\theta_3 - 3\theta_1$, significant control of product formation is possible. They assume the initial vibrational state is $\nu = 0$ on the ground surface, and investigate the effects of angular momentum on the control procedure. The results are displayed in Figure 2–6. The figure shows a contour plot of the percentage of Br* produced from the photodissociation process described previously. The ordinate is labeled by an amplitude parameter, $S = x^2/(1+x^2)$, and the abscissa is the relative phase. Panel A specifies $J = 1, M = 0$, and $\omega_1 = 6657.5$ cm^{-1}, where these are the total angular momentum, z projection of the total angular momentum, and excitation frequency respectively. The Br* yield can be varied significantly from less than 25% with $S = 0.35$ and the relative phase of 15°, to greater than 95% with $S = 0.8$ and a relative phase of 325°. A second calculation gives the product ratio accounting

for the different values of M. This is accomplished by calculating the exit probability independently for each of the possible $2J + 1$ values of M, and then taking the average. The yield in this case can be seen in Panel B. The overall features of this plot are the same as that for the single projection value, with slight differences in the location of the contours.

In another example, Brumer and Shapiro designate the initial state as $J = 42$, and average the yield over all possible values of M. This rotational level is chosen because at room temperature, it is the most highly populated angular momentum state. The results are displayed in Figure 2–7 with $\omega_1 = 6635$ cm^{-1}. Again, the control of product formation is quite significant. The photodissociation reaction can be forced to yield either product almost exclusively. The results are not spoiled when using higher energy initial states. The theoretical success of the Brumer-Shapiro method to control product formation has spurred several experimental groups to formulate control problems in the (ω_1, ω_3) framework.

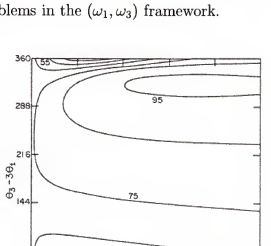

Figure 2–7: Contour plot of the yield of Br*. S is the amplitude parameter, $x^2/(1+x^2)$, and $\theta_3 - 3\theta_1$ is the relative phase. The initial states are $J = 42$, and all eighty-five values of M. Reprinted with permission from C. K. CHAN, P. BRUMER, AND M. SHAPIRO, J. CHEM. PHYS. **94**, 2688 (1991). Copyright 1991, American Institute of Physics.

Experimental verification of the interference created by one-photon and three-photon pathways has been demonstrated. Chen and Elliot[43,44] have observed signal interference while conducting ionization experiments in atomic Mercury. An intermediate step in their experiment involves a bound transition using the (ω_1, ω_3) procedure. A modulation of the ion signal following the intermediate step is observed as the pressure of gas in the chamber is increased. The phases of the laser fields are shifted in magnitude as they pass through the gas. The relative phase between the fields is varied when the gas contains a strong dispersion near one of the laser frequencies. The interference is a result of coherent excitation of the two competing pathways, and is modulated by varying the relative phase. The relative phase is modulated by 2π as the gas pressure increases by about 6 Torr.

In similar experiments, Gordon and co-workers[45,46] observe signal modulation in diatomics such as HCl and CO. The goal of reaction control is more evident in their studies as the products are chemically distinct. The technique is applied to transitions involving different electronic states, different rotational lines of the same electronic state, and competing chemical processes. A key point is that in all cases the transitions induced are bound to bound, and hence not a true implementation of the Brumer-Shapiro method which involves continuum states, and eventually product formation.

Kleiman, Gordon, and co-workers[47] have performed experiments demonstrating phase control using the Brumer-Shapiro method of bound to continuum transitions. They control the direct ionization of the polyatomic molecule H_2S. The molecule is excited above the ionization threshold creating the ions S^+ and HS^+. Both ion signals show a characteristic modulation in phase with each other, as the relative phase between excitation fields is altered. The modulation depths of the individual ion signals are slightly different, producing a product ratio (S^+/HS^+) of 4–4.75 depending on the gas pressure. The group also finds similar results for the photodissociation

of CH_3I,[48] where the ratio of (I^+/CH_3^+) is 2−2.5. The most impressive results are obtained when Gordon et al.[49] excite HI. They are able to control the product ratio of HI^+ to I^+ following laser excitation of HI. Again the two pathways display the modulation of ion signal as a function of gas pressure. However, in this system the signals are conveniently out of phase with each other. The signals show a notable difference in ion concentration as a function of relative phase. The product ratio of (HI^+/I^+) is 2−4 depending on the gas pressure. The product channels can be populated over a significant range, as the Brumer-Shapiro scheme suggests. The exact reasons for the phase lag in HI are the subject of subsequent studies.[50,51]

2.3 Optimal Control Theory

Another means of control employs pulse shaping to manipulate system dynamics. A variety of experimental techniques available currently can produce short, intense wave forms. It is also now possible to generate modulated frequencies, complex envelopes, or trains of pulses. While the technology is readily accessible, experimentalists need a procedure to deduce which pulse traits will yield the desired outcome. It is often the case that intuitive guesses of pulse shapes or sequences are inadequate, and cannot be used to attain target objectives. The subtle intricacies of a quantum mechanical system coupled to an electric field are not trivial. One way to combat this quandary is to use the machinery of Optimal Control Theory (OCT). A desired target outcome is defined, and then one determines the conditions necessary to achieve it. Several groups have used OCT to predict the optimal laser pulse for a desired task. The general procedure is a constrained optimization with Lagrange multipliers. A functional is assembled containing the function to be interrogated, and the constraints placed on the system. The variation of the functional leads to set of coupled differential equations with specified boundary conditions. An iterative procedure yields the solution. Upon convergence, the optimal laser field that induces an extremum of the functional and abides by all of the imposed constraints is obtained.

Numerous groups have analyzed the OCT procedure for chemical purposes. Specifically, they have investigated the feasibility of the process for discovering shaped laser pulses that drive a wave function governed by the Schrödinger equation to specified final state.[52–56] Rabitz and co-workers[52] have proven the existence of an optimal laser field for the above task, and have shown that under general conditions there are an infinite number of reasonable solutions. These may not correspond to the true (global) extremum of the functional, yet are satisfactory to achieve reasonable results.[54] Rice and Zhao[53] have extended the existence analysis to include unbound, continuum states. Some exceptions have been noted. For example, an optimal pulse is not discovered when the initial state consists of numerous states with uncertain phases. Under these conditions, the OCT procedure cannot drive an initially random state to a pure final state.[55]

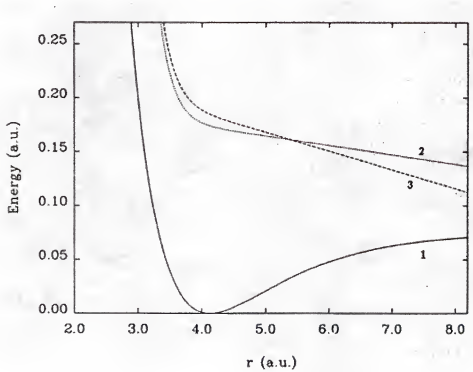

Figure 2–8: Potential energy curves of a model diatomic system. Reprinted with permission from P. GROSS, D. NEUHAUSER, AND H. RABITZ, J. CHEM. PHYS. **96**, 2834 (1992). Copyright 1992, American Institute of Physics.

Rabitz and co-workers[52] have investigated numerous control objectives using the OCT methodology including final state control and dissociation. One study similar in spirit to previous examples examines curve crossing dynamics between two dissociative electronic surfaces.[57] OCT produces optimized laser pulses that can enhance or eliminate certain product channels. The system consists of three surfaces. The ground state is a Morse potential, while the excited potentials are repulsive (Figure 2–8). The excited states cross at $r_x = 5.25$ au, and are coupled by an interaction term $\propto A\exp(r - r_x)^2$. The value of A is varied to simulate strong, medium, and weak coupling. In the case of strong coupling ($A = 0.0075$) most of the wave packet crosses over to the V_2 potential, and then exits. A narrow wave packet is placed on the V_3 potential centered at $r = 4.25$ au, initially at rest. It is then propagated using the Split Operator Method (Appendix C). In the absence of an electric field, 87% of the population exits from Channel 2. The goal is to design a laser pulse using OCT that eliminates product Channel 2 and enhances the products exiting from Channel 3. The optimized wave form found is displayed in Figure 2–9. A low frequency filtering technique is applied to limit the pulse intensity and the frequency components to an experimentally accessible range. The wave packet is excited with the optimal field from V_1 to V_3, and begins to evolve towards the crossing region. Between $t = 200$ and 500 au most of the population is dumped back to the ground surface conserving momentum, and oscillating back and forth in a bound region. When the wave packet reaches the inner turning point on the ground surface, significant amounts of population are excited (mostly to V_3) at $t \approx 800$ au and again at $t \approx 2000$ au. The density on V_3 then passes the crossing region without losing a significant amount of population (Figure 2–10). The authors attribute their success of the method to the added momentum generated from excitation high on the potential curve at the inner turning point, as well as the delicate interferences that alter the curve-crossing dynamics. After application of the laser field, the yield in

Channel 3 increases to over 63% from the initial value of 12%. Similarly impressive results are obtained using other values of the coupling, and different target objectives. Ironically, the mechanism here is reminiscent of the Tannor-Rice pump-dump process in the reverse order. Indeed, Tannor and Rice[58] have utilized OCT to design pulses to optimize performance in their pump-dump procedure.

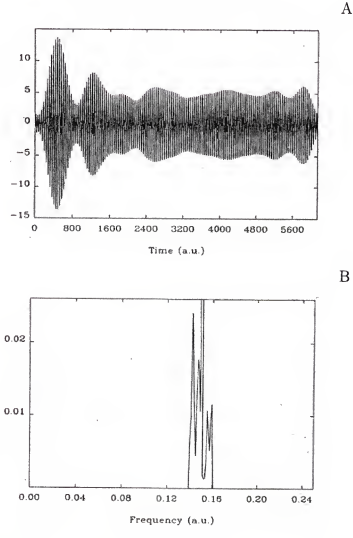

Figure 2–9: Optimal field calculated to steer population out of exit Channel 3. A) Electric field $\times 10^{-2}$ au; B) Power spectrum. The height of the ω_0 peak in the power spectrum is 0.99. This frequency corresponds to the resonant transition between V_3 and V_1 at $r = 4.9$. Reprinted with permission from P. GROSS, D. NEUHAUSER, AND H. RABITZ, J. CHEM. PHYS. **96**, 2834 (1992). Copyright 1992, American Institute of Physics.

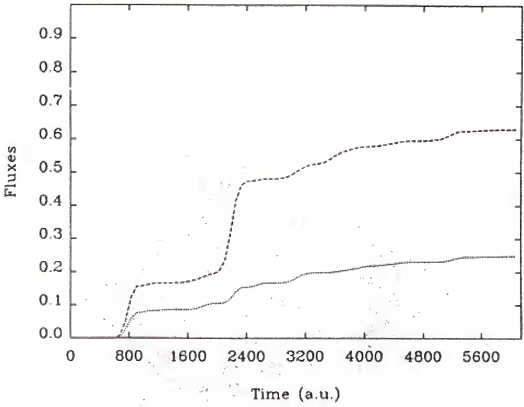

Figure 2–10: Time integrated fluxes of transmitted probabilities in Channel 2 (dotted line) and Channel 3 (dashed line). Reprinted with permission from P. GROSS, D. NEUHAUSER, AND H. RABITZ, J. CHEM. PHYS. **96**, 2834 (1992). Copyright 1992, American Institute of Physics.

The iterative process necessary for calculating excitation fields using OCT works well, and frequently produces pulses that contain complex, non-intuitive structure. However, there are some disadvantages. The iteration procedure is computationally expensive, and quite often generates fields which are not experimentally feasible. Commonly, for example, very intense fields are predicted with rapid turn ons (and offs). Several groups have addressed these problems. Tannor and co-workers[59,60] have used Krotov's optimization theory to control dissociation and multiphoton excitation. This method reduces the computer time by a factor of four. Rabitz and co-workers[61,62] have developed a family of rapidly convergent iteration methods. They include a multiplicative factor to terms in the functional that uncouples the boundaries. Also,

one can obtain mechanistic information, and achieve robust solutions by adding terms to the fitness function.[63] Sundermann and Vivie-Riedle[64] have altered the functional to induce a smooth turn on and off of the pulse. They show that the adjusted pulses affect the performance only slightly.

Wilson et al.[65] have formulated formulated a version of OCT that is specific to the weak response regime. This method alleviates the need for an iterative solution The excited state population scales linearly with laser intensity in the weak response regime, and system dynamics are accurately described by perturbation theory. The globally optimal field that produces the best overlap with a target state at a specific time is calculated directly. As with strong-response OCT, a variation of a functional produces an equation for the field. Approximations valid in the weak response regime allow the formulation of the equation as an eigenequation. Diagonalization gives numerous locally optimal fields, and one globally optimal field, which is the eigenvector of the largest eigenvalue. A density matrix formalism allows studies of numerous scenarios such as distributions of initial states, high temperatures, or dynamics in solutions.

Krause et al.[66] have used this formulation to demonstrate significant control of the molecular dynamics of I_2 by focusing wave packets on the excited B state potential surface. The momentum and position of the evolving state are specified at a predetermined target time. They title creatively two such scenarios the "cannon" and the "reflectron." These colorful names describe a dissociating target state with positive momentum, and a bound target with negative momentum. The characteristics of the optimal pulses are unique to the chosen target state, and quite different from each other. The pulse optimized for the cannon has a significant positive linear chirp and a slight quadratic chirp. It also contains a large bandwidth, with frequencies above the B state dissociation energy of I_2 (20,000 cm^{-1}). This is consistent with the dissociating target state. The excited wave packet is initially very wide, but begins to focus

as it approaches the target time. The justification for the positive chirp is that the low energy components of the wave packet will take longer to reach the target (less momentum from the inner potential wall), and hence need to be excited first. The pulse optimized for the reflectron has a negative chirp and frequencies ~ 2000 cm^{-1} below that of the cannon, corresponding to a bound energy region of the potential. This is again consistent with the chosen target state. In this case, the higher energy components will take longer to reach the outer potential wall, and experience flatter regions of the potential. Therefore, these components need to be excited first. In both cases the overlap with the target state is close to unity, indicating nearly perfect control.

Numerical fits of the optimized pulses, whose form is readily accessible to experimentalists, yield good control of the system dynamics as well. In fact, the negative chirp designated in the reflectron scenario has been verified experimentally proving the predictive value of the work.[67] In addition, the solutions are extremely robust. Later work has extended the results to the strong response regime, and finds that the perturbative results can include situations in which significant population transfer occurs (well beyond the linear regime).[68] The laser fields calculated in the weak regime provide excellent first guesses of pulse shapes for the iterative process necessary in the strong response regime, and converge in less than ten iterations.[68]

2.4 Local Control

Rabitz and co-workers[69] have developed a method known as tracking, in which the need for an iterative procedure to find the solution is not necessary. The idea is specify the path that a chosen observable follows, and calculate the field corresponding to the predetermined path. The time variation of an observable specified by operator, O, is

$$\frac{d\langle O\rangle}{dt} = \frac{i}{\hbar}\langle\psi\,|\,[H,O]\,|\psi\,\rangle + \langle\psi\,|\dot{O}\,|\psi\,\rangle. \tag{2.7}$$

The Hamiltonian, H, is of the form $T + V - \mu\varepsilon$, where T and V are the kinetic and potential energy operators, and the remaining terms represent the laser interaction. Equations for the field are derived, which produce the predetermined path of the observable. For example, if one wants to control position the expression is

$$\frac{d\langle x\rangle}{dt} = \frac{1}{m}\langle\psi\,|\,p_x|\psi\rangle. \tag{2.8}$$

The above equation contains no contribution from the field. Differentiating again gives

$$\frac{d^2\langle x\rangle}{dt^2} = \frac{1}{m}\langle\psi\,|\frac{\partial\mu}{\partial x}|\psi\rangle\,\varepsilon - \frac{1}{m}\langle\psi\,|\frac{\partial V}{\partial x}|\psi\rangle, \tag{2.9}$$

where the electric field is present explicitly, and can be found by providing a reasonable path, and its second derivative. An initial state is selected with characteristics matching the specified path (i.e., the same average values of x and p_x at $t = 0$). The electric field is then calculated with Equation (2.9). Using the calculated field, the initial state is propagated one step, and the process is repeated with the new wave function. The process relies on choosing a physically reasonable path. Spectacular intuition, or reasonable knowledge of the ensuing events are imperative to yield experimentally feasible laser fields. Although the Schrödinger equation is linear, the proposed scheme is highly nonlinear, and sometimes becomes unstable. Rabitz and co-workers[70,71] have expanded the general tracking process outlined here to give useful information such as potential surfaces and dipole moments. Other methods of calculating the field locally (on the fly) have been developed. Tannor and co-workers[72–74] have shown that energy and state population can be controlled with local optimization schemes.

2.5 Closed Loop Procedures

Rabitz and Judson[75] have contributed to the realization of using laser pulses to control molecular dynamics with the suggestion of a closed loop procedure. They propose a cyclic process, where a learning algorithm finds the optimal laser pulse.

The procedure is as follows. An initially chosen field excites the system, and produces an experimental observable, which compares directly to a fitness function. An algorithm then searches for characteristics of a new laser field that increase performance, and the cycle is repeated. The procedure continues until the optimal laser field is discovered. In a sense, the closed loop process solves the Schrödinger equation exactly, without any knowledge of the system. It also provides solutions that can be robust against laboratory uncertainties and equipment drifts because the algorithm is constantly accounting for them.[76] This form of feedback control eliminates the need to have prior knowledge of the system Hamiltonian. For very large, complex systems, the Hamiltonian is often unknown, and contains complicated molecular couplings and numerous degrees of freedom. A numerical solution in these conditions is often impossible. Moreover, methods such as OCT rely on a good Hamiltonian to generate reasonable results. In many cases the fields calculated contain considerable structure, and are difficult to reproduce experimentally.

Many types of searching algorithms have been employed to optimize laser fields for a particular task. Rabitz and Phan[77,78] have investigated an algorithm based on linear input-output mapping. Two well-tested methods are simulated annealing and genetic algorithms (GA) (Appendix D). Both have been shown to converge in this type of application.[79] Simulated annealing is usually faster, however a GA tolerates more noise without loss of performance.[76] For this reason, GAs have dominated most closed loop experiments.

Rabitz's closed loop feedback proposal has spawned several successful experimental implementations. Wilson and co-workers[80] have used feedback control to alter emission from large molecules. A GA is used to optimize wave forms that maximize population transfer from the ground surface to an excited surface of the laser dye molecule IR125 in methanol. The laser pulses are adjusted by the algorithm to increase fluorescence of the molecule in solution. Two different criteria are used to

rank performance, efficiency and effectiveness. In the former case the goal is to maximize the yield with respect to laser power, while in the latter case no restrictions are placed on laser intensity. The optimal form of the laser pulses are wildly different. The field optimized to be most efficient has low power, a narrow band width, and a slight negative linear chirp. The GA finds that the maximum fluorescence yield is generated by exciting only a narrow spectral region close to the absorption peak of the molecule at 13,000 cm^{-1}, and does not waste laser intensity in other spectral regions. The pulse optimized to be most effective is intense, with a large band width, and a significant positive chirp. The authors attribute the positive chirp to a dynamic Stokes shift from the intense pulse. The levels shift to lower frequencies as the pulse sweeps through the resonance, and thus population transfer is maximized. These results indicate that the optimization process can be tuned to match experimental requirements, such as pulse intensity. Most impressively, the closed loop procedure succeeds even while investigating complex molecules in solution.

Gerber and co-workers[81] have used a feedback loop to optimize branching ratios of organometallic photodissociation reactions. They find that the relative populations of ions can be maximized or minimized without any prior knowledge of the reaction mechanism. The optimized wave forms induce different multiphoton effects and fragmentation processes. An evolutionary algorithm adjusts the laser fields, while product ions are detected by a time of flight spectrometer. In one example, the goal is to control the relative yield of Fe^+ and $Fe(CO)_5^+$ produced from the photoexcitation of $Fe(CO)_5$. Several other ions are produced in the dissociation, but are not included in the optimization. The ratio of $Fe(CO)_5^+/Fe^+$ can be maximized or minimized by the feedback optimization. This allows significant control of the ions produced in the dissociation channels. Similar results are found in more complex organometallics such as $CpFe(CO)_2Cl$ where $Cp = \eta^5\ C_5H_5$ (a five membered carbon ring coordinated to the metal).[81]

Other groups have also produced promising results using feedback loops to optimize laser pulses for different tasks. Daniel et al.[82] have used a pump-probe interrogation defined by a feedback loop to optimize ion ratios in the photodissociation of $CpMn(CO)_3$. Feurer and co-workers[79] have implemented a modified Tannor-Rice control scheme to maximize Cs^+ ions from the photodissociation of CsCl. Bucksbaum and Weinacht[83,84] have used feedback to control the radial wavefunction in Cesium, dissociation of Na_2, and molecular vibrations in methanol.[84] Particular modes can be excited, or suppressed with properly sculpted laser fields. Levis and Rabitz[85] have used intense laser pulses to control ion yields produced from photodissociating a series of organic molecules. All of these studies are all impressive examples of feedback control realized in experiments.

2.6 Stimulated Raman Adiabatic Passage

As the field of molecular dynamics grows, it is evident that there is a need for techniques that can prepare atoms or molecules in a specific quantum state. Ideally, these techniques transfer population in an efficient and robust manner, offsetting some experimental uncertainties. One scheme developed for this task is STIRAP (Stimulated Raman Adiabatic Passage).[86–88] Essentially, STIRAP is the multi-level analogue of the widely studied topic of adiabatic passage in a two-level system.[31,89,90] It has proven to be an ideal scheme for selective population of high-lying vibrational states. STIRAP is fairly insensitive to experimental uncertainties, which makes the procedure robust. Also, it can be used to populate states that are inaccessible by single photon excitation according to selection rules.

The basic implementation of STIRAP involves three states, and two laser fields. A pump laser couples States $|1\rangle$ and $|2\rangle$, while a Stokes laser couples States $|2\rangle$ and $|3\rangle$. The initial state, $|1\rangle$, might be the ground vibrational state. State $|2\rangle$ could be a state on an excited potential surface, while $|3\rangle$ may be an excited vibrational state on the lower energy surface. The model designates States $|1\rangle$ and $|3\rangle$ as long lived, while

State $|2\rangle$ can, in principle, undergo spontaneous emission to other levels. The goal is to transfer all of the population from the initial state, $|1\rangle$, to the final state, $|3\rangle$, without any loss through decay processes. Population loss corresponds essentially to populating the intermediate state, $|2\rangle$. The model assumes that the initial state and final state are not dipole coupled, therefore a direct transition is impossible, and the two-step excitation procedure must be used.

Incoherent processes typically transfer at most 50% of the population to the target state for each transition.[88] For example, using incoherent radiation to excite the intermediate state, and then the target state will yield at most 25% of the population in the final state.[88] Using a coherent process has potential advantages. However, if intense lasers are tuned to resonance, Rabi cycling will decrease the efficiency and robustness. An alternate approach is to sweep through the resonance slowly with a coherent laser pulse inducing adiabatic passage. This process can populate the target state completely and efficiently, as long as certain criteria are satisfied. A well-designed STIRAP experiment shows these predictions are true. The most robust and successful implementation uses a partially overlapping, counterintuitive pulse sequence, in which the Stokes pulse precedes the pump pulse. The Stokes pulse first couples the two empty states, creating a coherent superposition. This state is then coupled to the initial state by the pump pulse. A trapped state is formed that cannot transfer population to the leaky intermediate, and therefore all of the population is driven to the desired final state.

A convenient way of interpreting the STIRAP procedure is to examine the time-dependent eigenvalues and eigenvectors while the laser excitation is occurring. The Hamiltonian matrix for three nondegenerate states coupled by two laser fields, within

the rotating wave approximation can be written as

$$H(t) = \frac{\hbar}{2} \begin{bmatrix} 0 & \Omega_P(t) & 0 \\ \Omega_P(t) & 2\,\Delta_P & \Omega_S(t) \\ 0 & \Omega_S(t) & 2\,(\Delta_P - \Delta_S) \end{bmatrix}. \tag{2.10}$$

In the preceding matrix, the Rabi frequencies are

$$\Omega_P(t) = \mu_{12} E_P/\hbar \qquad \text{and} \qquad \Omega_S(t) = \mu_{23} E_S/\hbar, \tag{2.11}$$

where μ_{ij} are the dipole matrix elements, and $E_{P,S}$ are the laser pulse envelopes (P for pump, S for Stokes). The detunings converted to energies are

$$\hbar\Delta_P = (E_2 - E_1) - \hbar\omega_P \qquad \text{and} \qquad \hbar\Delta_S = (E_2 - E_3) - \hbar\omega_S, \tag{2.12}$$

where $\omega_{P,S}$ are the center frequencies of the laser fields. The time-dependent states excited by the laser fields are known as dressed states, and are the following linear combinations

$$|\,a^+\rangle = \sin\Theta \sin\Phi\,|1\rangle + \cos\Phi\,|2\rangle + \cos\Theta \sin\Phi\,|3\rangle \tag{2.13}$$

$$|\,a^0\rangle = \cos\Theta\,|1\rangle - \sin\Theta\,|3\rangle \tag{2.14}$$

$$|\,a^-\rangle = \sin\Theta \cos\Phi\,|1\rangle - \sin\Phi\,|2\rangle + \cos\Theta \cos\Phi\,|3\rangle, \tag{2.15}$$

where the mixing angle is defined by

$$\tan\Theta = \frac{\Omega_P(t)}{\Omega_S(t)}. \tag{2.16}$$

The expression for the angle Φ is of minimal importance for the following discussion. Note though, $\tan\Phi = 1$ when the fields are in resonance. The time-dependent eigenvalues are

$$\omega^{\pm} = \Delta_P \pm \sqrt{\Delta_P^2 + \Omega_P^2 + \Omega_S^2} \qquad \text{and} \qquad \omega^0 = 0. \tag{2.17}$$

The form of the dressed states provide a prescription for achieving the goal of complete population transfer from bare state $|1\rangle$ to $|3\rangle$. The obvious route is to use Equation (2.14), which does not populate State $|2\rangle$ at any time. This can be accomplished by adjusting the ratio of (Ω_P/Ω_S), and in turn manipulating the mixing angle Θ. In this situation, the counterintuitive pulse sequence is derived naturally from the the dressed state picture. A careful adjustment of pulse intensities allows the population to occupy $|a^0\rangle$ exclusively. In particular, decreasing the amplitude of the Stokes pulse while increasing the amplitude of the pump pulse produces a smooth transfer from bare state $|1\rangle$ to $|3\rangle$ as Θ goes from zero to $(\pi/2)$. Care must be taken to adjust the intensities and pulse overlap such that $|a^0\rangle$ is followed adiabatically, and no coupling to the other dressed states occurs. Specifically, the coefficients multiplying $|1\rangle$ in the other dressed states, $\sin\Theta\sin\Phi$ and $\sin\Theta\cos\Phi$, must be neglibly small while the amplitude of $|1\rangle$ is significant. A criterion for adiabaticity can be derived which shows that the procedure will be successful when $\dot{\Theta} \ll |\omega^{\pm} - \omega^0|$. Bergmann and co-workers[88] have developed another criterion for successful transfer from experimental experience stating $\Delta\tau\sqrt{\Omega_P^2 + \Omega_S^2} > 10$, where $\Delta\tau$ is the laser interaction time.

Halfmann and Bergmann[91] have demonstrated STIRAP experimentally in SO_2. They find that using the method outlined above, approximately 100% of the population is transferred between vibrational states efficiently and robustly. A pump laser couples the ground vibrational state to the (1,1,0) state on an excited surface, while the Stokes pulse couples the (1,1,0) state to the (9,1,0) state on the ground surface. Figure 2–11A displays a schematic of this scenario. The population in the target state is probed by excitation to a higher energy level, and then observed by fluorescence. The intensity of emission is directly proportional to the population of the (9,1,0) state. As can be seen in Figure 2–11B, the intensity is diminished greatly when the Stokes pulse is not applied. The authors define a transfer efficiency proportional to a normalized fluorescence signal. Figure 2–12 shows a plot of the transfer efficiency

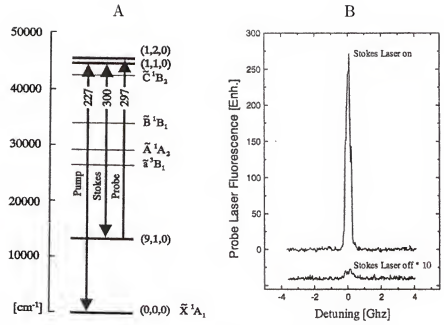

Figure 2–11: STIRAP in SO_2. A) Schematic with wavelengths given in nm; B) Fluorescence signal (proportional to the target state population) with and without the Stokes pulse. The lower trace has been shifted down and multiplied by ten for clarity. Reprinted with permission from T. HALFMANN AND K. BERGMANN, J. CHEM. PHYS. **104**, 7068 (1996). Copyright 1996, American Institute of Physics.

as a function of delay between the pump and Stokes pulses. The STIRAP signature is evident. Nearly complete population transfer is achieved when the Stokes pulse precedes the pump pulse. The flat plateau around -4 ns is a signal of robustness. Small variations in pulse timing do not greatly affect the transfer efficiency. The experiment is in complete agreement with theory predicting the optimal conditions for complete population transfer.

The basic version of STIRAP mentioned above can be extended to more accurately represent typical experimental conditions. Concerns such as molecules with weak oscillator strengths, or unstable intermediates have both been addressed. In addition, systems with a high density of levels surrounding the three states, as well as STIRAP with many level systems have been investigated. In many instances, these

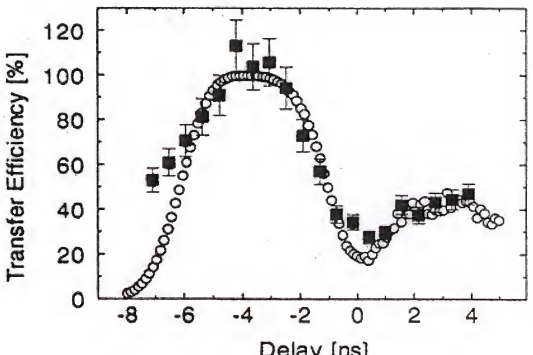

Figure 2–12: Variation in transfer efficiency versus delay time between the pump and Stokes pulses. The filled squares are experimental data, while the open circles are a simulation. Both show the most efficient population transfer when the Stokes pulse precedes the pump by 4 ns. Reprinted with permission from T. HALFMANN AND K. BERGMANN, J. CHEM. PHYS. **104**, 7068 (1996). Copyright 1996, American Institute of Physics.

situations are not problematic, and can be overcome with small variations of the original STIRAP procedure. The slight adjustments yield results that are surprisingly stable, and are therefore applicable to a wide array of problems.[92–95]

Several other methods designed to control population using adiabatic passage have now been demonstrated. Techniques such as exciting a high-energy region with a laser field, and then using a dc field to Stark shift the level into resonance have been used to control population in two and three-level systems.[96,97] Another concept employs frequency modulation (pulse chirping) to fulfill the adiabaticity requirements. The laser pulses are designed with frequencies that vary in time, and sweep through the resonance in the appropriate manner. Chirped pulses have been shown to produce

robust, state-selective excitation. High-lying vibrational states can be populated, or the molecule can be dissociated by an appropriately chirped laser pulse.[98,99] In this case, the probabilities are enhanced greatly compared to the corresponding transform-limited pulses.[100,101] Indeed, chirped laser pulses can be used in the STIRAP procedure without detrimental effects, while allowing beneficial improvements such as less intense pulses and increased robustness.[102–104] A related method known as adiabatic passage by light induced potentials (APLIP) uses very intense fields that deform potential surfaces.[105–107] This allows a wave packet to travel a continuous path to the desired final state. Chirped pulses can also be used in the APLIP method to allow more flexibility in the path of the evolving state.[108]

2.7 Other Molecular Control Objectives

The quantum control literature is increasing rapidly. It is impossible to categorize every study in the preceding sections. An exhaustive review of all areas and interests is not feasible. The purpose of this abbreviated section is to note briefly some novel techniques, which do not lend themselves to the classifications in the preceding sections. A thorough explanation and synopsis of these methods is not attempted. Rather, a short account of the research goals and results is provided, as well as citations to the original work.

Several studies have investigated methods to produce a single enantiomer from an initial configuration not predisposed to yield one or the other of the racemates. Schemes in organic synthesis typically use a chiral reactant that is subjected to certain conditions that generate only a single product enantiomer. Some members of the control community have deduced alternative methods. Brumer and Shapiro[109] have shown that the ratio of left- and right-handed products can be altered by using plane polarized laser light to photodissociate the molecule. Adjusting the delay time between pulses allows control over the product channels in a pump-dump scenario. Fujimura et al.[110] have used an elliptically polarized laser pulse optimized using

Optimal Control Theory (OCT) to drive an initially racemic mixture to 100% of a single enantiomer.

In a similar spirit, tailored laser fields have been used to separate isotopes in a mixture. Charron and co-workers[111] have shown that linearly polarized light containing the fundamental frequency and its second harmonic photodissociates diatomic molecules in a manner allowing separation of product distributions. Leibscher and Averbukh[112] have used tailored laser fields optimized with OCT to separate $^{79}Br_2$ and $^{81}Br_2$. They have devised a scheme based on the different masses, and hence slightly different periods, that allows spatial separation of wave packets evolving on an excited surface. Another control scheme uses a pump-dump procedure and interference effects to separate the product isotopes.[112]

A number of researchers have shown that polar molecules can be oriented in a specific manner with customized laser pulses. Dion and co-workers[113] have used intense, linearly polarized laser fields containing the fundamental frequency and the second harmonic to orient HCN. They find that orientation is possible due to the simultaneous action of the fields on the permanent dipole, as well as the polarizability. Hoki and Fujimura[114] have used OCT to optimize laser fields that control the alignment of CO. The fully optimized pulses are compared to the fields calculated by Dion, and show similar mechanisms characteristics.

Paramonov and co-workers[115,116] have demonstrated that tailored pulse sequences can control population transfer to high-lying vibrational states. This is essentially the same goal as STIRAP, however the mechanism is quite different. Numerous subpulses and multiphoton effects are used to populate desired vibrational states, or induce photodissociation. These calculations include environmental effects via coupling the molecular system to a bath of harmonic oscillators. As much as 80% of the

population can be coerced into a desired target state, or 75% driven beyond the dissociation limit.[117] Later studies have shown that by linearly polarizing the excitation light fields, the dissociation can be increased to nearly 100%.[115,116]

Hiller and Cina[118] have shown that the amplitude of vibrational motion in I_2 can be increased using optimized pulses, while minimizing electronic absorption. A series of pulses with an appropriate center frequency and linear chirp can significantly increase the I_2 bond length when compared to non-optimized pulse sequences. The authors state that linear chirp can enhance impulsive stimulated Raman scattering, which is encouraging with regard to controlling ground state vibrational distributions.

2.8 Control in Semiconductors

Controlling dynamic properties in the solid state has not been investigated as widely as in gas phase atoms and molecules. Schemes have been reported to control the dynamics of molecules encased in solid matrices such as Argon or Krypton.[119,120] From a technological point of view, controlling "caged" molecules has less impact than controlling optoelectronic properties and charge carrier dynamics in semiconductors. The computer boom has fueled massive research efforts in these systems, some of which are concerned with controlling transport properties. Despite the obvious differences between molecular and solid state systems, many successful implementations of variations of the control schemes outlined above have been applied to semiconductors. Some examples are described below.

In the spirit of the Tannor-Rice method, some early examples of control in semiconductors rely on multiple pulses and delay times for control. Pairs of phase-locked pulses are used to alter system dynamics. The delay time between the pulses can be varied to adjust the relative phase of the coherent events, and induce interference. Heberle and co-workers[121] have shown that a series of pulses with well-defined phase relationships can create excitons in a quantum well, and then either enhance or

suppress them over very short time periods. Also, they have shown that more complicated pulse shapes can further enhance this effect.[122] In a similar study, Cundiff and co-workers[15] have observed density flops in quantum wells. They attribute these observations to phenomena similar to Rabi oscillations in two-level atomic systems.

Laser excitation of semiconductors can excite the atoms, and induce vibrational motion. Several groups have demonstrated the ability to produce coherent interference of phonons generated from excitation with two laser pulses. Dekorsy et al.[123] have developed a method to measure both the phase and amplitude of the vibrational motion. This allows them to apply a second pulse with the correct delay time to generate another wave of coherent phonons, which can interfere constructively or destructively. Other groups have found similar results both experimentally and theoretically in bulk samples and superlattices.[124–126] These examples demonstrate convincingly that ultrashort laser pulses can control the collective motion of atoms in a lattice.

Another application of quantum control via pulse timing has been demonstrated in the emission of electromagnetic radiation from quantum well systems. It is well documented in the solid state literature that photoexcitation of charge carriers across the band gap can create an oscillating charge density in the conduction band of a semiconductor superlattice that emits radiation, typically in the Terahertz (THz) regime. The frequency of the emission is governed by the energy splittings of the states in the superposition state. For example, when a two-state wave packet is created, the frequency is $(\Delta E/\hbar)$ and the period of oscillation is proportional to $(\Delta E)^{-1}$. When the frequency is known, the delay time between laser pulses can be adjusted to enhance or suppress the THz emission. Planken and co-workers[127] have demonstrated this idea in an asymmetric double quantum well. The scenario is as follows. A laser pulse creates a coherent superposition of the two lowest electronic states in the narrow well. The wave packet oscillates back and forth through the barrier with a

known frequency. After an appropriate delay time, another identical pulse excites the system. Both constructive and destructive interference can be observed, depending on the delay time between pulses. When the relative phase is not an integer multiple of π, more complex dynamics are observed including phase shifts. Several subsequent experimental studies, as well as theoretical investigations, have reproduced these results.[128–130] In the spirit of the Brumer-Shapiro method, Pötz[131] has used one-photon and two-photon transitions to control the quantum well emission.

A method similar to the Brumer-Shapiro scheme has been used to control photocurrent direction and magnitude in a semiconductor quantum well. Dupont and co-workers[132] have photoexcited electrons from a bound state to a continuum state with lasers tuned to the one-photon and two-photon resonances. The relative phase between the laser pulses is adjusted by passing the beams through a rotating crystal. A slight rotation of the crystal leads to a phase shift of π when both lasers are applied. The oscillatory nature of the signal is easily observed as the relative phase is varied. Adjusting the crystal offers a means to control the photocurrent magnitude and polarity. The signal modulation is due to interference between the two quantum pathways, as predicted by Brumer and Shapiro. Experiments and theory have shown that this procedure can also control photocurrents in bulk samples.[133,134]

Designing laser pulses to drive wave packets onto predetermined targets has been explored in semiconductor structures. Dargys[135] has investigated controlling transitions between hole states in a semiconductor. The laser field is cast in a parameterized form dictating amplitude, width, and frequency. Initially, these parameters are chosen intuitively to match the resonance condition, and achieve reasonable results. The projection onto the target state is found to be roughly 0.75. A direct optimization procedure based on nonlinear programming is then used to find the laser field that maximizes overlap with the target state. The optimization changes the frequency and amplitude of the excitation field. The optimized laser drives the wave function

to complete overlap with the target state at the specified time. Other studies have used Genetic Algorithms to find pulses that force an evolving wave packet to a certain quantum well at a specific time with excellent results.[136] In fact, feedback loops have been used to optimize laser pulses that control semiconductor nonlinearities.[137] The evolutionary algorithm increases the differential transmission by approximately a factor of four.

As a precursor to studies involving control of population, Pötz[138–140] has designed a novel scheme to control carrier dynamics in double quantum wells with a combination of laser pulses. The intensity and phase of a microwave field that initially couples two states can control absorption and dynamics. The charge density can be forced to remain localized, or tunnel to a different spatial region. These studies show that despite the time limitations imposed in solid state samples due to phase breaking, coherent manipulation of final state population is possible.

Bonadeo[141] and Pötz[139] suggest that quantum control methods might be realized most easily in quantum dots, due to their sharp atom-like states. Hohenester and co-workers[142] have suggested a solid state implementation of STIRAP in a double dot structure. They propose a three-state system composed of a hole state in the left well, $|L\rangle$, a charged exciton state, $|X^+\rangle$, and a hole state in the right well, $|R\rangle$. The charged exciton state consists of one electronic state, and both hole states. The goal is to induce complete population transfer from $|R\rangle$ to $|L\rangle$ using the two-pulse STIRAP procedure. Using the correct pulse timing and pulse intensities, all of the population is moved from the initial state in the right well, to the final state in the left well. At intermediate times the charged exciton state is populated due to nonadiabatic coupling. However, following the laser pulses nearly all of the population resides in the target state. Others have suggested STIRAP in a double-dot structure. Pazy et al.[25] have proposed this idea to create a solid state implementation

of a quantum computer, in which a measurement process can be achieved through coherent population transfer, specifically STIRAP.

As stated previously, the control literature in the solid state is limited compared to the vast amount of work done in gas phase atoms and molecules. However, it is interesting to note that many examples are direct implementations, or slight variations of methods used in molecules. This shows that some of the difficulties posed by condensed phase systems can be overcome. As laser technology progresses, issues associated with control in the solid state may become less important.

CHAPTER 3
PRELIMINARY STUDIES

In previous investigations, Krause and co-workers[136,143] have demonstrated that relatively simple laser pulses are sufficient to control the dynamics of electronic wave packets in quantum wells. Electronic wave packets in the asymmetric double quantum well (ADQW) can be driven to maximum overlap with a target distribution in a desired well at a specified time. Alternatively, given a fixed laser pulse, the structure of the quantum well system, such as well and barrier dimensions, can be customized to maximize the overlap with the target distribution.

This work examines the robustness of previous results to several possible effects that might be expected to influence carrier dynamics. These effects include fluctuations in the dc bias field, growth imperfections in the layered structure, and environmental effects such as vibrational dissipation. These are possible phase breaking events that could place an upper bound on the time period in which significant control of electronic dynamics is possible. Investigation of these effects is important when considering the feasibility of control in semiconductors. In addition, the treatment is extended to include a multi-well superlattice (SL). In this case, the carrier dynamics are much more complex due to numerous interacting states, and the multiple quantum wells present in the potential profile. Results show that significant control of dynamics can be attained in both the ADQW and the SL.

3.1 Carrier States and Dynamics

The following theoretical methodology, known as the envelope function model, is well established for treating dynamics in semiconductor heterostructures.[144,145] The wave functions for carriers in quantum well systems can be separated as rapidly oscillating band-edge Bloch states, $u^{\alpha}(\mathbf{r})$, a slowly varying envelope function, $\phi_n^{\alpha}(z)$,

and two-dimensional plane waves given as

$$\Phi^{\alpha}_{n,\mathbf{k}}(\mathbf{r}) = \frac{e^{i\mathbf{k}\cdot\mathbf{r}}}{\sqrt{A}}\, u^{\alpha}(\mathbf{r})\, \phi^{\alpha}_{n}(z), \tag{3.1}$$

where $\alpha = e, h, l$ labels the carrier (electrons, heavy holes, and light holes respectively) and n labels the subband. Carrier motion in the confined dimension is described by $\phi^{\alpha}_{n}(z)$, while translational motion in perpendicular dimensions is described by a plane wave with bidimensional wave vector $\mathbf{k} = (k_x, k_y)$ and cross-sectional area A.

When confined in quantum wells, the envelope functions satisfy a one-dimensional, effective-mass Schrödinger equation

$$\left[-\frac{\hbar^2}{2m^*_{\alpha}}\frac{d^2}{dz^2} + V_{\alpha}(z) \pm eFz\right] \phi^{\alpha}_{n}(z) = E^{\alpha}_{n}\, \phi^{\alpha}_{n}(z), \tag{3.2}$$

where m^*_{α} is the effective mass, $V_{\alpha}(z)$ is the confining potential, and F is the static dc field. In the third term, the plus sign is used for the electrons, and the minus sign is used for the holes. Solving the Schrödinger equation yields a set of parabolic subband energies with electronic levels given by

$$E^{e}_{n}(k) = E_g + E^{e}_{n} + \frac{\hbar^2 k^2}{2m^*_e}, \tag{3.3}$$

where E_g is the bandgap and $k^2 = (k_x^2 + k_y^2)$. The energies of the heavy and light holes are

$$E^{h}_{n}(k) = -E^{h}_{n} - \frac{\hbar^2 k^2}{2m^*_h} \qquad \text{and} \qquad E^{l}_{n}(k) = -E^{l}_{n} - \frac{\hbar^2 k^2}{2m^*_l}. \tag{3.4}$$

Equation (3.2) is solved on an evenly spaced, numeric grid. The envelope functions are discretized as $\phi(z_i) = g_i$ and the potential as $V(z_i) = v_i$, where i labels the grid point ranging from 0, ..., N. The wave function is required to vanish at the boundaries of the grid. The second derivative of the envelope functions at interior

grid points is approximated as

$$\frac{d^2 g_i}{dz^2} = \frac{g_{i+1} - 2g_i + g_{i-1}}{\Delta z^2}, \qquad i = 1 \ldots N-1. \tag{3.5}$$

This leads to a tridiagonal matrix for the Hamiltonian as

$$\mathcal{H} = \begin{pmatrix} v_0 + \frac{\hbar^2}{m\Delta z^2} & \frac{-\hbar^2}{2m\Delta z^2} & & & \\ \frac{-\hbar^2}{2m\Delta z^2} & v_1 + \frac{\hbar^2}{m\Delta z^2} & \frac{-\hbar^2}{2m\Delta z^2} & & \\ & \ddots & \ddots & \ddots & \\ & & \frac{-\hbar^2}{2m\Delta z^2} & v_{N-1} + \frac{\hbar^2}{m\Delta z^2} & \frac{-\hbar^2}{2m\Delta z^2} \\ & & & \frac{-\hbar^2}{2m\Delta z^2} & v_N + \frac{\hbar^2}{m\Delta z^2} \end{pmatrix}, \tag{3.6}$$

where the blank areas in the matrix are zero. Diagonalization yields the eigenvalues and the amplitudes of the corresponding envelope functions at each grid point. Previous calculations have used the discrete variable representation (DVR) to solve Equation (3.2).[146] The finite difference scheme is found to be much more efficient, and is in excellent agreement with DVR with the exception of slight discrepancies in highly energetic, unbound regions.

At this point, the theory can be simplified by making some physically reasonable assumptions. First, it is assumed that optical excitation occurs at approximately zone center, where the parabolic bands of the model are an accurate description. When interrogating such interband transitions, all of the relevant dynamical information is contained in the slowly varying envelope functions. Therefore, the z dimension can be treated exclusively (Appendix E). Laser excitation couples the heavy hole state in the valence band to electronic levels in the conduction band. The light hole states are neglected because the corresponding absorption is much less intense.[144] This essentially reduces the problem to an $(N+1)$-level system, where N is the number of wells in the structure, because of the sizeable energy separation between mini-bands. An approximate solution can be obtained using conventional time-dependent perturbation theory. The simplified theory does not describe the dynamics of the holes. This

approach is qualitatively correct for the ADQW, because the holes are essentially trapped by the application of the dc bias field. Experiments have confirmed that the dynamics under these conditions in the ADQW are dominated by the electrons.[6] In addition, the carriers on the ground surface of a coupled-surface calculation do not display notable dynamics until a moderate amount of population is transferred. In most experiments, low intensity lasers are used, which do not produce significant population transfer.

A more advanced theory for this system has been formulated in a density matrix picture that includes the dynamics of the holes explicitly, as well as the perpendicular **k** states. This theory, which does not include Coulomb interactions, reduces to a modified version of the optical Bloch equations.[145] Comparisons between the results obtained with the two theoretical treatments have demonstrated that the simplified version captures the essence of the physics, and is in agreement with the more advanced theory.[136] Due to the extra steps involved in optimizing the excitation pulse, it is beneficial to simplify the problem as much as possible. Therefore, the simplified theory is used in this analysis.

Proceeding from these assumptions, the model Hamiltonian can be written

$$H(t) = H_0 - D\,E\,(t), \tag{3.7}$$

where $E\,(t)$ is the laser field, and H_0 is the time-independent Hamiltonian given by

$$H_0 = H^h|h\rangle\langle h| + H^e\,|e\rangle\langle e|. \tag{3.8}$$

In this equation, H^h and H^e are the Hamiltonians for the heavy holes and electrons from Equation (3.2). The laser field is incident along the growth axis, and assumed to be x-polarized. The symbols in brackets, $|h\rangle$ and $|e\rangle$, designate degrees of freedom accessible to the wave functions. Their properties are represented by the Kronecker delta, δ_{he}. Specifically $\langle e|e\rangle = \langle h|h\rangle = 1$, and $\langle e|h\rangle = \langle h|e\rangle = 0$. The dipole operator,

D, is

$$D = \mu \left\{ |h\rangle\langle e| + |e\rangle\langle h| \right\} \tag{3.9}$$

where μ is the dipole moment connecting the hole states in the valence band with the electronic states in the conduction band. Note that μ is actually μ_x because the field is polarized, as discussed in Appendix E. The total envelope function consists of both hole and electronic components, and is given as

$$|\Psi(t)\rangle = |\Psi^h(t)\rangle\,|h\rangle + |\Psi^e(t)\rangle\,|e\rangle. \tag{3.10}$$

The hole and electron envelope functions can be expanded in eigenstates as

$$|\Psi^h(t)\rangle = \sum_j a_j^h(t)\,|\phi_j^h\rangle e^{-(i/\hbar)E_j^h t}, \tag{3.11}$$

and

$$|\Psi^e(t)\rangle = \sum_n b_n^e(t)\,|\phi_n^e\rangle e^{-(i/\hbar)E_n^e t}. \tag{3.12}$$

The total envelope function satisfies the time-dependent Schrödinger equation,

$$i\hbar\frac{d}{dt}|\Psi(t)\rangle = \{H_0 - D\,E\,(t)\}\;|\Psi(t)\rangle. \tag{3.13}$$

In the ADQW, application of a bias dc field causes the holes states to move out of tunneling resonance. Hence, for the purposes of this work, they are essentially stationary states, and the dynamics are restricted to a wave packet composed of electronic states in the conduction band labeled by $|e\rangle$. Hole dynamics are not treated explicitly in this work, therefore the equation of motion for the holes is not stated, allowing the $|e\rangle$ label on the electronic equation to be dropped for clarity. Inserting the electronic envelope function into the time-dependent Schrödinger equation leads to the following expression for the electronic expansion coefficients,

$$\frac{db_n^e}{dt} = \frac{iE(t)}{\hbar}\sum_j a_j^h(t)\,\langle\phi_n^e|\,\mu\,|\phi_j^h\rangle \exp\left[\frac{i}{\hbar}(E_n^e - E_j^h)\,t\right]. \tag{3.14}$$

At this point, the usual approximation of first-order perturbation theory is used. This consists of assuming that the laser field is sufficiently weak such that all of the coefficients in Equation (3.14) are essentially equal to their initial values. Specifically $a_1^h = 1$ while $a_{i\neq 1}^h = 0$. Then, the coefficients require that only the initially occupied state, $|\phi_1^h\rangle$, contributes giving

$$b_n^e(t) = \frac{i}{\hbar}\langle\phi_n^e|\,\mu\,|\phi_1^h\rangle \int_0^t dt'\, E\,(t')\, e^{i\omega_{n1}t'} \tag{3.15}$$

where $\omega_{n1} = (E_n^e - E_1^h)/\hbar$. This leads to an expression for the electronic wave packet as

$$|\Psi_{wp}(t)\rangle = \frac{i}{\hbar}\sum_n |\phi_n^e\rangle\langle\phi_n^e|\,\mu\,|\phi_1^h\rangle \int_0^t dt'\, E\,(t')\, e^{-i\omega_{n1}(t-t')} \tag{3.16}$$

where the heavy hole energy level has been taken as the zero of energy. For computational reasons a "promoted" wave packet is defined as

$$|\Psi_{wp}^0(\tau)\rangle = \frac{i}{\hbar}\sum_n |\phi_n^e\rangle\langle\phi_n^e|\,\mu\,|\phi_1^h\rangle\, e^{-i\omega_{n1}\tau}, \tag{3.17}$$

which is propagated over the relevant time period from zero to the final time t. This quantity can be calculated once and stored, avoiding a new propagation for each new laser field. The wave packet in the presence of the field is

$$|\Psi_{wp}(t)\rangle = \int_0^t d\tau\, E(t-\tau)\,|\Psi_{wp}^0(\tau)\rangle. \tag{3.18}$$

3.2 Control Theory

The optimal laser conditions for a given control objective can be determined by a variety of means.[147–150] One method uses Optimal Control Theory to determine the laser field that achieves a desired control objective. It has been demonstrated previously that the globally optimal field, in the weak response limit, can be calculated by diagonalizing a specially constructed control kernel.[65,66] An alternative method is to parameterize the laser pulse in a reasonable functional form, and simply search for the optimal parameters numerically. Past experience has shown that conventional

search routines such as conjugate gradient are insufficient to obtain the optimal parameters, because they tend to get trapped in local minima. Previous work has found that a genetic algorithm converges to the optimal parameters, with none of the difficulties encountered with more traditional methods.[136] Numerous implementations of the genetic style algorithm are available. One of the more popular versions, called GENESIS[151] is used here.

In this work, the laser pulse is described as

$$\varepsilon(t) = E(t)\, e^{-i\omega_L(t-\bar{t})} + E^*(t)\, e^{i\omega_L(t-\bar{t})}, \tag{3.19}$$

where $E(t)$ and $E^*(t)$ are slowly varying, complex envelope functions. The true laser frequency is assumed to have two parts, a large carrier frequency (ω_L) that excites the initial state to the middle of the electronic band of interest, and a small residual frequency (ω) known as the frequency detuning, which is contained in the envelope function. Note that the equation for the electronic wave packet does not contain both terms in the laser expression. The rapidly oscillating, counter-rotating term has been dropped according to the rotating wave approximation (RWA) (Appendix B). The envelope function is parameterized in the following form,

$$E(t) = E_0\, e^{-(t-\bar{t})^2/2\Gamma^2} e^{-i\phi(t)}. \tag{3.20}$$

Here, E_0 is the amplitude, $\bar{t}$ is the center time, and Γ is the temporal width, with a full-width at half-maximum (FWHM) of $\Gamma\sqrt{\ln 16}$. The amplitude E_0 is irrelevant in the weak response regime considered here, because the population in the conduction band is small, and scales linearly with the laser intensity. The time dependent phase, $\phi(t)$, can be expanded in a Taylor series as

$$\phi(t) = \phi + \omega(t-\bar{t}) + \frac{b}{2}(t-\bar{t})^2 + \ldots, \tag{3.21}$$

where ϕ is an irrelevant phase factor, ω is the frequency detuning, and b is the linear chirp. The four parameters ω, Γ, $\bar{t}$ and b allow sufficient flexibility to determine the optimal laser pulses for a wide range of experimental conditions and control objectives.

The genetic algorithm is a general purpose minimization routine that requires a test function as input. More information regarding genetic algorithms can be found in Appendix D. The projection of the electronic wave packet onto a target state is chosen as the test function for the algorithm to optimize. For historical reasons this is called the achievement.[66] Assuming that the target state, χ, and the wave packet are normalized, the achievement is given as

$$\alpha(t) = |\langle \chi | \Psi_{wp}(t) \rangle|. \tag{3.22}$$

The probability that the electronic wave packet resides in the target state is α^2. As defined in this equation, α ranges from zero to one, corresponding to no control and perfect control, respectively.

3.3 Controlling Carriers in a Double Well

Control of electronic wave packets in the ADQW (Figure 3–1) are considered. The material parameters and effective masses are taken from Leisching[9] with $x = 0.1$, and a 60:40 band gap offset. The objective is to find an optimized light pulse that excites charge carriers across the band gap, and drives a wave packet to maximum overlap with a Gaussian target distribution in the narrow well at a chosen time. The control parameters are limited to the frequency detuning, center time, and pulse width. For this target, the linear chirp has minimal effect, and therefore is not included in the optimization. The dc field is set to -10.5 kV/cm, which brings the lowest two electronic states to their smallest energy splitting, while the hole states diverge energetically.

For the control scenario depicted in Figure 3–1, the optimal parameters are $\omega = -33.8$ cm^{-1}, $\bar{t} = 507$ fs, and $\Gamma = 129$ fs. Recall that ω is measured relative

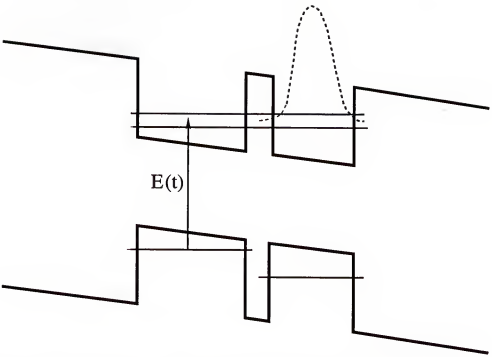

Figure 3–1: Schematic of the biased ADQW. The wide well is 145 Å, and the narrow well is 100 Å. The two wells are separated by a barrier of 25 Å. A laser pulse, $E(t)$, excites from the lowest heavy hole state to the lowest electronic mini-band. The target is a Gaussian distribution centered in the narrow well (dotted line). Adapted from K. L. Shuford and J. L. Krause, Int. J. Quant. Chem. **77**, 393 (2000).[152]

to the center of the two lowest electronic states in the conduction band (ω is the detuning, not the center frequency). This laser pulse produces an achievement of $\alpha = 0.99$, indicating nearly perfect control at the target time of 2.0 ps. The induced state is a coherent superposition (wave packet), and hence is not stationary. Figure 3–2 displays the evolution of the achievement. As can be seen in the figure, the wave packet completes 2.5 oscillations before landing in the target well at the target time. Notice that since the present model contains no dephasing, the period and depth of the oscillations are determined completely by the excitation process, and the wave packet will continue to oscillate indefinitely. Experiments observe signals from wave packet motion that persist for tens of picoseconds, allowing approximately ten oscillations.[10,127] The inevitable phase-breaking events do not significantly decrease the control achieved over the short time periods discussed above. The target distribution,

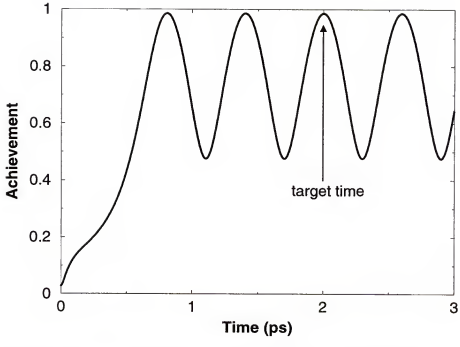

Figure 3–2: Achievement as a function of time for the optimal laser pulse. An achievement of one represents perfect control. Adapted from K. L. Shuford and J. L. Krause, Int. J. Quant. Chem. **77**, 393 (2000).[152]

and the probability density of the wave packet at the target time are shown in Figure 3–3. The overlap of the wave packet with the target is nearly perfect, as expected from the value of the achievement. Small discrepancies in center position and width of the distribution do not affect the achievement significantly.

3.4 Tests of Robustness

The likelihood that the control scheme is successful experimentally is greatly improved if the results are robust against possible variations in conditions. The effects of variations of the laser detuning and the center time have been analyzed, and Krause et al.[136] find that the results are rather insensitive to the pulse width, but fairly sensitive to the detuning and the center time. As a further test of the robustness of these results, the effect of varying the magnitude of the dc field is considered. The optimized laser parameters for a dc field of -10.5 kV/cm are left unchanged, while the field is allowed to vary over a large range. As expected, the

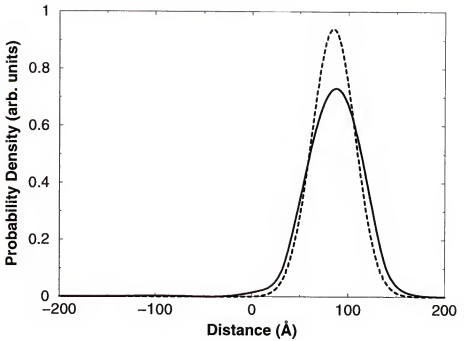

Figure 3–3: Wave packet (solid line) and the target (dashed line) at the target time. Adapted from K. L. Shuford and J. L. Krause, Int. J. Quant. Chem. **77**, 393 (2000).[152]

achievement falls off rather quickly as the field shifts away from -10.5 kV/cm as seen in Figure 3–4. The dc field Stark shifts the electronic energy levels. Keeping the laser conditions constant, and varying the dc field changes the relative components and frequency of the excited wave packet, which in turn affect the oscillation period. The peaks of high achievement seen in Figure 3–4 occur when the wave packet is in phase with the original wave packet created under the optimized conditions. The middle of the graph displays a region where essentially a single state is excited, and hence the achievement does not vary as much. The oscillations on the right portion correspond to a wave packet confined to the wide well, and therefore overlap with the target is minimal. However, for many values of the dc field the laser field can be re-optimized to produce an achievement of in excess of 0.98 as displayed in Figure 3–4. These results show that control is possible over a wide range of dc fields, but

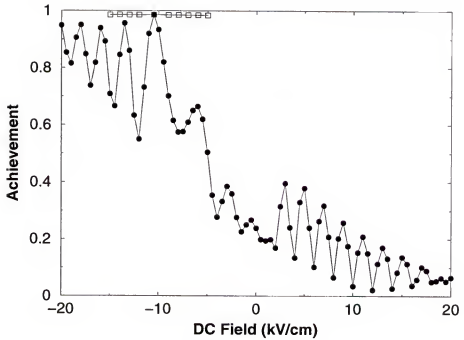

Figure 3–4: Achievement as a function of the dc field using the laser pulse optimized for −10.5 kV/cm (filled circles), and re-optimized pulses at each value of the field (open squares). Adapted from K. L. Shuford and J. L. Krause, Int. J. Quant. Chem. **77**, 393 (2000).[152]

once the laser pulse is optimized to a specific value of the field, slight changes in the field can dramatically reduce the achievement.

The effects of defects in the potential profile are considered as another test of the robustness of the results. The physical basis of such defects could be impurities in the samples, or variations in the stoichiometry of materials. Two styles of defects are modeled. Specifically, they are a point defect and a notch defect, or dislocation, as shown in Figure 3–5. For both types of defects, the achievement varies inversely with the magnitude of the defect using the optimal laser parameters in the absence of the defect. Once again, re-optimizing the pulse parameters allows the laser field to compensate for the defect, producing achievements of over 0.97 in all cases investigated. The results are summarized in Table 3–1. In most cases, the defect causes the electronic energy levels to be repelled, requiring an increase in center frequency and band width of the laser pulse.

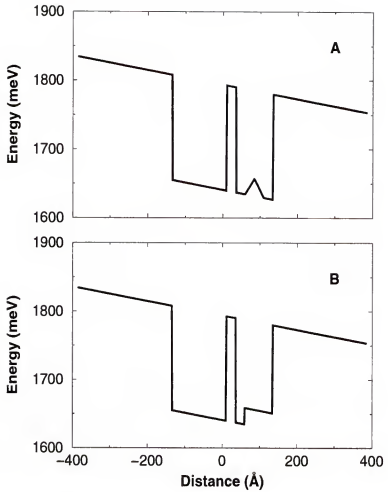

Figure 3–5: Potential profiles with model defects. A) Point defect of 25 meV; B) Notch defect of 75 Å. Adapted from K. L. Shuford and J. L. Krause, Int. J. Quant. Chem. **77**, 393 (2000).[152]

As a final test of the robustness of our results, the electronic wave packet in the ADQW is coupled to a harmonic bath, consisting in this work of a single oscillator. The aim is to include the effects of phonons in the model, as an example of a dissipation mechanism. The preliminary results presented here are a first step towards including such interactions.

The time-dependent Hartree (TDH) approximation[119,153–158] is adopted to calculate the effects of coupling to the oscillator. The TDH approximation is a variational method for finding solutions to the time-dependent Schrödinger equation. It

Table 3–1: Effects from Sample Imperfections[a]

Dislocation (Å)	α_0	α_{new}	Point (meV)	α_0	α_{new}
0	0.99	—	0	0.99	—
25	0.85	0.99	10	0.87	0.98
50	0.43	0.98	15	0.73	0.98
75	0.20	0.97	20	0.73	0.98
100	0.16	0.97	25	0.37	0.98

[a] The achievement using the original pulse is designated α_0, and the achievement using a newly optimized pulse is α_{new}. In all cases the GA can compensate for the perturbation, and find a new pulse to overcome the defect.

is attractive because it factorizes a complicated N-dimensional problem into N one-dimensional problems. Each component of the total wave function feels an interaction potential averaged over the densities of the other subsystems. As has been well-documented, the TDH approximation tends to work well at short times, and when the bath modes are uncorrelated. It tends to fail at long times, when correlation is extremely important, or when calculating properties that are strongly dependent on the system as a whole.

The total Hamiltonian is given as a sum of the individual Hamiltonians, and an interaction potential. In this work, a linear interaction is chosen as

$$V_{int}(z,x) = -c\,z\,(x - x_{eq}), \tag{3.23}$$

where c is a constant governing the strength of the coupling between the ADQW and the oscillator, and x_{eq} is the equilibrium position of the oscillator. The Hartree product wave function is wave packet in the conduction band in the absence of the laser field (i.e., the equivalent of the promoted state discussed above) multiplied by a harmonic oscillator state, $\Psi^0_{wp}(z,t)\,\phi_x(x,t)$. With the form of the coupling given in Equation (3.23), and the TDH form of the wave function, the equations of

motion[119,153] for the individual components are,

$$i\hbar\frac{\partial\Psi^0_{wp}}{\partial t} = \left\{H^e + \frac{c^2}{2\,\mu\,\nu^2}\,z^2 + \langle\phi_x \,|\, V_{int}\,|\phi_x\rangle\right\}\Psi^0_{wp}, \tag{3.24}$$

and

$$i\hbar\frac{\partial\phi_x}{\partial t} = \left\{-\frac{\hbar^2}{2\mu} + \frac{\mu\,\nu}{2}\,x^2 + \langle\Psi^0_{wp}\,|\,V_{int}\,|\,\Psi^0_{wp}\rangle\right\}\phi_x, \tag{3.25}$$

where H^e is the Hamiltonian given in Equation (3.2), μ is the reduced mass of the oscillator, and ν is the oscillator frequency. The term containing c^2 is included to prevent the depth of the wells from depending on the coupling strength.[155] The equations above differ from the original Hartree product by a phase factor. The corrected wave function is then

$$\Psi(z,x,t) = e^{i\,\theta(t)}\Psi^0_{wp}(z,t)\,\phi_x(x,t), \tag{3.26}$$

where $\theta\,(t)$ is the expectation value of the interaction between the electron and the harmonic oscillator

$$\theta\,(t) = \int_0^t d\tau\,\langle\Psi^0_{wp}(z,\tau)\,\phi_x(x,\tau)\,|\,V_{int}(z,x)\,|\,\Psi^0_{wp}(z,\tau)\,\phi_x(x,\tau)\rangle. \tag{3.27}$$

The target is chosen to be a Gaussian distribution in the narrow well, as in the examples presented above. Since the target does not depend on the oscillator coordinate, the coupling affects only the promoted wave packet. The electronic wave packet created by the laser field can then be determined via a convolution over the laser pulse, as in Equation (3.18). For convenience, the initial state of the oscillator is chosen to be a Gaussian centered at x_{eq},

$$\phi_x = \left(\frac{\mu\nu}{\pi}\right)^{1/4} e^{-(1/2)\,\mu\,\nu\,(x-x_{eq})^2}, \tag{3.28}$$

with a mass equal to the effective mass of the electron in the conduction band, and a frequency of 50 cm^{-1}.

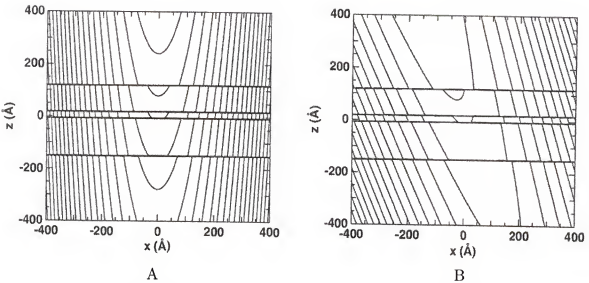

Figure 3–6: Effective potential for an ADQW coupled to a harmonic oscillator. A) Potential for zero coupling; B) Potential for a coupling of 1.6×10^{-2} g/s^2. Adapted from K. L. Shuford and J. L. Krause, Int. J. Quant. Chem. **77**, 393 (2000).[152]

In the case of coupling to a single oscillator, the (exact) dynamics involves propagation on a two-dimensional potential surface. Figure 3–6 shows the potentials for zero coupling, and a moderately strong coupling. As can be seen in the figure, a coupling of 1.6×10^{-2} g/s^2 is sufficient to distort the potential significantly. However, this distortion does not completely eliminate the control, nor does it diminish the controllability. Figure 3–7 shows the wave packet created with the parameters of the laser field set to the optimal parameters for the case of zero coupling. The achievement drops to 0.89, but most of the wave packet density still lands in the target well at the target time. Re-optimizing the parameters of the laser field leads to nearly perfect control. All three parameters change significantly in the re-optimization, with the biggest change in the frequency detuning. Unlike in the examples discussed previously, there is no intuitive explanation for the the observed changes in the parameters. Figure 3–8 displays the result of increasing the coupling by a factor of ten. The achievement drops to 0.19 using the optimal parameters for zero coupling. Re-optimizing increases the achievement to 0.69, but as can be seen in the figure, the

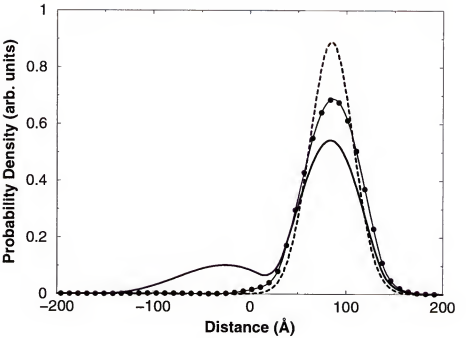

Figure 3–7: Wave packet produced at the target time using a laser pulse optimized for zero coupling (solid line) and the re-optimized pulse for a coupling of 1.6×10^{-2} g/s^2 (filled circles). The target is indicated as a dashed line. Adapted from K. L. Shuford and J. L. Krause, Int. J. Quant. Chem. **77**, 393 (2000).[152]

final wave packet cannot reach the target region with high probability in the presence of large coupling. These results suggest that a strong coupling to the environment, resembling fast dissipation, can be detrimental to complex control schemes.

3.5 Chirped Laser Pulses in a Superlattice

In this section, the control objective used for the ADQW is extended to a more complex system, specifically a twelve-well superlattice (SL). A schematic of the SL can be seen as Figure 3–9. The wide well is 130 Å followed by ten 95 Å wells, and an 80 Å narrow well. The widths of all barriers are 17 Å. The same material parameters[9] are used as in the ADQW to model the energetics with $x = 0.25$, and a bad gap offset of 65:35. The conduction band contains approximately twenty-four bound states grouped in two mini-bands of twelve states each. Again excitation takes place from the lowest heavy hole state (wide well), creating a time-evolving wave

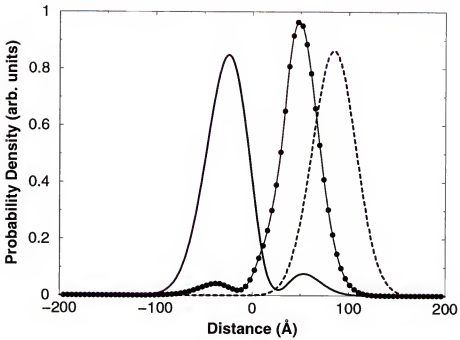

Figure 3–8: Wave packet produced at the target time using a laser pulse optimized for zero coupling (solid line) and the re-optimized pulse for a coupling of 1.6×10^{-1} g/s^2 (filled circles). The target is indicated as a dashed line. Adapted from K. L. Shuford and J. L. Krause, Int. J. Quant. Chem. **77**, 393 (2000).[152]

packet composed of the excited mini-band states. The goal is to create maximum electron density in the narrow well at the target time.

Initially the dc field is set to zero, and the GA searches for laser parameters that localize the charge density in the narrow well at 4 ps. For this problem, the GA finds numerous solutions with approximately the same achievement. Care must be taken when optimizing the parameter sets so that the value of the chirp does not exceed reasonable values (Appendix F). Some examples of typical parameter sets are listed in Table 3–2.

Several general trends emerge from the optimization of this system. Transform limited pulses ($b = 0$) have smaller values of the detuning (relative to the lowest electronic state), a center time closer to the target time, and wider widths relative to the chirped pulses. While optimizing the system with a chirped pulse, b varies wildly between runs until settling on a particular region of parameter space. All other

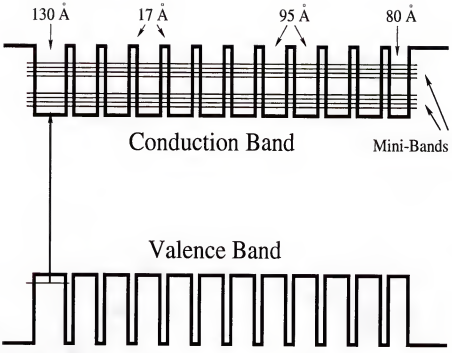

Figure 3–9: Schematic of a twelve-well superlattice. The wide well is 130 Å followed by ten 95 Å wells, and a narrow well of 80 Å. The conduction band contains two mini-bands composed of twelve states. The objective is to create density in the narrow well at the target time.

parameters are slowly varying and change in predictable manners until converging. Looking at the data sets with positive chirps (a and b), the center time is $\approx$ 500 fs earlier than the data sets corresponding to negative chirps (c and d). Also notice that set (d) has the smallest magnitude of the chirp (when a chirp is present), and it generally follows the trends mentioned earlier for pulses with no chirp. The data in Table 3–2 illustrates that there are several possible solutions to this problem that produce nearly the same results, each with a slightly different means of achieving high performance.

Further study of data sets (a) and (e) show that they produce very similar dynamics even though the laser pulses are quite different as can be seen in the Wigner representations displayed in Figure 3–10. Projections onto the excited states at the final time show that the wave packet is composed primarily of States 11 and 12. Significant population is limited to only these two states, with 90% in the latter.

Table 3–2: Optimized Laser Parameters[b]

Data Set	ω (cm^{-1})	$\bar{t}$ (fs)	Γ (fs)	b (cm^{-1}/fs)	α
a	332.2	1254	225.2	0.05	0.728
b	334.1	1202	219.4	0.05	0.727
c	341.1	1768	207.0	−0.05	0.728
d	308.2	1882	234.7	−0.03	0.728
e	284.3	2106	266.7	0	0.730
f	280.3	2124	281.1	0	0.730

[b] The genetic algorithm finds the most suitable parameter values for the superlattice structure with no bias applied.

Essentially, the laser pulses pump States 11 and 12 to drive electronic density into the narrow well. The SL stationary states possess the characteristic that the state number corresponds to the well with the greatest amount of density, however some density does leak into adjacent wells. Since State 12 is primarily localized in the target well, it is reasonable that the GA would seek solutions that excite mostly this state.

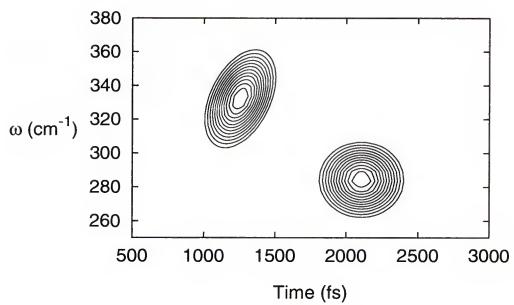

Figure 3–10: Wigner distributions for data sets (a) and (e) in Table 3–2. The pulse occurring at 1200 fs is data set (a), while the pulse occurring at 2100 fs is data set (e). The two pulses are significantly different, however both produce approximately equal achievements.

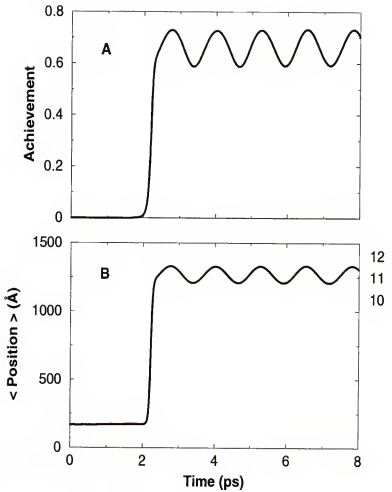

Figure 3–11: Wave packet properties as a function of time for data set (a) in Table 3–2. A) Time evolution of the achievement; B) Time evolution of the expectation value of position. The numbers on the right side of Panel B are the well numbers that correspond to each distance. These plots are representative of all the sets listed in Table 3–2. A smooth, periodic curve is shown in both panels.

Figure 3–11A shows the achievement as a function of time for set (a). This curve shows a regular, periodic motion corresponding to a single frequency. The period of the oscillation is ~ 1.26 ps $= 1/(E_{12} - E_{11})$ as expected from the population data. A Fourier analysis of the time signal confirms this assignment with a peak at the energy splitting of these two states. Figure 3–11B displays the expectation value of position as a function of time for the induced wave packet. Figure 3–11 shows that wave packet motion never returns to the left side of the potential after initial

excitation, and essentially oscillates between wells ten and twelve. Note that the period of oscillation is well-defined, and identical in both panels.

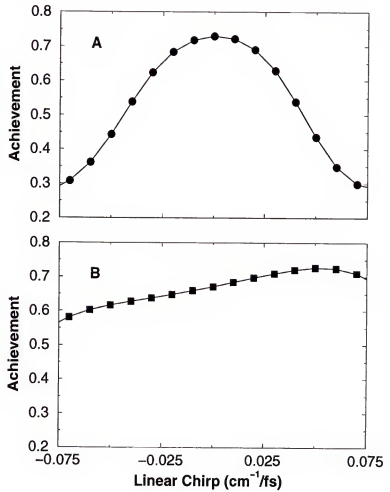

Figure 3–12: Achievement as a function of chirp variation. A) Effect on achievement by adding chirp to data set (e) in Table 3–2; B) Effect on achievement by varying the chirp in data set (a) in Table 3–2. All other parameters are set to the optimized values while b is allowed to vary. In both plots the maxima correspond to the optimized value of the linear chirp.

The effects on the achievement caused by fluctuations in the chirp parameter are also investigated. The other three laser parameters are fixed at their optimized values while the chirp parameter is allowed to vary in an experimentally physical range. Figure 3–12 displays the achievement under these conditions. In both panels, the maximum corresponds to the optimized chirp values. As expected, the achievement

declines as the linear chirp is shifted from the optimized value. Note that data set (e) is very sensitive to the value of the chirp. As a chirp is added to this set the achievement value drops considerably, by as much as 0.4, while data set (a) drops by a maximum of only 0.15. This indicates that the data set optimized including a chirp is much more robust against variations in linear chirp.

Upon applying a small dc field, the system dynamics are much more complex. When the dc field is -0.58 kV/cm, the energy difference between State 12 and State 1 is minimized. This value of the bias field is chosen for the optimizations. Again the GA optimizes the excitation pulse, and yields several acceptable solutions. In accord with previous optimizations in the ADQW, a linear chirp is not imperative to achieve good control of system dynamics. In many cases, all parameters are similar except for the addition of a chirp. The transform limited pulses perform consistently better than chirped pulses, and thus are the only results reported here. One parameter set with high achievement ($\alpha = 0.721$) is $\omega = 182.2$ cm^{-1}, $\bar{t} = 1778$ fs, and $\Gamma = 547.4$ fs. The dynamics of the wave packet show distinct differences compared to the flatbed conditions (dc = 0). The wave packet is not localized spatially, and oscillates across the entire potential surface. Projections of the wave packet onto the basis states at the center time of the excitation pulse show a wide distribution of states populated initially. Following the laser pulse as many as one-third of the states in the first miniband play a role in the time evolution. This is in contrast to the results at zero dc field, in which only two states are populated. With the presence of the added components, the wave packet exhibits much more complex dynamics. Figure 3–13 displays the time evolution of the achievement and average position, and reveals this complexity. This is in striking contrast to Figure 3–11, which exhibits a single, dominant period and frequency. It is evident that this wave packet has a complex phase relationship with multiple frequencies present. The expectation value of position does not parallel the achievement as in the earlier cases. The wave packet splits and reforms several

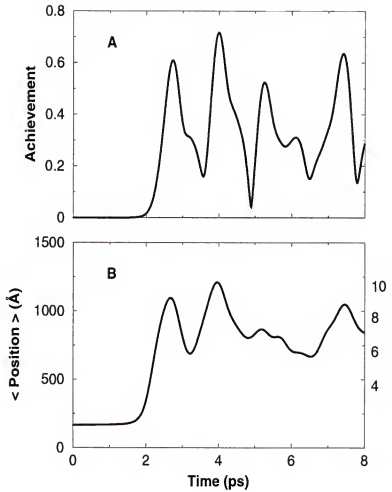

Figure 3–13: Wave packet properties as a function of time. A) Time evolution of the achievement; B) Time evolution of the expectation value of position. The numbers on the right side of Panel B are the well numbers that correspond to each distance. The curves are much more complex when the dc field is set to -0.58 kV/cm than under zero bias conditions.

times over the time investigated. At some time steps the electron density is found on both sides of the potential, leading to an average value between the two extremes. However, the achievement is at a maximum at the target time as required by the optimization.

3.6 Conclusions

This chapter considers the control of electronic wave packets in an asymmetric double quantum well (ADQW) and a multi-well superlattice (SL). A relatively simple model and control scheme are used to investigate the major contributions to the dynamics in semiconductor quantum wells under typical experimental conditions, as well as assess the feasibility of controlling charge carriers in such systems. In both systems, significant control of electronic dynamics is possible with simple, experimentally achievable laser pulses. As expected, the dynamics in the SL are much more complex due to numerous states and couplings in the multi-well potential.

A number of factors are investigated that might be expected to affect the control in the ADQW. In particular, the results are quite sensitive to the magnitude of the static dc field, however the parameters of the laser pulse can be adjusted to achieve control over a broad range of conditions. This implies that once the optimal laser parameters for a particular value of the dc field are determined, large fluctuations or drifts in the field can adversely affect control.

Also examined are the effects of two defects, a point defect and a notch. Once again, control is robust to fairly large defects, and the parameters of the optimal pulse can be re-adjusted to compensate for such defects. The changes in the values of the optimal pulse parameters are not simple to predict, though some trends do emerge, such as the tendency to adjust the bandwidth and center frequency as the size of the defect increases. If the defects are made large enough, the controllability is adversely affected. However, current technology can produce structures with defects smaller than the extreme cases considered here.

Environmental effects are considered by coupling the wave packet in the conduction band to an additional degree of freedom, a harmonic oscillator. A sizeable coupling causes a significant distortion in the effective potential, yet is not sufficient to

eliminate the control. Re-optimizing the laser pulse allows the dynamics to compensate for the coupling. However, increasing the coupling eventually causes sufficient distortion in the potential such that no laser pulse can achieve a large overlap with the target. The changes in the laser parameters as a function of the coupling strength are not intuitive in this case, and no general trends emerge.

In both of the systems investigated, multiple solutions to the control problem posed are evident. Numerous, widely varying parameter sets are obtained, all yielding approximately the same value of the achievement. The linear chirp is shown to vary in an inconsistent manner, and quite erratically among the various optimizations. Within an optimized parameter set, the magnitude of the chirp is important, but generally the sign of the chirp is neither significant, nor consistent. In each case studied there is a transform limited pulse that produces the same achievement. This leads to the conclusion that a chirped pulse is not imperative, and is not necessary to control carrier dynamics in the structures under conditions investigated here.

As a final note, the results in this study indicate clearly the potential value of adaptive learning or feedback control in quantum well experiments.[75] Control in these systems is apparently quite robust, and in most cases studied here, a precise value for a given parameter is not necessary, provided the laser pulse is allowed to adjust to changes in the experimental conditions.

CHAPTER 4
COULOMB EFFECTS

Chapter 3 demonstrates that relatively simple laser pulses can be used to control the dynamics of electronic wave packets in quantum wells. Specifically, wave packets in asymmetric double quantum wells (ADQW) and superlattices (SL) can be driven to maximum overlap with a target distribution at a desired time. The robustness of these results has been analyzed by testing their sensitivity with respect to several effects such as fluctuations in the dc field, sample defects, and coupling of the system to a harmonic bath modeling phonons. It has also been found that given a predetermined, fixed laser pulse, the dimensions of the structure can be varied to maximize the overlap with the target distribution.[136]

These studies use an effective Hamiltonian approach within the envelope approximation. This allows the use of control methods developed previously for the Schrödinger, wave function formalism. In this chapter, the previous formalism is expanded to include the effects of Coulomb interactions present in excitons. The interaction is introduced in a dynamic fashion based on the instantaneous separation of electrons and holes. This concept has been used previously to examine the dynamics of an electrically pumped exciton created by hole-assisted resonant tunneling.[159,160]

A laser field excites the QW system producing transitions across the band gap. As a result, excited electrons reside in the conduction band, while holes are present in the valence band. A time-dependent attraction develops between the charge carriers. The electron and hole are represented by wave packets in their respective bands, which evolve according to the quantum well potentials and the Coulomb interaction between them. The propagation of the coupled system produces a dynamic view of the exciton evolution, and the time-dependent potential on which the system evolves.

The current model neglects many-body effects (carrier-carrier interactions). This assumption is reasonable when a weak laser pulse excites the system. The small number of photons limits the carriers per well to $\leq 10^{10}$ cm^{-2}. The intraband damping rate of optically excited wave packets under these conditions is density independent at low carrier density (1×10^8–1.5×10^9 cm^{-2}),[161] indicating that carrier scattering is minimal when the excitation is in the weak response regime. Most experiments in quantum well systems are performed at low temperatures ($\sim$ 10 K). The cryogenic conditions also justify the neglect of phonon interactions. In fact, experimental observations show coherent oscillations from optically excited wave packets persisting up to 12 ps.[10] Dephasing is not addressed in the current model because the controlled wave packet motion occurs on a much faster time scale than the relevant damping and recombination processes. The model used in this work accurately portrays the conditions under which most experiments are performed, and is valid in describing the dominant contributions to the system dynamics. As shown below, this model allows emphasis to be placed on the major physical process not considered in previous work, allowing the evaluation of its influence on the dynamics and the controllability of the carriers in a quantum well.

4.1 Theoretical Model

The symmetry of the quantum well system allows the use of cylindrical coordinates (ρ, ϕ, z), where z is the growth direction, ρ is the distance from the z axis, and ϕ is the projection on the x–y plane. The dimensions perpendicular to z are separated into center of mass and relative coordinates. Within the effective-mass, envelope approximation the Hamiltonian for an electron and a heavy hole interacting via a Coulombic potential is

$$\mathcal{H} = H_e(z_e) + H_h(z_h) + T_{rel}(\rho, \phi) + V_{coul}(\rho, z_e - z_h), \tag{4.1}$$

in which the center of mass motion has been neglected. The terms in the preceding equation are defined as

$$H_e = -\frac{\hbar^2}{2m_e^*}\frac{\partial^2}{\partial z_e^2} + V_e(z_e) + eFz_e, \tag{4.2}$$

$$H_h = -\frac{\hbar^2}{2m_h^*}\frac{\partial^2}{\partial z_h^2} + V_h(z_h) - eFz_h, \tag{4.3}$$

$$T_{rel} = -\frac{\hbar^2 \nabla_\rho^2}{2\mu_\perp}, \tag{4.4}$$

and

$$V_{coul} = -\frac{e^2}{4\pi\epsilon_0\epsilon}\frac{1}{\sqrt{\rho^2 + (z_e - z_h)^2}}, \tag{4.5}$$

where $m_{e,h}^*$ are the effective masses in the dimension parallel to the growth direction, $\mu_\perp$ is the reduced mass in the perpendicular plane, $V_{e,h}$ are the confining QW potentials, F is a static dc field, and ϵ is an average dielectric constant. The materials considered in this work are $GaAs/Al_xGa_{1-x}As$ with $x = 0.2$, and a 65/35 band gap offset. Structural parameters[162,163] for this system are $E_{gap}^{GaAs} = 1.52$ eV, $E_{gap}^{AlGaAs} = 1.78$ eV, $m_e^* = 0.0665\ m_0$, $m_h^* = 0.34\ m_0$, $\mu_\perp = 0.0415\ m_0$, where m_0 is the bare electron mass, and $\epsilon = 12.15$.

The complete exciton wave function is approximated by the product trial function

$$\Phi(z_e, z_h, \rho) = \psi_e(z_e)\,\psi_h(z_h)\,\psi_{rel}(\rho), \tag{4.6}$$

where ψ_e and ψ_h are the single particle eigenstates obtained by solving the Schrödinger equation for the electron and hole with the Hamiltonians in Equation (4.2) and (4.3), respectively. The in-plane motion is represented by the variational wave function

$$\psi_{rel}(\rho) = \sqrt{\frac{2}{\pi}}\frac{1}{\lambda}\exp\left[\frac{-\rho}{\lambda}\right], \tag{4.7}$$

where λ is a parameter that is varied to minimize the energy. This choice of wave function corresponds to a 1s orbital, and is accurate for quantum wells up to 100 Å

wide.[163] Larger quantum wells require wave functions coupling all dimensions in the exponential to yield reliable results.[164]

The expectation value of the energy for the exciton system is

$$\langle \Phi | \mathcal{H} | \Phi \rangle = E_e + E_h - E_b, \tag{4.8}$$

where E_e and E_h are the energy of the electron and heavy hole respectively, and E_b is interpreted as the exciton binding energy. Two terms contribute to the binding energy,

$$-E_b = \int_0^{2\pi} \int_0^{\infty} \psi_{rel}^* T_{rel} \psi_{rel} \rho \, d\rho \, d\phi + \langle \Phi | V_{coul} | \Phi \rangle. \tag{4.9}$$

The first expression on the right hand side can be evaluated analytically as $\hbar^2/2\mu\lambda^2$. The second term written explicitly is

$$\int_{dz_h} \int_{dz_e} \int_0^{2\pi} \int_0^{\infty} \psi_e^* \psi_h^* \psi_{rel}^* V_{coul} \psi_e \psi_h \psi_{rel} \, d\tau, \tag{4.10}$$

where $d\tau = \rho \, d\rho \, d\phi \, dz_e \, dz_h$. Simplifying this expression gives

$$-\frac{e^2}{4\pi\epsilon_0} \frac{4}{\epsilon\lambda^2} \int dz_e \, \psi_e^* \psi_e \int dz_h \, \psi_h^* \psi_h \int_0^{\infty} d\rho \, \frac{\rho \, e^{-2\rho/\lambda}}{\sqrt{\rho^2 + (z_e - z_h)^2}}. \tag{4.11}$$

Note that $e = 4\pi\epsilon_0 = 1$ in atomic units. The integral over ρ can be solved as

$$|z_e - z_h| \left\{ \frac{\pi}{2} \left[H_1(\xi) - Y_1(\xi) \right] - 1 \right\}, \tag{4.12}$$

where $\xi = \frac{2}{\lambda} |z_e - z_h|$, H is a first order Struve Function, and Y is a Bessel Function of the second kind.

In the present model, the binding energy is interpreted as an energy shift resulting from the Coulomb interaction. The attractive potential shifts the Coulomb-free energy levels in the confined dimensions, decreasing the transition frequencies across the bandgap in agreement with experiment.[162,163] The energy shifts are defined as

$$W_i = \langle \psi_i | \psi_i \rangle \, E_b, \tag{4.13}$$

where $i = \{e, h\}$, W_i is the interaction potential, and E_b is the binding energy. The Coulomb-free energy levels are shifted by a fraction of the binding energy as determined by the relative population of electrons present in each band. As the population of carriers in the conduction band increases, its energy level is shifted by a smaller percentage of the binding energy.

The ground state of the system consists of electrons in the valence band, while the conduction band is empty. Electrons are promoted via a laser pulse to the conduction band. The number of electrons in the excitation process is conserved, and gives the relation between the number of charge carriers in each band. Following the laser pulse, these populations become constants. Note that because of population changing bands, terms in Equation (4.8) need to be normalized accordingly.

The Coulomb interaction binds the particles more tightly than free particles in their respective bands, and lowers the energy of the exciton state. To model this effect, the hole energy increases (to a lower energy state) and the electron energy decreases, thus creating a less energetic, electron-hole pair. The resulting equations of motion for the wave packets, $\Psi_h(t)$ and $\Psi_e(t)$, are

$$i\hbar\frac{\partial}{\partial t}\Psi_h(t) = [H_h + W_e]\Psi_h(t) - \mu\,\varepsilon(t)\Psi_e(t), \tag{4.14}$$

and

$$i\hbar\frac{\partial}{\partial t}\Psi_e(t) = [H_e - W_h]\Psi_e(t) - \mu\,\varepsilon(t)\Psi_h(t), \tag{4.15}$$

where μ is the transition dipole moment, and $\varepsilon(t)$ is the laser pulse. The form of the laser pulse is chosen as

$$\varepsilon(t) = E_0\,\exp\left[\frac{-(t-\bar{t})^2}{2\Gamma^2}\right]\cos(\omega\,t) = E(t)\,\cos(\omega\,t) \tag{4.16}$$

where E_0 is the amplitude, $\bar{t}$ is the center time, Γ is the pulse width, $E(t)$ is the pulse envelope, and ω is the laser frequency. Invoking the rotating wave approximation

(Appendix B) gives the following matrix equation describing the system dynamics,

$$i\hbar\frac{\partial}{\partial t}\begin{bmatrix}\Psi_h(t)\\ \Psi_e(t)\end{bmatrix} = \begin{bmatrix} H_h + W_e & -\frac{\mu E(t)}{2}\exp(i\Delta t) \\ -\frac{\mu E(t)}{2}\exp(-i\Delta t) & H_e - W_h \end{bmatrix}\begin{bmatrix}\Psi_h(t)\\ \Psi_e(t)\end{bmatrix}, \quad (4.17)$$

where Δ is the frequency detuning from the first electronic state. These equations are propagated using the split operator method (Appendix C).[165,166]

4.2 Test System

As a test of the model, a simple structure whose parameters are well-known is considered. The exciton binding energy[168] for GaAs/AlGaAs quantum wells with widths less than 100 Å is $\sim$ 9 meV. A variational calculation employing the method described above yields a binding energy of 8.67 meV for a 60 Å, unbiased quantum well. The dynamic model, which is based on the instantaneous particle separation, reproduces the experimental value under similar excitation conditions. Figure 4–1 shows the time evolution of the binding energy. The pulse is centered at 278 fs, and the frequency is tuned just below the bandgap ($\Delta = -E_b$). At the completion of the pulse, the binding energy exhibits slight oscillations around 8.67 meV. The oscillations are due to a small population of higher-lying states, and can be eliminated completely by exciting with a longer pulse. These results demonstrate that the calculated binding energy converges to the experimental value for a single-well structure. This is a strong indication that the interaction potentials can adequately account for the electron-hole Coulomb interaction.

4.3 Dynamics in Complex Systems

The next system considered is an asymmetric double quantum well (ADQW). This structure has been the focus of considerable experimental and theoretical research due to its simplicity, and the availability of high-quality experimental data regarding structure and dynamics.[2,6,10,127–131] The ADQW consists of two wells with dimensions of 80 Å and 40 Å, separated by a 20 Å barrier, as shown in Figure 4–2.

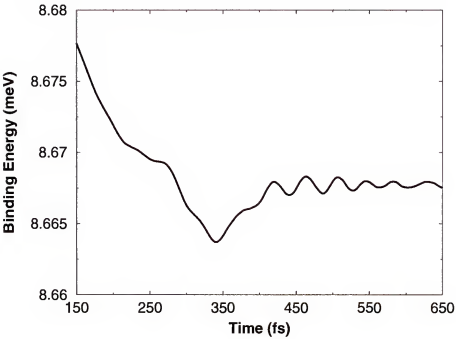

Figure 4–1: Time evolution of the exciton binding energy. The laser pulse is tuned to the first excitonic resonance with a center time of 278 fs. Adapted from K. L. Shuford and J. L. Krause, J. Appl. Phys. **91**, 6533 (2002).[167]

Application of a -18 kV/cm dc field brings the first two electronic energy levels into tunneling resonance, while the hole levels move out of resonance. This produces essentially a three-level system due to the large energy gap between higher-lying electronic states. The initial state is localized in the wide well of the valence band, and the target state is a Gaussian distribution centered in the narrow well of the conduction band. Excitation with a sufficiently narrow pulse creates a coherent superposition of two electronic states in the conduction band, which oscillates back and forth through the barrier with a frequency corresponding to the energy splitting. The goal is to find the laser pulse that drives the electronic wave packet to maximum overlap with the target distribution at a specified time.

The performance of a particular laser pulse is evaluated by an achievement function,

$$\alpha(t) = \frac{|\langle \chi \,|\, \Psi_e(t) \rangle|}{\langle \chi \,|\, \chi \rangle^{1/2} \langle \Psi_e(t) \,|\, \Psi_e(t) \rangle^{1/2}}, \tag{4.18}$$

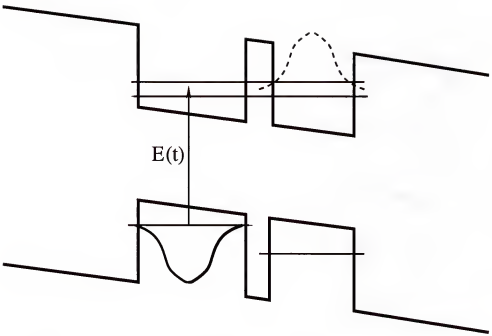

Figure 4–2: Schematic of the ADQW considered in this work. The width of the wide well is 80 Å, the width of the narrow well is 40 Å, and the barrier width is 20 Å. The initial state (solid line) is localized in the wide well of the valence band. The target distribution (dashed line) is centered in the narrow well of the conduction band. The goal is to create an electronic wave packet that produces maximum overlap with the target distribution at the target time of 550 fs. Adapted from K. L. Shuford and J. L. Krause, J. Appl. Phys. **91**, 6533 (2002).[167]

where χ represents the target state. The achievement is the normalized overlap of the electronic wave packet with the target state, and varies from zero to one corresponding to no control and perfect control, respectively.

Initially, the pulse parameters are optimized neglecting the Coulomb interaction ($W_{e,h} = 0$). A parameter set that performs well in this case is $E_0 = 2.57 \times 10^8$ V/m, $\Delta = 26$ meV, $\bar{t} = 297.3$ fs, and $\Gamma = 50$ fs. The achievement for these parameters is $\alpha = 0.98$, indicating nearly perfect overlap with the target state at the target time. The populations of the electronic eigenstates $|1\rangle$ and $|2\rangle$ following the laser pulse are 0.21 and 0.79, respectively. The lowest electronic eigenstate, $|1\rangle$, is localized in the wide well with a small density in the narrow well, while the second state, $|2\rangle$, is localized primarily in the narrow well, with a small density in the wide well. This

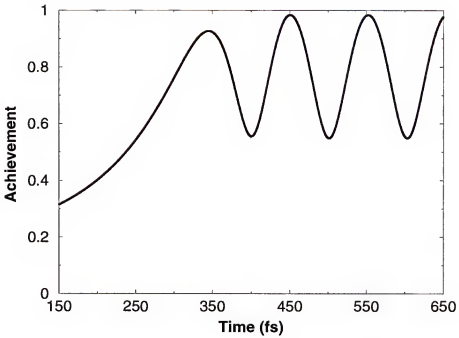

Figure 4–3: Achievement as a function of time. The wave packet completes two oscillations before arriving in the narrow well at the target time. Adapted from K. L. Shuford and J. L. Krause, J. Appl. Phys. **91**, 6533 (2002).[167]

ratio of components reflects the fact that the target is located in the narrow well, so additional character from the second state is required to produce density in this region. Limiting the excitation to State $|2\rangle$ gives a significantly lower achievement. Adding some character of State $|1\rangle$ allows the wave packet to propagate through the structure, and increases the achievement at the target time. Note that the peak amplitude, E_0, is restricted to values for which the population in the conduction band scales linearly with its field strength (i.e., the excitation is in the weak response regime). In this regime, the precise value of E_0 does not affect the control.

The next step is to optimize the laser parameters in the presence of the Coulomb interaction. This requires minimizing Equation (4.8) (maximizing the binding energy) at each time step, which adds to the computation time considerably. Experience based on tests with full optimization of all parameters indicates that the detuning is the most sensitive parameter in the presence of the Coulomb interaction. Within

this model, changing the detuning compensates for the shifts in energy due to the excitonic binding energy. This allows an adjustment of the eigenstate composition of the electronic wave packet. When the composition is similar to that in the Coulomb-free case, the achievement is also similar.

Figure 4–3 shows the achievement as a function of time in the presence of the Coulomb interaction. All parameters are the same as in the Coulomb-free case except for the detuning, which has been decreased 6 meV to $\Delta = 20$ meV. As can be seen in the figure, the achievement oscillates between 0.59 and 0.98. The peak achievement, which occurs at the target time, is identical to that in the Coulomb-free case.

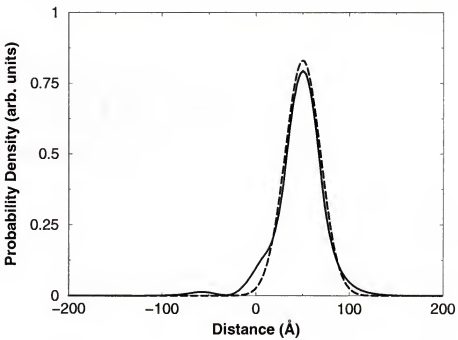

Figure 4–4: Probability density of the wave packet (solid line) and the target state (dashed line) at the target time. The achievement, α, is 0.981 at 550 fs indicating nearly perfect control. Adapted from K. L. Shuford and J. L. Krause, J. Appl. Phys. **91**, 6533 (2002).[167]

Figure 4–4 shows the target state probability and the density of the electronic wave packet in the presence of the Coulomb interaction. Once again, this figure illustrates that nearly perfect control is attained using the same parameters as in the Coulomb-free case, except for the detuning. Only a small amount of electron density

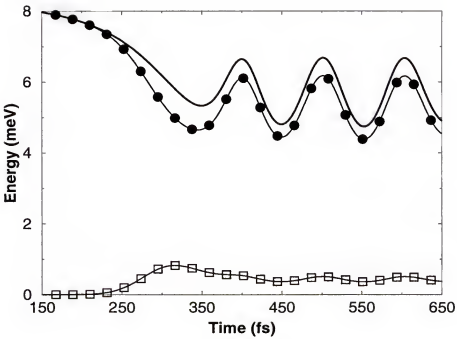

Figure 4–5: Time evolution of the exciton binding energy and interaction potentials. The contribution from the holes, W_h, is shown in the line with filled circles, and the contribution from the electron, W_e, is shown in the line with open squares. The solid line shows the total binding energy, which is the sum of the interaction potentials of the electrons and holes. Adapted from K. L. Shuford and J. L. Krause, J. Appl. Phys. **91**, 6533 (2002).[167]

remains in the wide well at $t = 550$ fs. Notice that the achievement never decreases to zero, indicating that some wave packet density always remains in the target well. In fact, most of the density is localized in the narrow well at all times. This is because the wave packet is 78% eigenstate $|2\rangle$, which is localized in that well.

The method used in this work also allows an examination of the dynamics in the valence band. The average position of the hole state is essentially a constant centered in the wide well. This is primarily due to the design of the structure, and the low pulse intensities used, which ensure that the hole wave packet in the valence band wave is confined to the wide well. The exciton binding energy oscillates with the period of the electronic wave packet as seen in Figure 4–5. The Coulomb interaction increases as the electronic wave packet moves closer to the wide well, which is the region in which the hole wave packet is localized, and then decreases as

it moves to the narrow well. The interaction potentials also oscillate at the frequency of the electronic wave packet, however their magnitudes are quite different. The interaction potential from the valence band (W_h) is significantly larger, with deeper oscillations, than the interaction potential from the conduction band (W_e). As a result, the contribution of the Coulomb interaction to the electronic potential energy is greater than the contribution to the hole energy. This causes a larger variation in the potential felt by the electronic wave packet. The state in the valence band also feels slight variations from the potential due to the Coulomb interaction, but the extent is reduced considerably. This difference arises from the relative population of carriers in the bands. The present model scales the binding energy by the relative population of carriers, which translates into larger energy shifts for the band with the smaller carrier population, and smaller energy shifts for band with the larger carrier population.

4.4 Conclusions

The model presented in this work accounts for the primary effect of the Coulomb interaction, specifically a decrease in the excitation frequency across the bandgap. From the viewpoint of wave packet control in the weak response regime, this effect does not diminish the possibility of controlling the dynamics. For the materials and quantum well dimensions considered here, the maximum binding energy is roughly 10 meV. This value is, of course, important for spectroscopy and static material properties, but is not crucial for the system dynamics since it can be compensated for by changing the detuning. In fact, the optimal pulse parameters with and without the Coulomb potential are nearly identical except for the excitation frequency. The parameter sets in both cases produce approximately the same eigenstate weights and achievement. Differences in the expectation value of position are very minor as can be seen in Figure 4–6. Adding the Coulomb interaction increases the energy splitting between the first and second electronic eigenstates by $\sim$ 2.2 meV. This

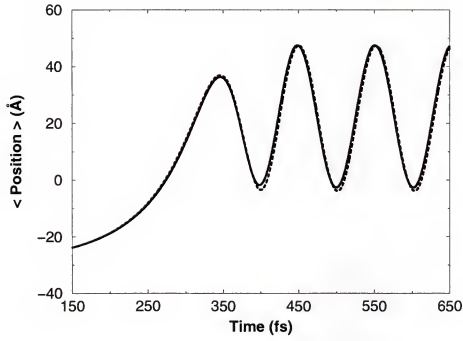

Figure 4–6: Expectation value of position for the electronic wave packet with the Coulomb interaction (dashed line) and without the Coulomb interaction (solid line). The laser parameters are the same in each case, except for the frequency detuning. Adapted from K. L. Shuford and J. L. Krause, J. Appl. Phys. **91**, 6533 (2002).[167]

slight shift decreases the oscillation period of the wave packet by about 5 fs. The Coulomb attraction increases the relative contribution of State $|1\rangle$, which increases the oscillation depth. In general, the differences between the Coulomb and Coulomb-free cases are quite small, and do not change the overall system dynamics dramatically.

One of the reasons for the small effect of the Coulomb interaction in the system studied here is that the average binding energy is $\sim$ 5 meV, which is equivalent to about one quarter of the energy splitting between States $|1\rangle$ and $|2\rangle$. The Coulomb interaction is also an order of magnitude smaller than the splitting between the electronic eigenvalues. As a result, for structures of this composition and dimension, the effects of the Coulomb interaction are much smaller than the energy scales of interest, which minimizes the effects on the dynamics. The binding energy becomes important when its magnitude is comparable to the splittings of the quantum well energies. This is the case for very wide wells, in which the variational wave function

used here is not valid. Coulomb effects might also be important when one state has significant overlap with the initial hole state and the other does not. The Coulomb attraction will then induce a sizeable decrease in the energy of one state, and affect the other only slightly. Splitting between the eigenstates will increase, causing a notable decrease in the oscillation period. However, in both scenarios, the well widths required will minimize the effects of the confining potential, hence eliminating the properties that they are created to produce.

In summary, this chapter investigates a simple, well-studied system to examine the effects of the attractive Coulomb interaction on the dynamics and controllability of electronic wave packets in quantum wells. The results indicate that previous work on this structure, which has neglected the electron-hole Coulomb interaction, is valid qualitatively. Coulomb effects in certain cases can dominate the dynamics, and are crucial when calculating spectroscopic or structural parameters. However, the dynamic effects for structures such as the ones studied here can be overcome by small changes in the detuning parameter.

CHAPTER 5
TERAHERTZ EMISSION

An extensive amount of research over the past decade has been devoted to studies of carrier dynamics in semiconductors with significant attention in quantum-confined systems such as quantum wells, wires, and dots.[169] Semiconductor nanostructures are of considerable interest in the electronics industry due to their minute size, and the ability to customize electronic and optical properties for specific applications. Numerous examples are in common use already such as diodes, rectifiers, transistors, quantum well lasers, modulators, and switches. In this chapter, the possibility that quantum wells can be sources (or detectors) of tunable, controllable Terahertz (THz) radiation is presented. Ultrafast pulses in this frequency regime are difficult to produce currently, and may find applications in spectroscopy, biological imaging, and communications.

When a quantum well structure is excited with a laser pulse of sufficient bandwidth, a coherent superposition state (or wave packet) of electronic levels is created in the conduction band. As the wave packet tunnels back and forth between wells, the oscillating charge density emits radiation. For typical quantum well structures, the emission is in the THz frequency regime. Examples follow that show the frequency and amplitude of this radiation can be controlled by varying the intensity of the dc field, and the characteristics of the excitation pulse. Pairs of pulses can amplify or suppress the density of the wave packet, and hence the magnitude of the THz radiation. This allows control of the frequency and amplitude of the emitted THz signal, and the possibility of optimizing the field to achieve a specific task. As examples, properly tailored THz radiation is used to invert the population in a two-level system, and to excite vibrational states selectively in a diatomic molecule.

5.1 Review of the Perturbative Solution

In this section, a perturbative treatment of charge carrier dynamics in semiconductor heterostructures is reviewed briefly. This method agrees well with experiment, and the more traditional density matrix description of transport in quantum wells.[136] Charge carriers are represented as wave packets that obey the time-dependent Schrödinger equation. Dynamics in two bands, coupled by a dipole moment, are described by the following set of equations

$$i\hbar|\dot{\Psi}_h(t)\rangle = H_h|\Psi_h(t)\rangle - \mu\,\varepsilon\,(t)|\Psi_e(t)\rangle, \tag{5.1}$$

and

$$i\hbar|\dot{\Psi}_e(t)\rangle = H_e|\Psi_e(t)\rangle - \mu\,\varepsilon\,(t)|\Psi_h(t)\rangle, \tag{5.2}$$

where $\varepsilon\,(t)$ is the laser pulse, μ is the transition dipole moment, and $H_{h,e}$ and $\Psi_{h,e}$ are the Hamiltonians and wave functions for the heavy holes (labeled h) and the electrons (labeled e). These equations can be simplified by assuming that the laser intensity is in the perturbative (weak response) regime. In this case, the electronic population scales linearly with the pulse amplitude. As a result, the transition term in Equation (5.1) is negligible with respect to the field-free Hamiltonian. Thus, the heavy hole wave function behaves essentially as an eigenstate, and its probability density is stationary in time. Within this approximation, the equations are uncoupled, and the equation of motion for the electronic wave function can be approximated accurately using time-dependent perturbation theory.

In this work, the Coulomb interactions between the electrons and holes is assumed to have a minimal effect on the dynamics, and are neglected. Previous studies on carrier dynamics have concluded that the Coulomb contribution to carrier dynamics in devices such as those considered here is small,[167] and that the intraband polarization leading to THz emission is influenced only slightly by excitonic effects.[170,171] In the absence of such effects, the electron dynamics can be treated exclusively in the

confined dimension, z. The remaining degrees of freedom contribute only arbitrary, additive constants. The stationary states $|\phi_{j\alpha}\rangle$, for charge carriers confined within the quantum well structure satisfy a one-dimensional, effective-mass Schrödinger equation

$$\left\{ \frac{-\hbar^2}{2\,m_\alpha^*} \frac{d^2}{dz^2} + V_\alpha(z) \pm e\,F\,z \right\} |\,\phi_{j\alpha}\rangle = E_{j\alpha} |\,\phi_{j\alpha}\rangle, \tag{5.3}$$

where $\alpha = h$ or e, m_α^* is the effective mass, V_α is the confining potential, F is a static dc field, and $E_{j\alpha}$ is the energy.[136,145] For electrons, the third term in the Hamiltonian has a positive sign, while for heavy holes this term is negative. The effective masses are assumed to be 0.340 m_0 and 0.0665 m_0 for the heavy holes and electrons, respectively where m_0 is the electron mass.[162,163] The wave packets can be expanded in stationary states as

$$|\Psi_\alpha(t)\rangle = \sum_j |\phi_{j\alpha}\rangle\, e^{-i\,\omega_{j\alpha}\,t}\, a_{j\alpha}(t), \tag{5.4}$$

where $\omega_{j\alpha} = E_{j\alpha}/\hbar$ and $a_{j\alpha}(t)$ are time-dependent coefficients. Inserting this expression into Equation (5.2) gives the expansion coefficients as

$$\dot{a}_{ke}(t) = \frac{i\,\varepsilon\,(t)}{\hbar} \sum_j a_{jh}(t)\, \langle \phi_{ke} |\, \mu \,|\, \phi_{jh} \rangle\, e^{\,i(\omega_{ke} - \omega_{jh})\,t}. \tag{5.5}$$

Next, the usual first-order approximation is made that the amount of population transferred is small. In this case, the coefficients in the summation remain close to their initial values. That is, $a_{1h} \approx 1$ and $a_{jh} \approx 0$ for $j \neq 1$. This gives the electronic wave packet coefficients as

$$a_{ke}(t) = \frac{i\,\mu_{k1}}{\hbar} \int_0^t dt'\, \varepsilon(t')\, e^{\,i\,\omega_{k1}\,t'}, \tag{5.6}$$

where $\mu_{k1} = \langle \phi_{ke} |\, \mu \,|\, \phi_{1h} \rangle$ and $\omega_{k1} = (\omega_{ke} - \omega_{1h})$. The functional form of the laser pulse is chosen as a Gaussian

$$\varepsilon\,(t) = E_0\, e^{-(t-\bar{t})^2/2\Gamma^2} \cos\left[\,\omega\,(t-\bar{t})\,\right], \tag{5.7}$$

where E_0 is the pulse amplitude (arbitrary in perturbative limit), $\bar{t}$ is the center time, Γ is the pulse width, and ω is the carrier frequency. Inserting this expression into Equation (5.6) and making the rotating wave approximation (Appendix B) gives

$$a_{ke}(t) = \frac{i\,\mu_{k1}}{2\hbar} \int_0^t dt'\, E(t') e^{i\omega_{k1} t'}, \tag{5.8}$$

where $E(t)$ is a complex laser pulse defined as

$$E(t) = E_0\, e^{-(t-\bar{t})^2/2\Gamma^2}\, e^{-i\,\omega\,(t-\bar{t})}. \tag{5.9}$$

The final expression for the electronic wave packet is then

$$|\Psi_e(t)\rangle = \frac{i}{2\hbar} \sum_k |\phi_{ke}\rangle\, \mu_{k1} \int_0^t dt' E(t') e^{-i\omega_{ke}(t-t')} e^{-i\omega_{1h} t'}. \tag{5.10}$$

The electronic wave packet has a finite lifetime before dephasing (primarily attributed to carrier-carrier interactions) destroys the coherence of the superposition state. Within the wave function formalism used here, true dephasing cannot be included. As an attempt to model the qualitative features of the observed physical behavior, the wave packet is multiplied by an exponential of the form

$$\psi = \Psi_e(t)\, e^{-\gamma\,(t-\bar{t})}, \tag{5.11}$$

where $\gamma = 0.40\ \mathrm{ps}^{-1}$. This value is consistent with intraband dephasing times extracted from numerical fits for GaAs/AlGaAs superlattices[171] and single quantum wells[172] under similar excitation conditions. The electronic wave packet begins decaying at the peak amplitude of the excitation pulse, and has a lifetime of approximately 8 ps.

The oscillating wave packet creates an intraband polarization (time-dependent dipole moment) given by

$$d\,(t) = \langle \psi \,|\, e\, z \,|\, \psi \rangle. \tag{5.12}$$

The coherent THz signal[10,11,173] produced by this polarization is proportional to the second derivative of the dipole moment

$$E_{\mathrm{THz}} \propto \frac{\partial^2 d(t)}{\partial t^2}. \tag{5.13}$$

The characteristics of this signal can be modified, as demonstrated in the following sections.

5.2 Tunable THz Emission

One way to control the THz emission from quantum wells is to excite with a fixed laser pulse, and vary the dc field. The excitation pulse must have sufficient spectral bandwidth to excite coherently at least two electronic levels in the conduction band simultaneously. The two-state wave packet that is created oscillates between the wells with a frequency $(E_2 - E_1)/h$. The energy splitting of the two electronic levels governs the beat frequency, and changes as a function of the magnitude of the static dc field. The range of frequencies that can be emitted is dictated by the dimensions of the structure, its material properties, and its response to the bias field.

As an example, consider the asymmetric double quantum well (ADQW) in Figure 5–1. This structure has been the focus of numerous experimental and theoretical studies because of its simplicity, the availability of high-quality samples, and the abundance of data concerning its physical properties.[2,6,10,127,128,130,131] The model potential has a 100 Å wide well, and an 80 Å narrow well separated by a 20 Å barrier. The well depths and band gaps are based on parameters for GaAs and AlGaAs.[162,163] Application of a reverse bias dc field brings the two lowest energy levels in the conduction band into a tunneling resonance. These levels undergo an avoided crossing as the field increases from 0 to -40 kV/cm. In the valence band, the heavy hole levels diverge in energy as the field increases, which traps the holes in a single well. The properties of this system are well-known, making it a good candidate for preliminary studies regarding the possibilities of controlling THz emission.

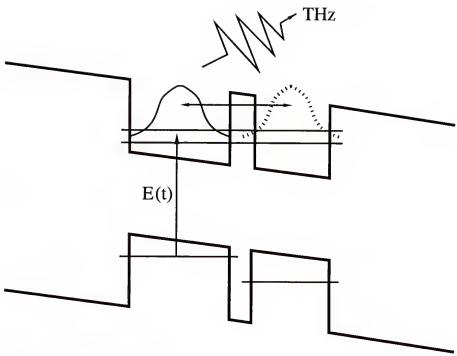

Figure 5–1: Schematic of the asymmetric double quantum well system considered in this work. Excitation occurs across the band gap into the wide well. The electronic wave packet oscillates through the narrow barrier creating an intraband polarization, which is the source of the THz radiation. Adapted from K. L. Shuford and J. L. Krause, J. Phys. Chem. A **106**, 10818 (2002).[174]

As a first example, the ADQW system is excited by a laser pulse with parameters $\bar{t} = 600$ fs, $\Gamma = 150$ fs, and a detuning from the first electronic state of 1.32 THz. Note that the detuning is not the carrier frequency, but the difference between the carrier frequency and the energy of the first electronic state. With these pulse parameters, and for the dc fields considered here, a coherent superposition is created that is composed solely of the lowest two levels in the conduction band. These levels are dipole-coupled via the laser field to the highest energy heavy hole state in the valence band. Figure 5–2 shows the THz signals produced by the oscillating wave packet as a function of the dc field. As the dc field increases to -11 kV/cm, the splitting between the first two electronic levels decreases, which produces a longer oscillation period and deeper oscillations. At dc fields larger than -11 kV/cm, the energy splitting increases, which yields shorter periods and shallower oscillations. At -11 kV/cm

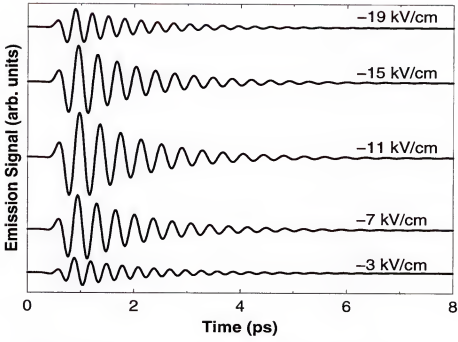

Figure 5–2: THz emission signals as a function of the dc field. Identical excitation pulses are used for each signal. The dc field is varied between −3 and −19 kV/cm. The signal is the most intense when the field is −11 kV/cm. Adapted from K. L. Shuford and J. L. Krause, J. Phys. Chem. A **106**, 10818 (2002).[174]

the system is in a tunneling resonance, with the smallest energy splitting and the deepest oscillations. The wells in the structure are strongly coupled at this point with eigenstates very similar in character and energy, and completely delocalized across the structure. The excitation pulse coherently excites both stationary states with equal weight, and the most intense signal is observed. These results are qualitatively similar to experimental results observed previously.[10,12]

Further information about the effects of the dc field can be gleaned by examining the Fourier transforms of the traces in Figure 5–2. As seen in Figure 5–3, the peak observed with a bias of −11 kV/cm is approximately 30% more intense than those produced at −7 and −15 kV/cm, and approximately six times as intense as the remaining peaks. These figures indicate that at small and moderate magnitudes of the dc field, one eigenstate begins to dominate the coherent superposition, and the intensity of the signal decreases. The emission signals at −3 and −19 kV/cm

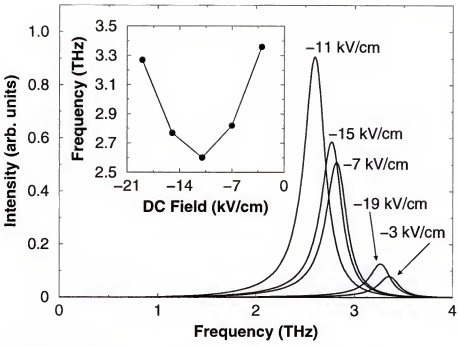

Figure 5–3: Fourier transforms of the emission signals in Figure 5–2. The inset shows the peak frequency in the signals as a function of dc bias field. The peak at −11 kV/cm is at least 30% more intense than the other signals. Adapted from K. L. Shuford and J. L. Krause, J. Phys. Chem. A **106**, 10818 (2002).[174]

are significantly weaker. In the limit that a single stationary state is excited, the amplitude of the THz emission is zero.

As the results above indicate, the ADQW is a simple example of a tunable THz emitter or detector. The structure considered here has an emission range of $\sim$ 2 THz, with varying signal intensities. This frequency range can be increased by clever structure design. Other semiconductor devices have also been shown to provide emission in this frequency regime. Several groups report the capability of various implementations of photoconducting antennas[173,175,176] and superlattices[12] to create bursts of THz radiation corresponding to sub-millimeter wavelengths.

5.3 Signal Interference Effects

The properties of the coherent superposition state that emits the THz emission can be altered to vary the intensity of the emission. Excitation with a pair of phase-locked optical pulses offset by a delay time, τ, enables interferometric enhancement,

annihilation, or shifting of the THz emission. The wave packets produced by each pulse are highly dependent on the relative phase of the excitation pulses. The magnitude of the THz signal is a function of the total wave packet density, and can be amplified or diminished by the interference between the excited waves. The intensity of two interacting waves with a time delay τ can be written as

$$\left|A\cos(\omega t) + A\cos[\omega(t-\tau)]\right|^2 = A^2\Big\{\cos^2(\omega t) + [\cos(\omega t)\cos(\omega\tau) + \sin(\omega t)\sin(\omega\tau)]^2 + 2\cos(\omega t)[\cos(\omega t)\cos(\omega\tau) + \sin(\omega t)\sin(\omega\tau)]\Big\}, \quad (5.14)$$

where for simplicity both wave packets are produced by identical pulses. In this case, the amplitudes (A) and frequencies (ω) in the preceding equation are equal.

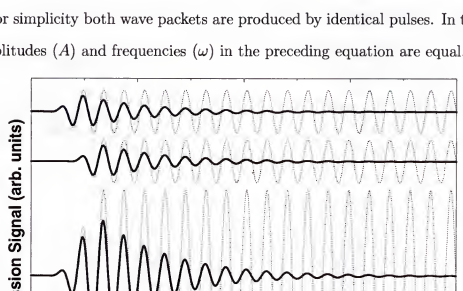

Figure 5–4: Coherent amplification of THz emission signals. The top two curves are the signals resulting from excitation with a single pulse. The bottom curve is the signal produced when both pulses are applied with a phase difference of 2π. The signal is amplified by a factor of four, indicating complete constructive interference. In all signals, the solid lines include dephasing, while the dotted lines do not. Adapted from K. L. Shuford and J. L. Krause, J. Phys. Chem. A **106**, 10818 (2002).[174]

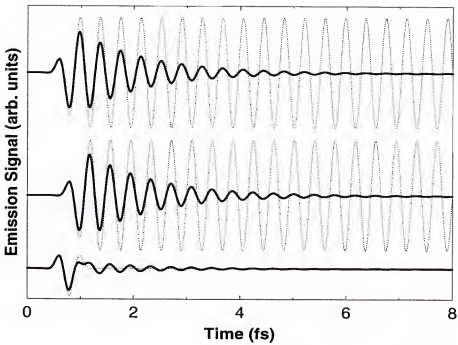

Figure 5–5: Coherent destruction of THz emission signals. The top two curves are the signals resulting from excitation with a single pulse. The bottom curve is the signal produced when both pulses are applied with a phase difference of π. The signal is annihilated, indicating complete destructive interference. In all signals, the solid lines include dephasing, while the dotted lines do not. Adapted from K. L. Shuford and J. L. Krause, J. Phys. Chem. A, **106**, 10818 (2002).[174]

For the two-state wave packets considered previously in the ADQW, ω is the beat frequency, $(E_2 - E_1)/\hbar$. As can be seen in Equation (5.14), the intensity of the wave depends sensitively on the delay time, τ. For the two waves to interfere constructively, the delay time between excitation pulses must equal the oscillation period (or a multiple of the period). For example, setting $\tau = 2\pi/\omega$ in Equation (5.14) yields an amplitude that is four times as intense as the signal from a single pulse. Destructive interference is also possible by adjusting the delay time to equal half of the oscillation period. Inserting $\tau = \pi/\omega$ into Equation (5.14) predicts complete annihilation of the THz signal. As shown in Figures 5–4 and 5–5, this simple analysis is adequate to describe the observed interference phenomena. In these figures, the relative phase between the wave packets has been adjusted to 2π and π, respectively by varying the delay time. In both plots the solid lines include dephasing (with $\gamma = 0.40$ ps^{-1}), while

the dotted lines ignore this effect ($\gamma = 0$). When dephasing is included, the decay of the signal obscures the full extent of the interference. However, the dotted lines clearly demonstrate the expected amplification by a factor of four for constructive interference, and the complete cancellation of the signal for destructive interference. These results are in qualitative agreement with experiments demonstrating controlled THz emission.[127,128]

The simplified analysis does not describe the interference phenomena completely when the relative phase between the pulses is not an integer of π. When $\tau = 1.5\pi/\omega$, for example, the intensity expected from Equation (5.14) is

$$A^2\left\{\cos^2(\omega\, t) + \sin^2(\omega\, t) - 2\cos(\omega\, t)\sin(\omega\, t)\right\} = A^2\left\{1 - \sin(2\,\omega\, t)\right\}. \tag{5.15}$$

The intensity produced by a single pulse can be written as

$$A^2\cos^2(\omega\, t) = \frac{A^2}{2}\left[1 + \cos(2\,\omega\, t)\right], \tag{5.16}$$

indicating that THz signal with $\tau = 1.5\pi/\omega$ should be approximately twice as intense as that produced with a single pulse. However, this behavior is not observed, as shown in Figure 5–6. In fact, the signal is approximately three times as intense as the single pulse case. A pseudo-vector approach has been used previously to interpret signal intensities for cases of fractional π relative phases.[128,129] Note also in Figure 5–6 that the fractional phase difference induces a slight phase shift in the amplified signal compared to the first excitation pulse. In this case, the second pulse shifts the emission signal to about 50 fs earlier. This can be justified by writing Equation (5.15) as

$$A^2\left[1 + \cos\left(2\,\omega\, t + \frac{\pi}{2}\right)\right], \tag{5.17}$$

indicating a phase shift of $\pi/2$. Our results display small phase shifts in all cases studied with fractional relative phases between the pulses. Under similar conditions,

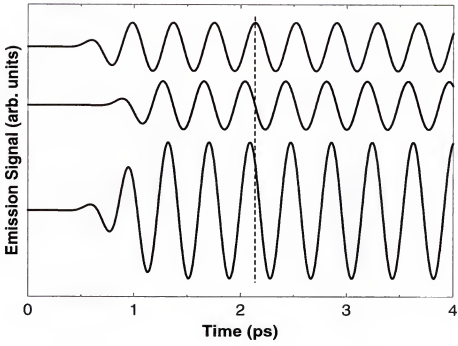

Figure 5–6: Coherent amplification of THz emission signals. The top two curves are the signals resulting from excitation with a single pulse. The bottom curve is the signal produced when both pulses are applied with a phase difference of $3\pi/2$. The amplitude of the signal is enhanced by roughly a factor of three. A phase shift of 50 fs compared to the top signal is observed. Dephasing is neglected in this figure. The dashed line is included to aid visualization. Adapted from K. L. Shuford and J. L. Krause, J. Phys. Chem. A **106**, 10818 (2002).[174]

phase shifts as large as 330 fs have been observed experimentally.[127–129] Other experiments have demonstrated that pulse shaping and multiple pulses in series can amplify the THz signal significantly.[128–130] These results are intriguing illustrations of the use of pulse sequences with well-defined phase relations to amplify, destroy, or shift the THz emission from semiconductor heterostructures.

5.4 Applications for THz Emission

In this section, the possibility that a carefully chosen excitation pulse can produce THz emission displaying desired characteristics is investigated. As demonstrated above, the frequency and amplitude of the signal can be tuned by adjusting the bias field and the center frequency of the excitation pulse. In principle, the phase and amplitude of the excitation pulse can be optimized as well.[177–179] The optimized field

can then be applied to a system of interest, and re-optimized if necessary to improve the performance in the actual physical system.[75]

As an example, population control in a two-level system is considered (Appendix B). The goal is to transfer population completely from one state to another using optimized THz emission as the excitation source. The two-level system is a generic case that might, for example, represent population transfer between rotational levels in molecules, or Rydberg states in atoms. The solution to the problem of population inversion in two-level systems is well known. With resonant excitation, complete population inversion[90,180] is achieved if the area of the pulse is an odd multiple of π. The inversion is robust with respect to the pulse shape, but not with respect to the area. Pulse area is defined as

$$\int_0^t dt' \, \Omega_{21} = \int_0^t dt' \, \frac{\langle 2| \, \mu \, |1\rangle}{\hbar} \, E(t'), \tag{5.18}$$

where Ω_{21} is the Rabi frequency, $\langle 2| \, \mu \, |1\rangle$ is the transition dipole matrix element, and $E(t)$ is the laser pulse envelope.

A two-level system with a resonant excitation frequency of 4 THz is used. To produce the required radiation, the ADQW in Figure 5–1 is biased with a dc field of -23.1 kV/cm. An optimized THz signal is produced by adjusting the center frequency of the excitation pulse to yield a THz pulse with area π. Figure 5–7 shows the optimized THz radiation and a population analysis of the test system. The excitation field induces complete population transfer from State $|1\rangle$ to $|2\rangle$, thus achieving the control objective. At the completion of the excitation pulse, all of the population has been transferred to the upper state. The unusual shape of the THz signal does not affect the efficiency of the population transfer, as expected. The population inversion illustrated in Figure 5–7 is quite robust with respect to small changes in the pulse area. Slight deviations from π do not significantly decrease the performance. Some of the expected deviations caused, for example, by fluctuations

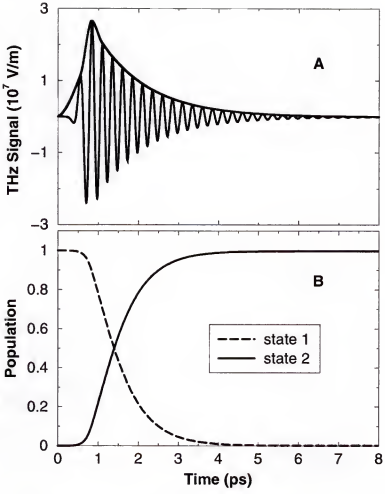

Figure 5–7: Sculpting of THz emission to invert population in a two-level system. A) Optimized THz radiation; B) Population dynamics of the two-level system. The THz field has a pulse area of π that completely inverts the population. Adapted from K. L. Shuford and J. L. Krause, J. Phys. Chem. A **106**, 10818 (2002).[174]

in the polarization lifetime, can be alleviated by adjusting the center frequency of the excitation laser.

Another possible application for THz pulses is spectroscopy in the linear regime. The population is not inverted completely, but significant control over the relative population of excited states is attainable. As an example, consider vibrational state selectivity in a simple molecule. A Morse potential is used to model the potential

energy of a diatomic molecule. The functional form of a Morse potential is

$$V(r) = D_e \left[1 - e^{-\beta(r-r_e)}\right]^2, \tag{5.19}$$

where D_e is the dissociation energy, r_e is the equilibrium bond distance, and β is a constant related to the vibrational frequency. In the example presented here, $D_e = 500$ kJ/mol, $r_e = 2.75$ Å, and $\beta = 0.67$ Å^{-1}. Using a reduced mass of 20 atomic mass units, the fundamental vibrational frequency is 250 cm^{-1}. The fourth overtone has a frequency of 4.95 ω_e demonstrating the characteristic effects of anharmonicity. The dipole moment is a function of distance, and is assumed to be

$$\mu(r) = e^{0.5}\,(r/r_e)\,e^{-0.5\,(r/r_e)^2}. \tag{5.20}$$

This function rises rapidly from 0 at the origin to 1 at the equilibrium bond distance, and decreases slowly as the potential becomes more anharmonic. The parameters chosen for the potential and dipole moment are typical for light diatomic molecules. They can be varied easily to model a desired molecule for a specific application.

A modified quantum well structure has been designed to produce the vibrational frequencies near the bottom of the potential. Figure 5–8 shows a schematic of a notched, six-well structure. Each well is 65 Å wide, and the barriers are 20 Å wide. The unusual shape of the quantum well structure produces eigenvalues with a non-trivial response to the dc field. In the absence of a dc field, States 1–3 and States 4–6 are close in energy, while a larger energy gap exists between States 3 and 4. The states begin to converge in energy as the magnitude of the dc field is increased, with States 3 and 4 interacting first at −35 kV/cm. A large range of frequencies can be produced, which in turn, can create exotic THz profiles. With the correct laser pulse, it is possible to excite just States 3 and 4 yielding a single-frequency signal. This signal can be tuned to match several vibrational states in the diatomic. Alternatively,

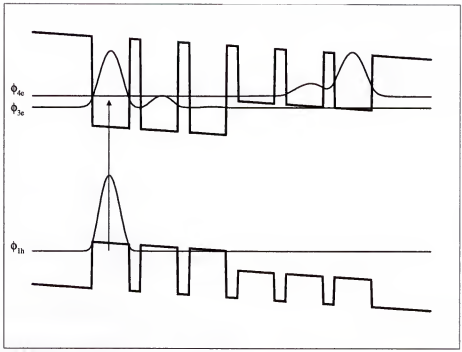

Figure 5–8: Schematic of the notched six-well structure with an applied bias field of −20 kV/cm. Electronic States 3 and 4 are shown, as well as the lowest hole state. This structure has been designed to produce emission corresponding to the energies of several vibrational states of a diatomic molecule. Adapted from K. L. Shuford and J. L. Krause, J. Phys. Chem. A **106**, 10818 (2002).[174]

signals containing multiple frequencies can be produced that excite a distribution of vibrational levels.

The vibrational state distributions excited by the THz signals are highly dependent on the dc field used to bias the quantum well system, and the laser pulse that excites it. Table 5–1 shows the vibrational populations produced by excitation with various THz fields. Using the correct combination of dc field and laser parameters yields THz signals resonant with the transition from the ground state to several vibrational levels in the diatomic. As can be seen in the table, essentially complete transfer of the excited population to $\nu = 1$, 2, or 3 is possible with the correct parameter set. The procedure is most successful at populating the $\nu = 2$ state due to the large dipole matrix element coupling this state to the ground state. The population of $\nu = 2$ as a function of time rises rapidly to one , while other vibrational states

Table 5–1: Population Control of Vibrational States in a Diatomic Molecule[a]

DC	ω	Γ	Signal	P_1	P_2	P_3	P_4
−28	18.6	95	250	0.98	0.02	10^{-5}	10^{-7}
−20	18.4	85	498	10^{-6}	1.0	10^{-6}	10^{-9}
−12	19.1	75	744	10^{-4}	0.067	0.93	10^{-6}
−3	20.8	65	995	10^{-3}	0.47	0.014	0.52
−28	29.7	35	214, 683	0.19	0.80	0.01	10^{-6}
−20	19.7	35	163, 674, 841	0.78	0.13	0.09	10^{-6}
−12	19.7	35	120, 879, 1007	0.06	0.85	0.09	10^{-4}
−3	23.0	35	996, 1090, 1071, 1199	7.5×10^{-3}	0.66	9.4×10^{-3}	0.32

[a] The left side of the table shows the excitation parameters for the quantum well shown in Figure 5–8. The units for the dc field, frequency detuning, and pulse width are kV/cm, THz, and fs, respectively. The middle section shows the dominant frequencies present in the Fourier transform of the induced signal in units of cm^{-1}. The right side displays the relative populations of the vibrational states in the diatomic molecule following excitation with the THz signal. The subscript labels the vibrational quantum number. Adapted from K. L. Shuford and J. L. Krause, J. Phys. Chem. A **106**, 10818 (2002).[174]

are not populated significantly at any time. Populating levels $\nu = 1$ or 3 (with the appropriate parameter set) gives final-time populations of 0.98 and 0.93 respectively. The intermediate time dynamics is considerably different than in the $\nu = 2$ example. In both of these cases, the population of $\nu = 2$ increases rapidly and begins to oscillate at early times. As the THz pulse ends, $\nu = 2$ decays, and the target state is populated. This impulsive excitation of $\nu = 2$ is found in all of the single-frequency studies.

As can be seen in Table 5–1, the lowest three excited vibrational states can be populated with high selectivity. However, due to the anharmonicity in the potential and the dipole moment, the same quantum well structure cannot be used to produce THz fields that excite higher lying states. Populating $\nu = 4$, for example, is not nearly as efficient as $\nu = 1{-}3$. Creating a THz signal with the resonant frequency does not induce the same selectivity as observed in the excitation of lower vibrational levels. This is due to several effects. The bandwidth of the THz signal overlaps more than one state as the energy levels become closer together. The dipole matrix element

is also two orders of magnitude smaller than for the $\nu = 2$ state. As a result, the population is essentially shared between $\nu = 2$ and 4, as can be seen in Table 5–1. The impulsive excitation of $\nu = 2$ is dominant in this case, producing a superposition state that cannot be coerced into a single vibrational level. Vibrational states greater than $\nu = 5$ cannot be populated with the current six-well structure. However, it is likely that, as in $\nu = 4$, performance would diminish due to the weak coupling to the initial state as ν increases.

Several trends are observed in the laser pulses used to excite the quantum well structure generating the optimized THz signal (upper left portion of Table 5–1). The frequencies and the widths used for the excitation pulse yield the most intense, single-frequency THz signal. The clearest trend is the decrease of bandwidth (increased Γ) as the magnitude of the dc fields increase. The bias field causes the energy levels to converge. To excite just two electronic levels (one frequency in signal) the bandwidth must decrease. A slight increase in laser frequency is also generally observed as the magnitude of the field decreases. It is difficult to interpret the frequency shifts, because the component eigenstates of the wave packet also vary as a function of dc field.

Exciting the diatomic molecule with a THz signal composed of multiple frequencies produces population in several vibrational states. The lower portion of Table 5–1 contains population data from THz signals in which more than one frequency is present. With the dc field set to -28, -20, or -12 kV/cm, the population is distributed among three vibrational levels. Further, in each case the majority of population is in a state that is not significantly populated by single frequency THz pulses at the same dc field. Figure 5–9 shows the THz signal from the final entry in Table 5–1. It is evident from the time and frequency domain representations that the signal is composed of several frequencies. This particular wave form produces a distribution of vibrational states in which the populations alternate in magnitude. Most of the

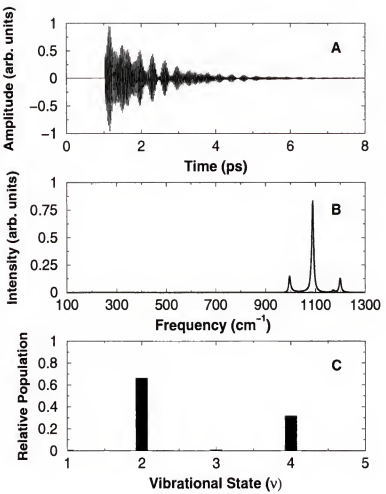

Figure 5–9: Complex THz signal emitted from the six-well structure in Figure 5–8 with a bias field of -3 kV/cm. A) Signal in the time domain; B) Power spectrum of the signal; C) Relative populations excited in the diatomic molecule. Adapted from K. L. Shuford and J. L. Krause, J. Phys. Chem. A **106**, 10818 (2002).[174]

frequencies present appear to be in the region resonant with $\nu = 4$ or 5, however the majority of the population occupies the $\nu = 2$ state. This example demonstrates once again the importance of the dipole matrix element. Even with intense peaks resonant with higher lying vibrational levels, the population prefers to occupy a state strongly coupled to the ground state.

This work shows that with a small number of parameters, the population of vibrational energy levels in a diatomic molecule can be shifted from a single state to many states using optimized THz pulses. The final result depends entirely on the

qualities of the THz signal, which can be sculpted to obtain a desired control objective. The notched six-well system is a versatile structure that can produce a wide variety of THz signals with numerous frequencies. This is a clear example demonstrating the utility of band gap engineering. The six-well structure has been designed specifically for the task of producing THz signals to excite the diatomic molecule used in this study.

Population inversion in a two-level system and state selective excitation are only two possible applications of THz radiation. Historically, the low power of existing sources has limited most applications to linear, time-domain spectroscopy, imaging, and communication.[181–183] However, in recent years several groups have reported the ability to shape and enhance narrow-band THz radiation.[182,184–186] The increased power and short duration of new THz sources have enabled applications in non-linear optics and multiphoton spectroscopy.[185] As further progress is made in pulse enhancement and shaping, semiconductor structures may realize their potential as versatile sources of tunable electric fields in the far IR wave-length regime.

5.5 Conclusions

This work demonstrates that control of THz radiation emitted from quantum wells can be achieved using simple, experimentally feasible laser pulses and laboratory conditions. The frequency of the emission is tunable over a large range by varying the magnitude of the static dc field. The amplitude of the emission can be altered by tuning the excitation frequency. Pairs of pulses can amplify or suppress the signal intensity. Phase-locked pulses with the proper delay times yield signals up to four times as intense as the signal produced with a single pulse. Alternatively, the signal can be completely annihilated. Phase shifts in the THz signal can be produced by setting the relative phase between the excitation pulses to a non-integer multiple of π. Also, THz signals with desired characteristics can be produced by varying the

excitation conditions. The emission signal can be optimized to achieve a predetermined goal in a system of interest, such as population transfer in a two-level system or state selective excitation in a diatomic molecules. A carefully constructed THz field can invert the population in a two-level system, and can actively control the relative population of several vibrational states in a model diatomic molecule.

Many other applications of sculpted THz radiation are feasible. This work is a first step toward analyzing what might be possible. Future work will consider additional examples of potential technological significance. Such applications will likely become more experimentally accessible as further advances are made in increasing the power of the sources, and developing efficient means to shape THz pulses.

CHAPTER 6
ADIABATIC PASSAGE

When a system is perturbed by an external potential, the magnitude of the induced change depends sensitively on the size and interaction time of the perturbation. A perturbation that occurs infinitely fast leaves the initial state unaltered. In contrast, if the perturbing potential varies slowly enough, an initial state can be transformed to a final state smoothly and continuously. In this case, the exact solutions of Schrödinger's equation are reproduced accurately by solving the time-independent problem using the instantaneous value of the Hamiltonian at each time step. When this is true, the state evolution is termed adiabatic. For textbook discussions on this subject see the work of Messiah,[31] Bohm,[89] and Allen and Eberly.[90]

Adiabatic passage has been documented extensively in the literature for atomic and molecular systems. Implementations of rapid adiabatic passage have achieved population inversion in two and many-level systems.[92,96] Frequency modulation (such as pulse chirping) can be used to achieve adiabaticity. Intense, chirped laser pulses have been shown to yield robust, state-selective excitation. Appropriately chirped pulses can produce efficient population transfer, while avoiding molecular dissociation.[98,99,101,187] One implementation of adiabatic passage is known as STIRAP (stimulated Raman adiabatic passage).[87] STIRAP uses a counter-intuitive pulse sequence (probe before pump) to drive population from an initial state to a final state that is not dipole-coupled to the initial state. This method produces complete population transfer in many-level systems with transform limited pulses[87,88,93] and chirped pulses.[102,104] The criterion for adiabatic passage is satisfied by varying the intensities of the pump and probe pulses, the timing between the pulses, and their detuning from resonance. A related method, known as APLIP (adiabatic passage by light induced

potentials),[105–107,188] uses the same counter-intuitive pulse sequence as STIRAP, but the intermediate dynamics are notably different. In APLIP, the laser pulses are intense enough to deform the potential energy surfaces, which allows a wave packet to travel continuously along a chosen path to the final state. A technique using time-gating of pulses has also proven successful at selective population transfer.[189,190]

Applications of rapid adiabatic passage to control population transfer in the solid state are not as numerous as those in the gas phase. Issues such as more rapid relaxation times, and the abundance of interacting states have hindered the development of adiabatic passage in this medium. Methods similar to STIRAP have been used to transfer population in quantum wells with some success.[139,191] Quantum dots are emerging as promising systems for applications of population control, due to the sharp, atomic-like states that inhabit such reduced-dimensionality systems. Recently, STIRAP has been proposed to control population in a double-dot structure.[25,142] Controlling the electronic properties of mesoscopic systems is of great interest for possible applications in optoelectronic devices and quantum information processing. In addition, reduced-dimensionality systems can be customized to exhibit desired characteristics, making them attractive targets for applications of quantum control.

In this chapter, the possibility of adiabatic passage in a double quantum well via the application of a controlled dc field is investigated. Previously discussed methods use pulse sequences, or chirped laser pulses to achieve adiabatic passage. This proposal suggests a slightly different method. The idea is to use a slowly-varying dc field to perturb the system adiabatically, and shift the population to a desired target state. The dc field alters the potential experienced by electrons in the conduction band during the carrier lifetime, and creates a time-varying state whose properties

can be specified. In principle, this method provides a smooth, reversible pathway between quantum wells, which can be used to control electron density in semiconductor heterostructures.

6.1 Methodology

The basic theoretical approach used in this work has been described previously.[136,152,167] The method captures the major contributions of the electronic dynamics in a quantum well (QW) structure. The particle density is assumed to be low, which yields long excited-state lifetimes, and minimizes carrier-carrier interactions that lead to relaxation and dephasing. Coulomb interactions are neglected. This decouples the problem into one confined dimension, and two unconfined (irrelevant) dimensions. Previous work has shown the primary effect of the electron-hole interaction is to decrease the band gap, which has a minimal impact on electron dynamics and controllability.[167]

The evolution of the electronic state is described by the Schrödinger equation,

$$i\hbar\dot{\Psi}(t) = H(t)\Psi(t), \tag{6.1}$$

where the QW Hamiltonian is

$$H(t) = \frac{-\hbar^2}{2\,m^*}\frac{d^2}{dz^2} + V(z) + e\,F(t)\,z. \tag{6.2}$$

In this equation m^* is the effective mass[162,163] of a carrier in the conduction band of GaAs ($m^* = 0.0665\ m_e$), $V(z)$ is the QW potential, and $F(t)$ is the dc field. The dc bias field modifies the electronic potential at each instant of time, thereby altering the instantaneous eigenvalues and eigenvectors of the Hamiltonian. In this application, the wave function is propagated using a split-operator method (Appendix C). The initial state is chosen as the lowest electronic eigenstate in the conduction band, in the absence of the dc field. The mechanism by which this state is populated is not included in this work. It might, for example, be populated via photoexcitation with

a low intensity laser pulse with spectral bandwidth smaller than the characteristic energy levels of the QW structure.

6.2 Theoretical Considerations

Before presenting the numerical results, it is instructive to obtain an expression describing the eigenstate composition of the wave function during the perturbation. This exercise determines conditions that are most favorable for efficient adiabatic passage, and predicts when the adiabatic approximation is valid. The validity of the adiabatic approximation can be estimated by calculating the probability that the system occupies a state other than the initial state throughout the passage. An analytic expression for the state population under these conditions can be obtained by making several approximations, which may or may not be accurate or justified for a given system. However, it is possible to obtain an expression for the time dependence of the components of the wave function in a more rigorous manner. From this, the optimal conditions for adiabatic passage can be deduced.

The electronic wave function is expanded as

$$\Psi(t) = \sum_j c_j\,(t)\,|\,\phi_j\,(t)\rangle\, e^{-(i/\hbar)\int_0^t E_j(t')dt'}, \tag{6.3}$$

where $|\,\phi_j\,(t)\rangle$ and $E_j(t)$ are the instantaneous values of the eigenvectors and eigenvalues at time t. Note that, due to the time-varying dc field, these quantities differ at each time step. Inserting this equation into Equation (6.1), multiplying by $\phi_k^\star \exp[(i/\hbar)\int_0^t E_k\,dt']$, and integrating over all space yields

$$\dot{c}_k + \sum_j c_j\,\langle\phi_k|\,\dot{\phi}_j\rangle\, e^{-(i/\hbar)\int_0^t (E_j - E_k)\,dt'} = 0. \tag{6.4}$$

Using the time-independent Schrödinger equation, and the Hermitian properties of the Hamiltonian gives

$$\langle\phi_k|\,\dot{\phi}_j\rangle = \frac{\langle\phi_k|\,\dot{H}\,|\,\phi_j\rangle - \dot{E}_j\,\delta_{kj}}{(E_j - E_k)}. \tag{6.5}$$

Note that the time variation of the energy associated with state j is

$$\dot{E}_j = \langle \phi_j | \dot{H} | \phi_j \rangle. \tag{6.6}$$

Equation (6.4) can then be rewritten as

$$\dot{c}_k + \sum_{j \neq k} c_j \frac{\langle \phi_k | \dot{H} | \phi_j \rangle}{(E_j - E_k)} \exp\left[-\frac{i}{\hbar} \int_0^t (E_j - E_k)\, dt' \right]. \tag{6.7}$$

By assumption, the initial values of the wave function coefficients are $c_1 = 1$ and $c_{k \neq 1} = 0$. If the values of these coefficients do not change significantly during the propagation, the process is adiabatic, even though the states themselves are changing due to the effects of the perturbation. For the Hamiltonian in Equation (6.2), the time variation of first component is

$$\dot{c}_1 = -\sum_{j \neq 1} c_j \frac{\langle \phi_1 | ez | \phi_j \rangle}{(E_j - E_1)} \dot{F} \exp\left[-\frac{i}{\hbar} \int_0^t (E_j - E_1)\, dt' \right]. \tag{6.8}$$

As can be seen in this equation, the time evolution of c_1 depends on the other coefficients, the overlap and energy splitting with surrounding states, as well as the time variation of the dc field at each time step. The weights can remain essentially constant, and close to the initial values if the time variation of F compliments the other factors. For example, if the energy difference is large, the overlap will likely be small, and the time variation of the field can be sizeable and still not cause a significant change in wave function composition. Achieving this delicate balance throughout the passage leaves the system in the slowly varying, initially occupied state, while the remaining states make minimal contributions. This implies that the electronic wave function remains essentially a pure state, and evolves adiabatically under the effect of the perturbation. The balancing act must occur during the entire dynamical process. As a result, regions in which ΔE is small (large overlap), and the time variation of F

is large are the most stringent tests of adiabaticity. In general, systems with large energy splittings are the most efficient at navigating the adiabatic passage successfully, and allow the quickest interaction time of the perturbation.

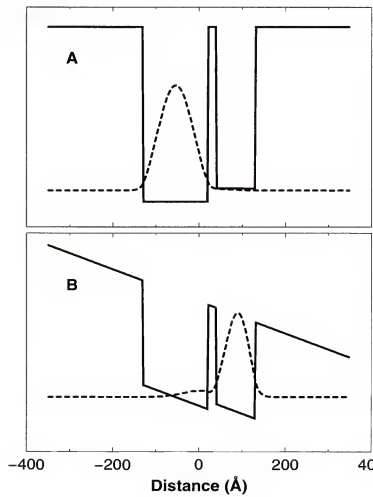

Figure 6–1: Notched asymmetric double quantum well and the probability density of the lowest electronic eigenstate. A) Potential in the absence of the dc field; B) Potential profile when a −40 kV/cm dc bias field is applied. The goal is to apply a dc field that causes the system to evolve adiabatically from the configuration in Panel A to that in Panel B. Adapted from K. L. Shuford and J. L. Krause, J. Phys. D **36**, 439 (2003).[192]

6.3 Passage Between Quantum Wells

In this section, the results of the procedure described above for an asymmetric double quantum well (ADQW) structure are presented. The ADQW system has been thoroughly studied, both theoretically and experimentally, and its dynamics are

well understood.[2,6,10,127,128,130,131] In the structure considered here, a 20 Å barrier separates a 150 Å wide well and a 90 Å narrow well. The wide well has a depth of 0.26 eV, while the the narrow well has a depth of 0.24 eV (Figure 6–1). This scenario corresponds roughly to a $GaAs/Al_xGa_{1-x}As$ heterostructure[162,163] with $x = 0.348$ in regions forming the energy barriers, $x = 0$ in the wide well (GaAs layer), and $x = 0.0235$ in the narrow well. A 60/40 band offset is assumed.

The double-well energy spectrum consists of a series of two-state minibands. Only the lowest miniband is addressed in this work because of the sizeable energy separation between it and the higher-lying states. In the absence of a bias field, the 20 meV energy offset in the well depths localizes the density of the lowest electronic eigenstate completely in the wide well (−130 to 20 Å), as seen in Figure 6–1A. However, a dc field of −40 kV/cm places the state in the narrow well (40 to 130 Å) as shown in Figure 6–1B.

The bias field inverts the energy spectrum of the miniband as seen in Figure 6–2. Initially, the lowest state is localized in the wide well, and separated in energy from the second state by 38 meV. When the field magnitude increases to −30 kV/cm, both states are delocalized across the entire structure, and separated in energy by 10 meV. At a field of −40 kV/cm the lowest state is localized in the narrow well and energetically separated by 15 meV from the nearest state. Knowledge of the response of the double-well system to the dc field provides an opportunity to spatially control the electron density within the QW structure, and to predict the region in which adiabaticity is most difficult to achieve. In this structure, fields between −20 kV/cm to −40 kV/cm require the slowest rate of change because of the significant overlap of the eigenstates, and the small energy separations.

For the system illustrated in Figure 6–1, the goal is to apply a dc field that causes the electronic population to flow from the wide well to the narrow well in a smooth, continuous fashion. To avoid dephasing, this process should occur as quickly

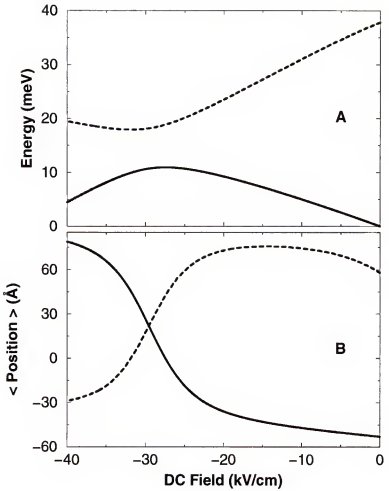

Figure 6–2: Energy and average position of State 1 (solid line) and State 2 (dashed line) as a function of dc field. A) Energy; B) Average position. As the field magnitude increases, State 1 moves from the wide well to the narrow well. Adapted from K. L. Shuford and J. L. Krause, J. Phys. D **36**, 439 (2003).[192]

as possible. As a first attempt, a field that varies linearly from 0 to −40 kV/cm is selected using several different induction times. The induction time is defined as the time required for the field magnitude to increase from zero to its maximum value. Figure 6–3 shows the average position of the state created with induction times of 250 fs (open circles), 2 ps (dashed line), and 5.5 ps (solid line). The state dynamics differ strikingly in each case. As the induction time decreases, the performance diminishes dramatically. For the shorter induction times, a coherent superposition state (wave packet) is created, composed of the first and second eigenstates. The

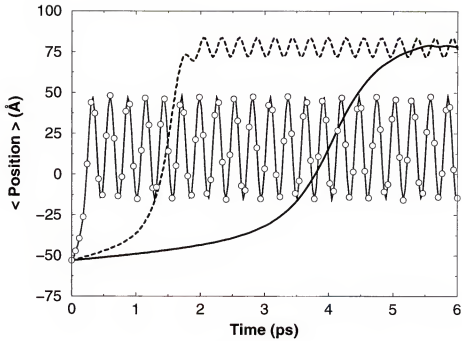

Figure 6–3: Average position as a function time. The field increases from zero to −40 kV/cm linearly over 250 fs (open circles), 2 ps (dashed line), and 5.5 ps (solid line). The oscillations are an indication that the state is not pure, and that a wave packet is created. Inducing the field over 5.5 ps allows the initial state to proceed adiabatically from the wide well to the narrow well. Adapted from K. L. Shuford and J. L. Krause, J. Phys. D **36**, 439 (2003).[192]

deep oscillations observed for the 250 fs case indicate that the eigenstate components have approximately equal weights. A longer induction time produces much shallower oscillations, which indicates that a single component dominates the wave packet composition. With an induction time of 5.5 ps, no oscillations are present indicating that a wave packet is not produced, and the transfer has indeed proceeded adiabatically.

Examining the population of the instantaneous eigenstates as a function of time further supports the interpretation discussed above. Initially, the system is in the lowest eigenstate (population = 1), and all other states are unoccupied. If the propagation occurs adiabatically, the initial state has essentially unit population throughout the process, while all other states have negligible populations. Figure 6–4 shows the state populations as the field is induced over 250 fs and 2 ps. The fast induction time

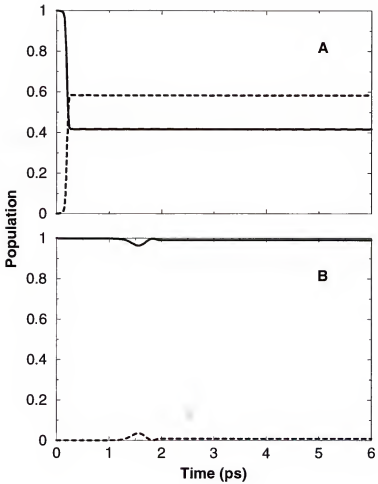

Figure 6–4: Instantaneous population of State 1 (solid line) and State 2 (dashed line) with different induction times. A) Field is induced over 250 fs; B) Field is induced over 2.2 ps. With an induction time of 5.5 ps (not shown), all of the population remains in the initially occupied state. Adapted from K. L. Shuford and J. L. Krause, J. Phys. D **36**, 439 (2003).[192]

of 250 fs mixes the states significantly, as shown in Panel A. Following the induction, a wave packet is created with populations of 0.42 and 0.58 for States 1 and 2, respectively. Increasing the induction time to 2 ps reduces the mixing, but does not eliminate it completely. Panel B shows a small population of State 2 is present after the field has reached its maximum value. The state mixing produces the oscillations noted in Figure 6–3. An induction time of 5.5 ps yields no significant mixing, and no oscillations are observed. The state dynamics for this case are displayed as Figure 6–5. The gradual increase in the field drives the probability density from its initial

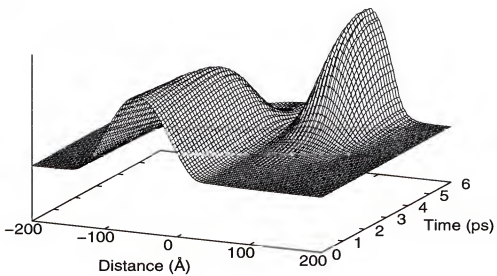

Figure 6–5: Probability density as a function of time. A linear field induced over 5.5 ps drives the initial state localized in the wide well (−130 to 20 Å) to the final state residing in the narrow well (40 to 130 Å). Adapted from K. L. Shuford and J. L. Krause, J. Phys. D **36**, 439 (2003).[192]

position in the wide well, to the final position in the narrow well. The motion is smooth and continuous, progressing adiabatically throughout the entire evolution. The results indicate, as expected, that the longest induction time is best suited for the most successful adiabatic passage.

The effects of more complex dc fields are investigated in an attempt to maximize performance. In principle, the response of the system to the perturbation implies the structure of an optimal field profile that compensates for the energy splitting exactly. The optimal form of the dc field accounts for the energy splittings (and other factors) at each instant in time, and induces variations in the Hamiltonian accordingly. Intuitively, a shaped dc field should be superior to a linearly ramped field. A shaped field would allow for rapid changes in the field when the energy levels

are far apart, and slow variations through regions in which the energy levels are close together.

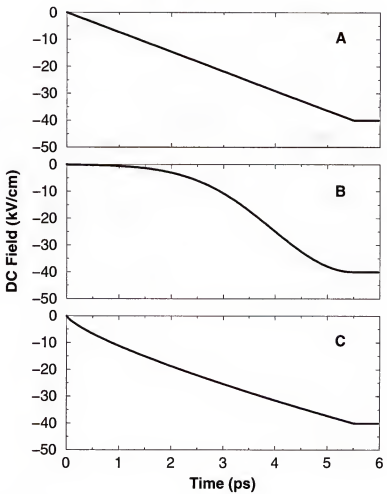

Figure 6–6: Various dc field profiles as a function of time. A) Linear field; B) Non-linear field; C) Non-linear field. All of the fields start at zero and reach −40 kV/cm at 5.5 ps. Each field profile has been tested for its efficiency at transferring population from the wide well to the narrow well in the allotted induction time. Adapted from K. L. Shuford and J. L. Krause, J. Phys. D **36**, 439 (2003).[192]

Figure 6–6 shows three different field profiles. Panel A is the linear field used previously. Panels B and C each have some nonlinear character. All field profiles begin at zero and rise to −40 kV/cm over 5.5 ps. The sensitive range of the dc field for the structure is between −20 and −40 kV/cm as can be seen in Figure 6–2. The field displayed in Panel B proceeds through this region quickly, and as a result

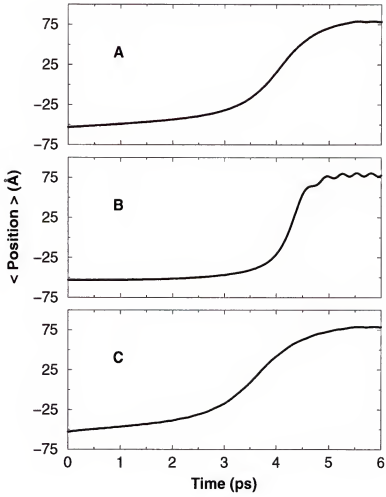

Figure 6–7: Expectation value of position as a function of time. Oscillations are an indication of less efficient adiabatic passage. Each panel shows the average position of the states created by the corresponding dc fields in Figure 6–6. Adapted from K. L. Shuford and J. L. Krause, J. Phys. D **36**, 439 (2003).[192]

one would expect worse performance. This is indeed the case. Each of the three fields is fairly successful at navigating the passage from the wide well to the narrow well. However, the fields in Panels A and C perform better. They both move slowly through the sensitive regions, producing a smooth passage as shown in Figure 6–7. Oscillations are prevalent in Panel B, indicating a decrease in performance due to a slight mixing of states. In Panels A and C, the oscillations are suppressed. Only the lowest two states are populated during this process. The population of State 2 at the final time is another indication of performance. The smaller the population, the

better the performance. For Panels A–C, the populations of State 2 at the final time are 2.5×10^{-5}, 1.1×10^{-3}, and 4.2×10^{-6}, respectively.

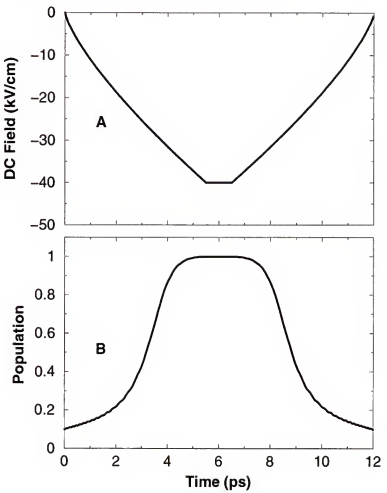

Figure 6–8: Field profile and target state population versus time. A) DC field profile; B) Target state population. The initial state begins in the wide well with minimal overlap with the target state. The dc field drives the electron density into the narrow well, and then back to the wide well. Adapted from K. L. Shuford and J. L. Krause, J. Phys. D **36**, 439 (2003).[192]

Among all of the field profiles tested, the slightly nonlinear field (Figure 6–6, Panel C) is the most efficient for the structure examined. The initial state proceeds from the wide well to the narrow well with the least amount of mixing. It should be stressed that the goal is to move the electron density efficiently in the shortest time possible. Each of the fields tested could, of course, satisfy the adiabatic criterion

strictly with longer induction times. However, dephasing places an upper limit on the time available to perform the transition. It may be that a field designed using optimal control theory can increase the performance, primarily by decreasing the induction time. Tests of this idea are underway using local control theory.[73,74]

Finally, it is worth noting that the method of adiabatic passage discussed above is reversible. It is possible to return the final state to its initial position in a controlled manner. Once again, the field deemed most efficient above is used. The field varies from zero to -40 kV/cm, remains constant for a short time, and then the magnitude decreases to zero. Figure 6–8 shows the dc field used, and the population of the target state. The target state is the lowest eigenstate when the QW is biased by a -40 kV/cm dc field (Figure 6–1, Panel B). There is some overlap between the initial state and the target state, as can be seen by a population of ~ 0.1 at the initial and final times. At times from 5–7 ps, the electronic wave function is in the target state. Figure 6–9 shows a contour plot of the state dynamics. As can be seen in the figure, the probability density moves across the entire ADQW structure, remains constant for a short time in the narrow well, and then returns along the same path to the wide well.

As the results presented show, adiabatic passage provides a method for selective population of a desired quantum well. A stationary charge density can be placed in either well by using an appropriate dc field. In a sense, each well is associated with a characteristic magnitude of the field. Charge can be localized in a chosen well, if enough time is allowed to evolve adiabatically to that spatial region. The upper limit of the time available for the field induction is set by the excited-state lifetime of the charge carriers. However, this method of adiabatic passage might be completed more quickly by optimizing the parameters of the structure or the field. Structures with sizeable energy splittings between states, for example, would ease the requirements

for adiabaticity. This, in fact, is the reason that a notched double well is used in this work.

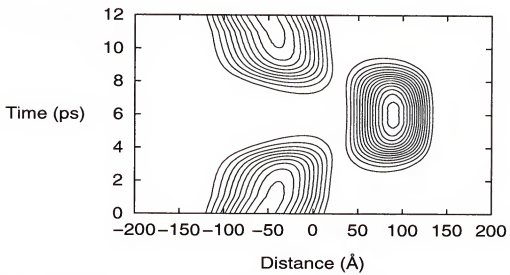

Figure 6–9: Contour plot of population evolution. The field induces an adiabatic passage of the population from the wide well to the narrow well, and then back along the same path to the wide well. Adapted from K. L. Shuford and J. L. Krause, J. Phys. D **36**, 439 (2003).[192]

6.4 Conclusions

Adiabatic passage between the wells of an ADQW structure can be achieved using a time-dependent dc field. With an appropriate field, the electronic density can be driven to a chosen quantum well at a specified time. The induction time of the field is a sensitive variable, dictating whether or not the process is effective and efficient. If the time duration is long enough, smooth adiabatic passage is observed from the initial state to the final state. If the induction time is too short, state mixing occurs, and a wave packet is created that spoils the efficiency. In general, the Hamiltonian must be transformed such that the energy differences between the close-lying states are complemented by the time-variation of the dc field. As a result, the form of the optimal dc field depends sensitively on the detailed response of the system to the field. By suitably tailoring the potential profile of the quantum well, the severity of the limitations enforced by the adiabatic criterion can be lessened. Finally, the

population transfer is reversible, and complex fields can be used to produce multiple density shifts between the quantum wells.

It is tempting to speculate that the methods described in this work may find application in the laboratory as optoelectronic devices, or components in quantum information processing. The basic idea, to control the flow of charge in a confined region of space, has certain elements of an ultrafast switch.[121,193] If the results can be extended to multiple quantum wells, the ability to populate a chosen well and to detect the density in that well, could allow reduced dimensionality systems to be used as quantum registers for encoding and manipulating quantum information.[25,26] Indeed, schemes utilizing adiabatic passage to perform qubit rotation and quantum searches have been suggested recently.[27,28]

CHAPTER 7
COULOMB EFFECTS REVISITED

In this chapter, the Coulomb attraction between carriers is re-investigated in a more rigorous fashion. Both the static effects on the system, such as distortion of the quantum well potential, and the variation of dynamics caused by the interaction are considered. A previous model is altered slightly to allow the observation and interpretation of the induced effects more clearly. The theoretical approach, assumptions, and material parameters are the same as used previously. For a thorough discussion of the excitation conditions and system properties, see Chapter 4. The salient features of the previous model are presented below, as well as a discussion regarding the new portion of the methodology.

7.1 New Exciton Model

Cylindrical coordinates (ρ, ϕ, z) are appropriate due to the symmetry of the quantum well (QW) system. The dimensions perpendicular to z are separated into center of mass (neglected here), and relative coordinates. The Hamiltonian for an electron and a heavy hole interacting via a Coulombic potential is

$$\mathcal{H} = H_e\left(z_e\right) + H_h(z_h) + T_{rel}\left(\rho, \phi\right) + V_{coul}\left(\rho, z_e - z_h\right). \tag{7.1}$$

The terms in this equation are defined as

$$H_e = -\frac{\hbar^2}{2m_e^*}\frac{\partial^2}{\partial z_e^2} + V_e\left(z_e\right) + eFz_e, \tag{7.2}$$

$$H_h = -\frac{\hbar^2}{2m_h^*}\frac{\partial^2}{\partial z_h^2} + V_h\left(z_h\right) - eFz_h, \tag{7.3}$$

$$T_{rel} = -\frac{\hbar^2 \nabla_\rho^2}{2\,\mu_\perp}, \tag{7.4}$$

and

$$V_{coul} = -\frac{e^2}{4\pi\epsilon_0\epsilon}\frac{1}{\sqrt{\rho^2 + (z_e - z_h)^2}}, \tag{7.5}$$

where $m^*_{e,h}$ are the effective masses in the dimension parallel to the growth direction, $\mu_\perp$ is the effective mass in the perpendicular plane, $V_{e,h}$ are the confining QW potentials, F is a static dc field, V_{coul} is the Coulomb interaction, and ϵ is an average dielectric constant. The complete, 1s exciton wave function is approximated by the product trial function

$$\Phi(z_e, z_h, \rho) = \psi_e(z_e)\,\psi_h(z_h)\,\psi_{rel}(\rho), \tag{7.6}$$

where ψ_e and ψ_h are the lowest single particle eigenstates. The in-plane motion is represented by the variational wave function

$$\psi_{rel}(\rho) = \sqrt{\frac{2}{\pi}}\frac{1}{\lambda}\exp\left[\frac{-\rho}{\lambda}\right], \tag{7.7}$$

where λ is a parameter that is varied to minimize the energy. The expectation value of the energy for the exciton is

$$\langle\Phi|\mathcal{H}|\Phi\rangle = E_e + E_h - E_b, \tag{7.8}$$

where E_e and E_h are the energy of the electron and heavy hole respectively, and E_b is the exciton binding energy. Two terms contribute to the binding energy given as,

$$-E_b = \int_0^{2\pi}\int_0^{\infty} \psi^*_{rel}\,T_{rel}\,\psi_{rel}\,\rho\,d\rho\,d\phi + \langle\Phi|\,V_{coul}\,|\Phi\rangle \tag{7.9}$$

The first expression on the right hand side can be evaluated analytically as $\hbar^2/2\mu\lambda^2$. The second term can be written explicitly as

$$\int_{dz_h}\int_{dz_e}\int_0^{2\pi}\int_0^{\infty} \psi^*_e\,\psi^*_h\,\psi^*_{rel}\,V_{coul}\,\psi_e\,\psi_h\,\psi_{rel}\,d\tau, \tag{7.10}$$

where $d\tau = \rho\, d\rho\, d\phi\, dz_e\, dz_h$. Simplifying this expression gives

$$-\frac{e^2}{4\pi\epsilon_0}\frac{4}{\epsilon\lambda^2}\int dz_e\, \psi_e^*\, \psi_e \int dz_h\, \psi_h^*\, \psi_h \int_0^\infty d\rho\, \frac{\rho\, e^{-2\rho/\lambda}}{\sqrt{\rho^2 + (z_e - z_h)^2}}. \tag{7.11}$$

The integral over ρ can be solved as

$$|z_e - z_h| \left\{ \frac{\pi}{2} \left[H_1(\xi) - Y_1(\xi) \right] - 1 \right\}, \tag{7.12}$$

where $\xi = \frac{2}{\lambda}|z_e - z_h|$, H is a first order Struve Function, and Y is a Bessel Function of the second kind.

The variational parameter is found by minimizing the total energy (essentially maximizing the binding energy). The total energy of the exciton can be lowered further by allowing the Coulomb attraction to affect the confined dimension explicitly. This is incorporated by including a single-particle, average potential that accounts for the interaction, and then re-diagonalizing to obtain new eigenstates for the electron and hole that "feel" each other. Interaction potentials W_e and W_h are calculated at each grid point, and then added to the QW potential. The effect is to decrease the potential in regions where the Coulomb attraction is greatest.

The new single particle Hamiltonians take the form

$$\bar{H}_i = -\frac{\hbar^2}{2m_i^*}\frac{\partial^2}{\partial z_i^2} + V_i^{eff}, \tag{7.13}$$

with

$$V_i^{eff} = V_i(z_i) \pm eFz_i + W_j. \tag{7.14}$$

In Equation (7.14), V_i is the QW potential, F is a dc field (the + sign is for electrons, and the − sign is for holes), i = (e or h), and $j \neq i$. The interaction potentials are defined as

$$W_j = \frac{1}{2}\int_{dz_j}\int_0^{2\pi}\int_0^\infty \psi_j^*\, \psi_{rel}^* \left[T_{rel} + V_{coul} \right] \psi_j\, \psi_{rel}\, \rho\, d\rho\, d\phi\, dz_j. \tag{7.15}$$

Note that the interaction potentials have a form similar to Equation (7.9), and that

$$\int dz_e \psi_e^* W_h \psi_e + \int dz_h \psi_h^* W_e \psi_h = -E_b \tag{7.16}$$

is strictly true. The sum of the single particle effective energies,

$$\langle \psi_e | \bar{H}_e | \psi_e \rangle + \langle \psi_h | \bar{H}_h | \psi_h \rangle = \bar{E}_e + \bar{E}_h, \tag{7.17}$$

closely represents the total exciton energy obtained previously in Equation (7.8). In addition, the shifting of energy levels due to the Coulomb attraction is approximately the binding energy

$$|E_e - \bar{E}_e| + |E_h - \bar{E}_h| \approx E_b. \tag{7.18}$$

In many simple cases this is exact, however in more complex systems there are slight discrepancies from the re-diagonalization process, as discussed below.

Similar procedures for calculating accurate envelope functions are suggested by Wu.[194] The method above is slightly different because Wu assumes one envelope function is frozen, and varies only the other function. Wu finds this method to be ideal for structures with large binding energies or small band gap offsets. In addition, he notes that there is a relatively small energy difference between using 2-D (as above) and 3-D relative wave functions, which couple all dimensions in the exponential. This observation is beneficial because it alleviates concerns about wider wells, where the 2-D relative wave function does not represent the system as well.

The new exciton method takes the re-diagonalization suggestion further by implementing an iterative scheme. After approximately seven iterations, the effective energies and the total exciton energy are lower, and constant to eight decimal places. The entire procedure is outlined below:

1. Solve for the envelope functions without V_{coul}.
2. Minimize the energy to obtain the exciton radius, λ.
3. Calculate W_e and W_h and construct $\bar{H}_e$ and $\bar{H}_h$.

4. Solve for new envelope functions $\bar{\psi}_e$ and $\bar{\psi}_h$ and effective energies $\bar{E}_e$ and $\bar{E}_h$.
5. Return to step 2 until convergence in energy is achieved.

7.2 Static Effects

The new model is tested first on a simple, single-well structure, where the value of the binding energy is well-known. A 60 Å well is used in the absence of a bias field. Under these conditions, the maximum overlap exists between the lowest hole and electron states. Therefore, this situation represents the largest possible distortion to the potential from the Coulomb interaction due to the localization of charge in a relatively small area.

The 1s exciton binding energy[162,163,168] for GaAs/AlGaAs quantum wells with widths less than 100 Å is 8–9 meV. The value calculated without the iterative scheme is 8.664 meV, in excellent agreement with experiment. After several iterations this value increases to 8.674 meV, thus lowering the total exciton energy. The iterative scheme lowers the binding energy by 0.115% of the original value. While the energy is not shifted by a large amount, the effects can be readily observed in Figure 7–1 by the distortion in the effective QW potentials. The dips in the potentials reflect spatial regions in which the lowest electron and hole wave functions have the most overlap, and hence the greatest attraction. The variations in the states themselves are much less noticeable. Each state becomes narrower and more peaked as a result of the interaction, however the Gaussian-like shape of a ground state wave function is maintained.

The effective energies equally split the binding energy. The Coulomb attraction shifts each uncoupled energy level by half of the binding energy. Tables 7–1 and 7–2 display the pertinent information regarding the energetics of the structures presented in this chapter. Propagation of the converged states ($\bar{\psi}_e$ and $\bar{\psi}_h$) with the effective Hamiltonians produces the expected results in these conditions. The average values of position are zero, and the average values of the effective potential are constant

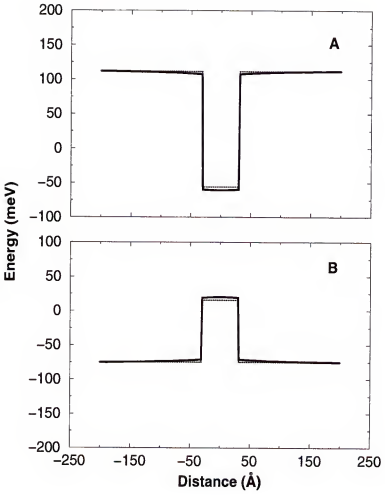

Figure 7–1: Quantum well energy profiles with (solid lines) and without (dotted lines) the Coulomb interaction. A) Electron effective potential; B) Hole effective potential. The lowest eigenvalue neglecting the Coulomb interaction is chosen as the zero of energy.

and shifted by $\frac{1}{2}E_b$ from the original, uncoupled values. These results are anticipated because the system is symmetric, and the converged states are eigenstates of the system using the effective, single-particle Hamiltonians. Note that the more energetic eigenstates are not shifted by the same amounts as the lowest states. The model is not created to address them specifically, and they occupy different spatial regions, which are not affected by V^{eff} in the same manner. For example, the second state in each band has a node where the ground states have maxima.

Table 7–1: Eigenvalues Neglecting the Coulomb Attraction[a]

Structure	Bias (kV/cm)	E_{1h}	E_{2h}	E_{1e}	E_{2e}
single well	0	0	-42.74	0	112.72
double well	0	0	-5.43	0	22.16
double well	-12	0	-17.46	0	16.52

[a] All energies are given in meV. Note that the zero of energy is taken as the lowest eigenvalue in each band.

Table 7–2: Eigenvalues Including the Coulomb Attraction[b]

Structure	Bias (kV/cm)	$\bar{E}_{1h}$	$\bar{E}_{2h}$	$\bar{E}_{1e}$	$\bar{E}_{2e}$	λ(Å)	E_b
single	0	4.34	-38.78	-4.33	110.18	124.64	8.67
double	0	3.68	-3.47	-3.66	20.20	142.00	7.38
double	-12	3.18	-14.73	-3.13	14.03	158.66	6.38

[b] All energies are given in meV. Note that the zero of energy is taken as the lowest eigenvalue in each band.

Next, a slightly more complicated structure is investigated. Specifically, this structure is an asymmetric double quantum well (ADQW) with dimensions 100/20/70, representing the dimensions in Å of the left well/barrier/right well, respectively. The binding energy drops to 7.363 meV, which is 1.3 meV less than in the single well due to the spreading of charge in the conduction band. The smaller effective mass of the electron allows it to tunnel through the barrier to the right well, which reduces the overlap with the hole state. Again, the Coulomb interaction induces a "bowing" of the effective potentials as seen in Figure 7–2. A larger distortion is noted in the left well than in the right well. This is the spatial region in which the lowest hole state is localized almost exclusively, and the lowest electronic state displays the most density, so the effective potential will be modified more strongly in this area. The electronic eigenstates are changed slightly more than the hole states by the Coulomb interaction. In both bands, the states are shifted towards regions of lower energy (the wide well) as seen in Figure 7–3. The energetic shifts of the lowest states do not equal the binding energy exactly. The discrepancy is ~ 0.04 meV, which is four times

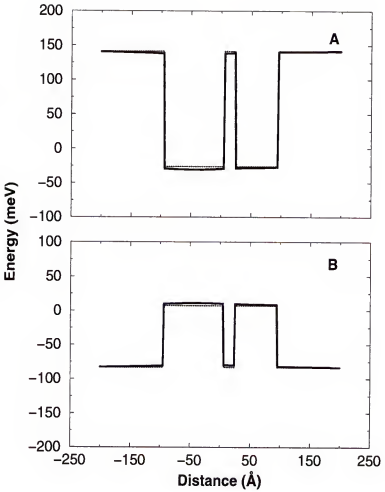

Figure 7–2: Quantum well energy profiles with (solid lines) and without (dotted lines) the Coulomb interaction. A) Electron effective potential; B) Hole effective potential. The lowest eigenvalue neglecting the Coulomb interaction is chosen as the zero of energy.

larger than in the single well case. This is a more complicated system, and therefore the re-diagonalization step introduces the larger variations.

Application of a dc field alters the situation described above slightly. Here the same ADQW is used, however now it is biased with a −12 kV/cm dc field. The field brings the electronic energies of the two lowest states (excluding V_{coul}) to their closest point. The Coulomb attraction again affects the wells in essentially the same manner as seen in Figure 7–4. When the double well is biased, the eigenvectors are altered much more by the Coulomb interaction as displayed in Figure 7–5. The

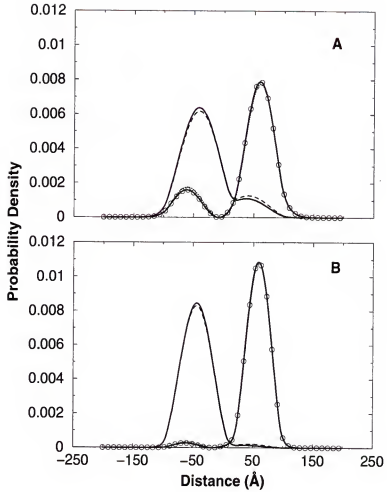

Figure 7–3: Quantum well eigenvectors. A) Electronic eigenvectors; B) Hole eigenvectors. In both panels, the dashed line and dotted line are the eigenstates ignoring V_{coul}, ψ_{1i} and ψ_{2i}, respectively where $i = e, h$. The solid line and the open circles are the eigenstates including V_{coul}, $\bar{\psi}_{1i}$ and $\bar{\psi}_{2i}$, respectively where $i = e, h$.

lowest electronic state is shifted to the wide well, and the lowest hole state is very slightly angled towards the corresponding electronic state. The second electronic state is shifted more to the narrow well. Apparently, the energy decrease present in the narrow well is enough to localize the state in this spatial region. The second hole state is slightly shifted to the wide well. The electronic states are altered severely by the Coulomb attraction when the system is biased. The hole states are not affected as much, however more than in the previous examples. Here again, the magnitude of the energy shifts resulting from the Coulomb interaction do not equal the binding

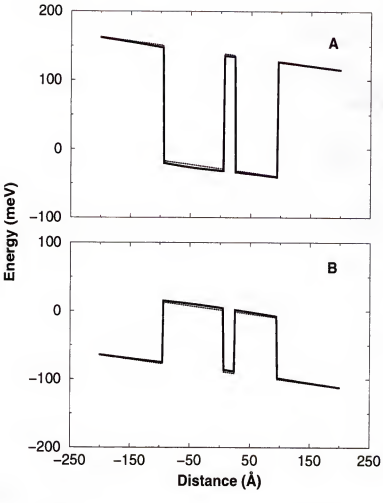

Figure 7–4: Quantum well energy profiles with (solid lines) and without (dotted lines) the Coulomb interaction. A) Electron effective potential; B) Hole effective potential. The lowest eigenvalue neglecting the Coulomb interaction is taken as the zero of energy.

energy exactly. The difference is ~ 0.07 meV. As the electronic charge becomes more delocalized, this discrepancy is increased.

7.3 Effects on Dynamics

The static effects on the potential, eigenvectors, and eigenvalues are important and easily viewable. The next step is to examine the primary concern of this investigation, specifically the dynamic effects on the charge carriers due to the interaction. Numerous earlier studies regarding carrier dynamics have neglected the Coulomb attraction in such systems. The goal of this section is to evaluate how accurate these

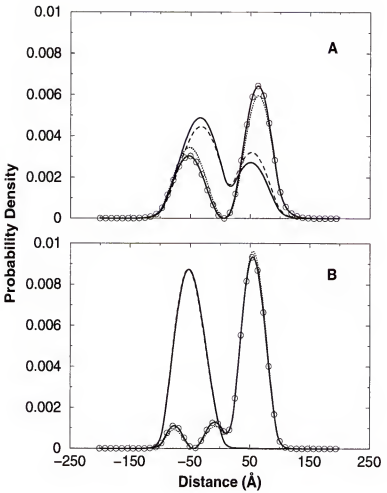

Figure 7–5: Quantum well eigenvectors. A) Electronic eigenvectors; B) Hole eigenvectors. In both panels, the dashed line and dotted line are the eigenstates ignoring V_{coul}, ψ_{1i} and ψ_{2i}, respectively where $i = e, h$. The solid line and the open circles are the eigenstates including V_{coul}, $\tilde{\psi}_{1i}$ and $\tilde{\psi}_{2i}$, respectively where $i = e, h$.

studies are, and to specify conditions in which this interaction is crucial to achieve reliable results.

A common situation in systems such as the biased ADQW is that of a stationary charge density in the valence band and a coherent superposition state in the conduction band. To simulate this situation, a wavepacket composed of electronic eigenstates is placed in the conduction band, while the lowest hole state resides in the valence band. Both charge densities are then propagated forward in time. It is assumed that the excitation across the band gap has occurred before the simulation

begins. To reiterate, a system composed of a single stationary state in the valence band and a superposition state in the conduction band is propagated as in the ADQW results presented in earlier chapters. This scenario is reasonable because in systems similar to these, it has been shown experimentally that the dynamics are dominated by the electrons.

Results obtained from a propagation using the envelope functions excluding the Coulomb attraction, and results using the converged excitonic states coupled by the Coulomb term are compared to establish the precise effects of the Coulomb interaction. Specifically, the idea is to compare dynamics obtained from

$$i\hbar\frac{\partial\psi_{1h}}{\partial t} = H_h\psi_{1h} \qquad \text{and} \qquad i\hbar\frac{\partial\Psi_e}{\partial t} = H_e\Psi_e, \tag{7.19}$$

where

$$\Psi_e = \frac{1}{\sqrt{2}}\left(\psi_{1e} + \psi_{2e}\right), \tag{7.20}$$

to

$$i\hbar\frac{\partial\bar{\psi}_{1h}}{\partial t} = \bar{H}_h\bar{\psi}_{1h} \qquad \text{and} \qquad i\hbar\frac{\partial\bar{\Psi}_e}{\partial t} = \bar{H}_e\bar{\Psi}_e, \tag{7.21}$$

where

$$\bar{\Psi}_e = \frac{1}{\sqrt{2}}\left(\bar{\psi}_{1e} + \bar{\psi}_{2e}\right). \tag{7.22}$$

In both cases addressed below, the same ADQW is used. First, the dynamics of the exciton state are investigated when no bias field is applied. Figure 7–6 shows significant differences in the average position of the electronic wave packet when the Coulomb attraction is included. The frequency of oscillation and periods are noticeably different. These effects can be traced to the energy shifts, and the splitting between electronic basis states one and two. This splitting governs both the frequency and period of oscillation. The Coulomb term induces a frequency shift of 0.41 THz, and a period shift of -13.23 fs. The average position of the hole state is roughly the same in both cases as can be seen in Figure 7–6. Interestingly, the Coulomb

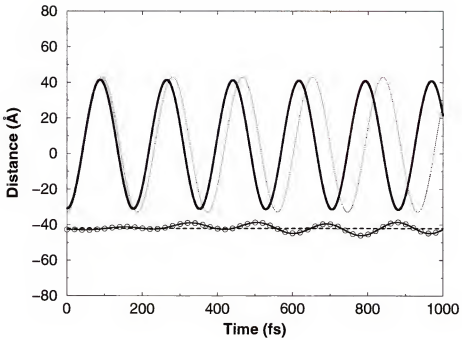

Figure 7–6: Average position of charge carriers. The electronic wave packet including the Coulomb attraction is represented with the solid line, and the uncoupled electronic wave packet is with the dotted line. The hole state including the Coulomb attraction is represented with the open circles, while the hole state neglecting the interaction is represented with a dashed line.

attraction to the electronic wave packet induces an oscillation in the hole state not observed when neglecting this interaction. This dynamic effect is due only to the Coulomb interaction. If the oscillation were from a contribution of another hole state, the the period would be in excess of 575 fs. As the plot of the average positions displays, the electronic wave packet samples both wells periodically, while the hole state is confined to the wide well. Plots of the carrier dynamics can be seen in Figures 7–7 and 7–8. The binding energy oscillates with the frequency of the electronic wave packet. As the electronic wave packet tunnels to the narrow well, the electron-hole attraction decreases, the binding energy decreases, and the exciton radius increases (Figure 7–9). Under these conditions, the quantum wells are not strongly coupled, and the Coulomb effects on the carrier dynamics are observed easily.

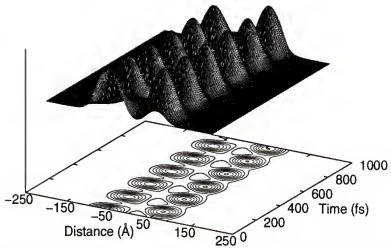

Figure 7–7: Electron dynamics coupled to a hole by a Coulomb attraction.

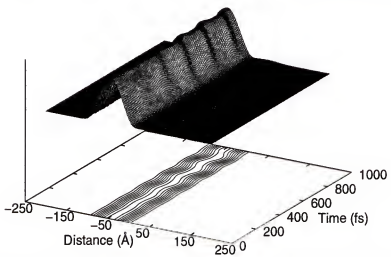

Figure 7–8: Hole dynamics coupled to an electron by a Coulomb attraction.

Next, the ADQW system is biased by a -12 kV/cm dc field. As noted previously, the field alters the eigenvectors of the system significantly. Following the same procedure as above leads to slightly different results. The Coulomb effects are not as pronounced when the ADQW is biased by a field of this magnitude. Both the frequency and period of the wave packet are still shifted, but the effect on the dynamics is much less than above, as seen in Figure 7–10. The frequency shift is 0.15 THz, and the shift in the period is -9.27 fs. The effects on dynamics are not as great in this case because the first and second electronic states are more similar in character. Therefore, the energy shifts are comparable, leaving the splitting (which dictates the

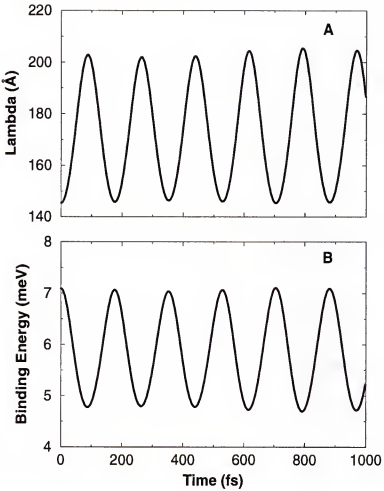

Figure 7–9: Time evolution of exciton radius and binding energy. A) λ; B) E_b. Both oscillate with the same frequency as the electronic wave packet.

frequency of oscillation) close to the original value. The oscillation present in the average position of the hole is much less than in the previous example. This result can be attributed to the more constant effective potential experienced by the carriers, which leads to less oscillation in the valence band. The relatively constant character of the potentials is a result of the stronger coupling between the two wells. Figure 7–11 shows a plot of the average effective potentials. The overall dynamics of the electronic wave packet and the hole state are qualitatively similar to the results presented above, however the effects of the Coulomb attraction are not as great when the ADQW is biased, and strongly coupled.

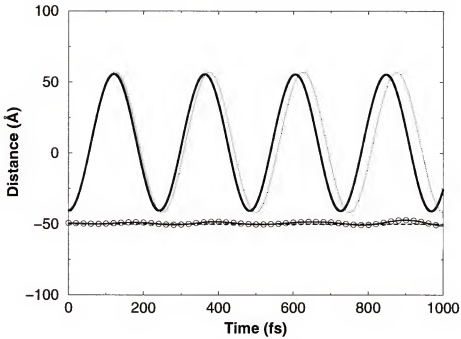

Figure 7–10: Average position of charge carriers. The electronic wave packet including the Coulomb attraction is represented with the solid line, and the uncoupled electronic wave packet is with the dotted line. The hole state including the Coulomb attraction is represented with the open circles, while the hole state neglecting the interaction is represented with a dashed line.

7.4 Conclusions

This chapter presents a modified version of an earlier method to include the effects of Coulomb interactions, which can be used to simulate dynamics in an excitonic system. The new method yields improved results for the binding energy, and produces a clear description of the effects of Coulomb interactions on carrier dynamics. This method shows that the Coulomb interaction can play a larger role than previous calculations indicated. The static effects, such as distortion of potential profiles, alteration of eigenvectors, and shifting of energy levels are fairly intuitive. The magnitude of the effects on the dynamics varies depending on the conditions. When the wells are loosely coupled, the effects on wave packet dynamics are much greater than when the wells are strongly coupled. In the former case frequency shifts on the order of of 0.41 THz and period shifts of 13 fs can be expected, while in the latter case

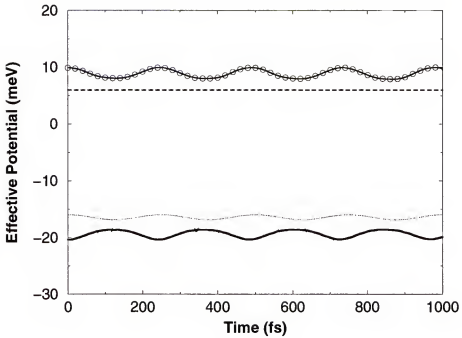

Figure 7–11: Time evolution of average effective potentials. The solid line and the dotted line show the electronic potentials including and neglecting the Coulomb term, respectively. The open circles and the dashed line show the hole potentials including and neglecting the Coulomb term, respectively.

frequency shifts of 0.15 THz and period shifts of 9 fs can be expected. Note that the loosely coupled system is the "worst case scenario" for wells of typical dimension and character such as the ones studied here. In addition, the shifts in period are only tens of femtoseconds, and thus are certainly on an ultrafast time scale. In some cases the slight differences may not even be observable without the latest laser technology. In each situation studied, the hole state remains localized in the wide well, while the electronic wave packet spreads across both quantum wells. On short time scales, the Coulomb interaction does not alter the results significantly. However, over long time scales the electronic wave packets including and neglecting the Coulomb attraction become out of phase. While neglecting the Coulomb attraction gives qualitatively correct results, attempts to localize charge density at long times (on the order of picoseconds), or to control the frequency of oscillation precisely must include the Coulomb effects. Ignoring the attraction produces results that are not robust.

CHAPTER 8
CONCLUSIONS AND FUTURE WORK

The preceding chapters introduce the subject of quantum control, and present several examples of controlling charge carrier dynamics in semiconductor heterostructures. A common goal is to discover electric fields that actively manipulate and control quantum systems, while achieving a predetermined target objective. Control objectives range from localizing charge in a narrow spatial region, to controlling the properties of emission such as frequency and amplitude. In each case considered, simple, experimentally feasible laser pulses can be used to control carrier dynamics, and achieve the target objective. A brief synopsis of the dissertation is below, followed by suggestions for possible areas of future work.

Chapters 1 and 2 introduce the two main topics, quantum control and quantum wells. An abbreviated history of quantum control, as well as reasons that one might want to use coherent laser fields to control system properties is presented. In addition, the rudiments of quantum wells are discussed, including what they are, how the effective potentials are created, and why they are attractive to scientists working in the field of quantum control. The technological importance of these systems, and numerous device applications are noted. A thorough literature review summarizes some control methods for atoms and molecules, and highlights the few examples of quantum control reported in semiconductors.

Chapter 3 presents the envelope function approximation used to treat charge carriers in bulk and quantum-confined systems. A perturbative treatment is developed based on several reasonable assumptions. The perturbative solution follows a framework reminiscent of methods describing molecular dynamics. This allows the

use of previously tested, and proven methods for optimization of electric fields. Control theory is discussed briefly, and procedures to optimize laser fields for a particular control objective are outlined. In one application, a genetic algorithm is used to search for the optimal pulse parameters that excite carriers across the band gap, and localize the electronic density in a chosen quantum well, at a specified time. The search procedure is highly successful at attaining the objective, displaying nearly perfect control of electron dynamics. Several factors that might limit the controllability are investigated, such as fluctuations in the dc field, sample imperfections, and environmental coupling. In all cases, a re-optimization of the field can compensate for the differences, adjust the laser accordingly, and again maximize the performance. Similar results are found in more complex, multiple-well systems like superlattices. It is noted that the chirp parameter is not necessary in any of the cases studied to achieve optimal results.

Chapter 4 investigates the effects of the Coulomb interaction between holes and electrons on charge carrier dynamics. The magnitude of the attraction depends on the instantaneous separation between the electron and the heavy hole. The goal is to clarify the extent to which this interaction modifies carrier dynamics in typical quantum well systems, and note the effects on control. Calculated energy values such as the exciton binding energy are in good agreement with experimental values. Again, controlling electronic wave packet dynamics is the primary objective. Simulations are performed both including, and neglecting the Coulomb attraction. It is found that only small discrepancies are observed when the wave packets have similar compositions. Further, a slight shift in laser parameters can compensate for any differences that the interaction might induce. Therefore, under certain conditions, the Coulomb attraction can safely be neglected in simulations of charge carrier dynamics.

Chapter 5 is concerned with controlling the emission of electromagnetic radiation from quantum wells. An intraband polarization is created when a wave packet

is created in the conduction band, and oscillates between wells. The moving charge density leads to emission from the quantum wells that typically radiates in the THz regime (far IR, sub-mm). The characteristics of the radiation can be varied making these systems controllable THz emitters or detectors. The emission frequency can be shifted over a range of several THz by adjusting the dc bias field. The emission amplitude can be adjusted by varying the frequency of the excitation laser. In addition, pairs of phase-locked pulses can create interference effects, such as signal amplification or annihilation. These methods provide a means to control the radiation frequency and amplitude. The signals can be designed, and created to accomplish a desired objective. Examples such as relative population control of vibrational states in a diatomic molecule, and complete population inversion in a two-level system are explored. Other applications for THz emitters and detectors include environmental sensing and biological imaging.

Chapter 6 presents a method to perform adiabatic passage in quantum well systems. A slowly varying dc field induces a controlled transfer of the electronic charge density between quantum wells. A general criterion for adiabaticity is derived that specifies conditions when the passage is most efficient and successful. Properties such as field induction time and field shape are crucial. The field must cause variations in the Hamiltonian that are complimented by other factors (such as energy separation) to avoid state mixing, and produce smooth passage. It is also demonstrated that the passage in reversible. The population can be moved by the field, and then returned along the same path. The adiabatic passage procedure has certain elements of an ultrafast switch, and similar processes have recently been speculated as useful for quantum computation and quantum registers.

Chapter 7 revisits the effects of the Coulomb interaction. The previous method is altered slightly to re-evaluate the extent of the effects. Modifying the methodology improves results slightly, and allows for an easier interpretation of effects on the

system. Distortions in the potential and the eigenvectors, as well as shifts in the eigenvalues are observed readily. Regions in which the Coulomb attraction is greatest display the most obvious effects. The model is tested in both single- and double-well systems, and performs well in each case. Dynamic effects such as the oscillation period and frequency also display the effects of the Coulomb attraction. When the wells are loosely coupled the effects are much greater than when the wells are strongly coupled. The analysis provides information about when the effects must be considered, and when the Coulomb interaction can be neglected.

All of the preceding studies display the versatility of QW structures. Numerous applications are presented for a relatively small number of new systems. The ability to customize well dimensions and depth allow a degree of freedom not present in molecular systems. Simply changing the well width, or stoichiometry of the materials can yield a potential better equipped to display a certain phenomenon of interest. These traits make layered semiconductor heterostructures rich areas for future study.

Future versions of the model must address some interactions neglected previously. Because of the dual process of calculating system dynamics, and optimizing laser fields, the models to date have been simplified considerably. The added computation time needed for optimization limits the complexity of theoretical treatments. In some cases, the above models are not adequate to accurately describe system dynamics. Examples are chosen specifically in which the major contributions to charge carrier dynamics have been identified previously. This allows some interactions to be neglected with a high degree of confidence. In order to move to more complex systems, or most importantly, to develop a unified treatment that can handle both simple and complicated systems, new interactions must be included. At the top of this list are many-body effects such as carrier-carrier interactions. This will allow excitation with more intense laser pulses, which cause significant population transfer between bands. Also, to treat systems at higher temperatures, phonons and energy

dissipation must be addressed. In addition, it is beneficial to develop a close collaboration with experimentalists in the field. The feedback can be important when developing future theoretical treatments.

Several other methods of control not explored in this dissertation appear to be applicable to quantum well systems. Forms of local control, and the Brumer-Shapiro interference method may be possible candidates for experimental and theoretical studies. Local control is attractive because the computation required to calculate electric fields is reduced compared to iterative methods, which allows studies of more complex systems. Pairs of laser fields that coherently excite a state with different frequencies might be used to control wave packet density in a given well. Indeed, similar investigations have already shown the possibility to control photocurrent magnitude and direction. Experimental groups conducting semiconductor research are just now beginning to use feedback loops to control system properties. This is a logical direction for future work. The results have been quite impressive in molecular work, in which the systems of interest are large, complicated molecules in solution. Success in such immensely complex systems makes the likelihood of similar results in semiconductor systems highly probable.

APPENDIX A
QUANTUM WELL BASICS

Quantum wells are created by the misalignment of energy bands present in different semiconductor materials. The prototypical III-V semiconductor material combination is $GaAs/Al_xGa_{1-x}As$. A vast amount of experimental and theoretical work has been devoted to characterizing the energetic properties of this material. Spectroscopic measurements show that the increase in band gap is proportional to the amount of Aluminum in the alloy. Numerical fits to experimental data and interpolation schemes can produce expressions describing the energy dependence as a function of alloy composition. Some examples taken from Adachi[195] for the direct band gap at 300 K are

$$E_g^{\Gamma}(x) = 1.424 + 1.247\,x \qquad (0 \le x \le 0.45), \tag{A.1}$$

$$E_g^{\Gamma}(x) = 1.424 + 1.247\,x + 1.147\,(x - 0.45)^2 \qquad (0.45 < x \le 1.0), \tag{A.2}$$

where all energy values are in electron volts (eV). These equations provide the band gap of AlGaAs by adding some change of energy to the value of the band gap for GaAs (1.424 eV). This change in band gap, ΔE_g, is from the addition of Al. The energy dependence has a similar functional form for low temperature studies, except for the band gap of pure GaAs is 1.52 eV.

The preceding discussion yields the absolute energy difference between the top of the valence band edge and the bottom of the conduction band edge for different layers. However, it provides no information about how the bands are arranged with each other. For example, the valence band edges of the two materials might be level, and the entire energy difference could reside in the conduction band edges, or vice versa. In fact, the observed energy differences are a combination of both band edges

being offset. The accepted values[144,163] in the literature suggest a split ratio within a few percent of 60:40. This gives the conduction band offset as 60% of ΔE_g and the remainder in the valence band offset. Therefore, the depth of the quantum well the electronic carriers experience is 0.6 times the band gap difference between GaAs and AlGaAs. The well depth the holes experience is 0.4 times the energy difference.

While the offset ratio is considered a constant, the change in band gap can be adjusted by adding more Al. It is both the amount of Al, and the band gap offset that control the depth of quantum wells in the heterostructure. The means to control well depth, coupled with the experimental capability to control well dimensions, provides an opportunity to create quantum well structures with certain characteristics. Assuming some knowledge of the system, the potential felt by charge carriers can be engineered to optimize a given task. The experimenter can determine the properties desired for the project, and design the dimensions and composition of the structure to the appropriate specifications.

APPENDIX B
POPULATION INVERSION IN TWO-LEVEL SYSTEMS

The system of interest consists of two levels described by states $|\phi_1\rangle$ and $|\phi_2\rangle$, with energies E_1 and E_2, respectively. The goal is to find the conditions in which a laser field coupling these two levels produces complete population transfer. The interaction of the two-level system with a laser field is

$$i\hbar\dot{\Psi}(t) = [H_0 - \mu\,\varepsilon(t)]\,\Psi(t), \tag{B.1}$$

where H_0 is the field-free Hamiltonian, μ is the dipole moment, and ε is the electric field. The state of the system is described by

$$\Psi(t) = a_1(t)|\phi_1\rangle e^{-i\omega_1 t} + a_2(t)|\phi_2\rangle e^{-i\omega_2 t}, \tag{B.2}$$

where $\omega_i = E_i/\hbar$. Inserting B.2 into B.1 leads to expressions for the expansion coefficients

$$\dot{a_1} = \frac{i\varepsilon}{\hbar}\langle\phi_1|\mu\,|\phi_2\rangle\, a_2\, e^{-i\omega_{21}t}, \tag{B.3}$$

$$\dot{a_2} = \frac{i\varepsilon}{\hbar}\langle\phi_2|\mu\,|\phi_1\rangle\, a_1\, e^{i\omega_{21}t}, \tag{B.4}$$

where $\omega_{21} = (\omega_2 - \omega_1)$. Note that terms containing integrals of the form $\langle\phi_i|\mu\,|\phi_i\rangle$ are zero due to parity. We assume the electric field can be written as $\varepsilon(t) = E\cos(\omega t)$, where E is the envelope and ω is the laser frequency. Inserting this expression gives the coefficients as

$$\dot{a_1} = \frac{i\Omega_{12}}{2}\, a_2 \left[e^{-i(\omega+\omega_{21})t} + e^{i(\omega-\omega_{21})t}\right] \tag{B.5}$$

$$\dot{a_2} = \frac{i\Omega_{21}}{2}\, a_1 \left[e^{-i(\omega-\omega_{21})t} + e^{i(\omega+\omega_{21})t}\right], \tag{B.6}$$

where Ω is the Rabi frequency defined as $\Omega_{ij} = \langle \phi_i | \mu | \phi_j \rangle \frac{E}{\hbar}$. At this point, it is common to make the Rotating Wave Approximation (RWA). RWA ignores terms that are far from resonance, and oscillating rapidly. It assumes that the laser frequency is nearly resonant with the transition from $|\phi_1\rangle$ to $|\phi_2\rangle$. This means that terms that oscillate at $\approx 2\omega_{21}$ are assumed to average to zero, and are neglected. Noting that $\Omega_{21} = \Omega_{12}$, the coefficients can be written as

$$\dot{a_1} = \frac{i\Omega}{2} a_2 e^{i\Delta t} \qquad \text{and} \qquad \dot{a_2} = \frac{i\Omega}{2} a_1 e^{-i\Delta t}, \tag{B.7}$$

where $\Delta = \omega - \omega_{21}$ is known as the frequency detuning. These coupled equations can be solved analytically if the pulse envelope, E, is constant.[180] Assuming that initially only $|\phi_1\rangle$ is occupied gives the solutions

$$a_1(t) = \left[\cos\left(\frac{\zeta t}{2}\right) - i\left(\frac{\Delta}{\zeta}\right)\sin\left(\frac{\zeta t}{2}\right)\right]\exp\left(\frac{i\Delta t}{2}\right) \tag{B.8}$$

$$a_2(t) = i\left(\frac{\Omega}{\zeta}\right)\sin\left(\frac{\zeta t}{2}\right)\exp\left(\frac{-i\Delta t}{2}\right), \tag{B.9}$$

where $\zeta = \sqrt{\Omega^2 + \Delta^2}$. The state populations as a function of time are then

$$|a_1|^2 = 1 - |a_2|^2 \qquad \text{and} \qquad |a_2|^2 = \left(\frac{\Omega}{\zeta}\right)^2 \sin^2\left(\frac{\zeta t}{2}\right). \tag{B.10}$$

When the laser field is resonant with the transition, the above expressions reduce to

$$|a_1|^2 = \cos^2\left(\frac{\Omega t}{2}\right) \qquad \text{and} \qquad |a_2|^2 = \sin^2\left(\frac{\Omega t}{2}\right). \tag{B.11}$$

As can be seen from Equations (B.11), when $\Omega t = \pi$ the population is inverted completely from $|\phi_1\rangle$ to $|\phi_2\rangle$. This means that all of the population resides in $|\phi_2\rangle$ when $\Omega t = n\pi$, where n is an odd integer. Increasing the magnitude of the detuning decreases the performance of the population transfer as can be seen in Figure B–1. Larger values of the detuning decrease the amount of population transferred, and causes a shift in the Rabi oscillations.

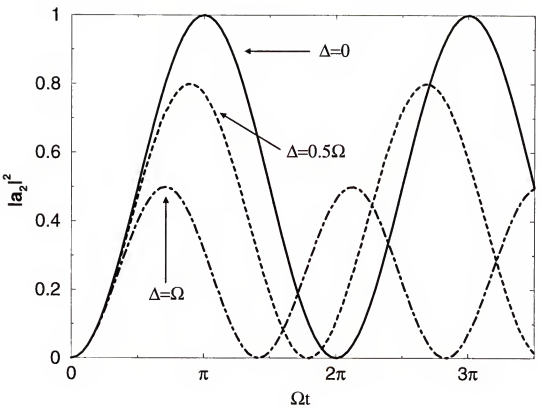

Figure B–1: Population of $|\phi_2\rangle$ versus the Rabi frequency multiplied by time (Ωt). When the electric field is on-resonance with the transition, the population is inverted from $|\phi_1\rangle$ to $|\phi_2\rangle$ when $\Omega t = \pi$. Increasing the detuning decreases the performance, and shifts the Rabi oscillation in phase.

In most cases of interest, the envelope of the laser is not constant. Often, a laser pulse is used to excite the system. The integral over time of the Rabi frequency is known as the pulse area. It is defined as

$$\text{Area} = \int_0^t dt' \, \Omega_{21} = \frac{\langle \phi_2 | \mu | \phi_1 \rangle}{\hbar} \int_0^t dt' E(t'), \tag{B.12}$$

where $E(t)$ is the laser pulse envelope. For resonant excitation, this definition of pulse area can replace Ωt in Equations (B.11), and accurately describes the state populations.[88,90] As in the constant envelope case, when the pulse area $= \pi$, complete population transfer occurs. For this reason, a laser pulse whose area satisfies this condition is termed a π-pulse.

APPENDIX C
PROPAGATION METHODS

Many problems in molecular dynamics require numeric solutions of the time-dependent Schrödinger equation,

$$i\hbar\frac{\partial\Psi}{\partial t} = H\Psi. \tag{C.1}$$

Equation (C.1) has the formal solution

$$\Psi(t) = U(t)\Psi(0) = T\exp\left[-\frac{i}{\hbar}\int_0^t H(t')\,dt'\right]\Psi(0), \tag{C.2}$$

where U is the evolution operator, T is a time-ordering operator, and H is the Hamiltonian operator. If the Hamiltonian operator is time-independent, T can be omitted, and the evolution operator is simply $U = -(i/\hbar)Ht$. In cases where direct diagonalization of the Hamiltonian matrix is not feasible, global propagators such as the Chebychev or Lanczos schemes can be used.[165,166] These methods make use of polynomial expansions to approximate the evolution operator. Global propagators are highly accurate, however without modifications intermediate time results are not obtained. For time-dependent Hamiltonians, the evolution operator can be divided into small increments of time in which H varies slowly. The evolution operator for a given time increment is then

$$U(\Delta t) = e^{-(i/\hbar)H(t)\Delta t}. \tag{C.3}$$

Two popular methods for approximating Equation (C.3) are discussed below.

C.1 Second-Order Differencing

The simplest method for propagating the wave function is found via a Taylor series expansion of Equation (C.3). This method is unstable, because time reversal

symmetry is not conserved.[166] However, a symmetric modification of the expansion achieves stability. One example is the relation

$$\Psi(t+\Delta t)-\Psi(t-\Delta t)=\left[e^{-(i/\hbar)H\Delta t}-e^{(i/\hbar)H\Delta t}\right]\Psi(t). \tag{C.4}$$

The exponential terms can be expanded as

$$e^{\pm i\phi}=1\pm i\phi+\frac{(i\phi)^2}{2!}\pm\frac{(i\phi)^3}{3!}+\frac{(i\phi)^4}{4!}\pm\cdots, \tag{C.5}$$

where $\phi = H\Delta t/\hbar$. This gives the new wave function propagated one step in time as

$$\Psi(t+\Delta t)\approx\Psi(t-\Delta t)-2(i/\hbar)H\Delta t. \tag{C.6}$$

This Second Order Differencing scheme preserves the norm and energy of the wave function. The error is on the order of $(E\Delta t)^3/3\hbar^3$.

C.2 Split Operator Method

This propagation method approximates the short time evolution operator as

$$U(\Delta t)\approx\exp\left[-\frac{i}{2\hbar}\frac{P^2}{2m}\Delta t\right]\exp\left[-\frac{i}{\hbar}V\Delta t\right]\exp\left[-\frac{i}{2\hbar}\frac{P^2}{2m}\Delta t\right], \tag{C.7}$$

where the kinetic and potential operators are propagated separately in their diagonal representations. The wave function is transformed to momentum space by a fast Fourier transform (FFT), and multiplied by $\exp(-iP^2\Delta t/4\hbar m)$ to propagate half of the kinetic step. Following this, the wave function is transformed back to the coordinate representation by inverse FFT, and multiplied by $\exp(-iV\Delta t/\hbar)$ for the propagation step of the potential. The final half step of the kinetic part is achieved in the same manner as previously, yielding a new wave function propagated by one time step. This procedure is repeated until all of the short time evolution operators have acted on the evolving state. The split-operator method conserves the norm of the wave function strictly, and is unconditionally stable.[165] The error is on the order of $(\Delta t)^3$.

APPENDIX D
GENETIC ALGORITHMS

In recent years, a new class of function optimization routines has emerged known as genetic algorithms. The name is meant to convey the idea of mimicking nature and its processes of reproduction and survival of the fittest. Indeed, terminology such as population, generation, mating, parents, and offspring is scattered throughout the literature. Genetic algorithms are a popular, and ever-evolving genre of optimization. The following is meant only to be a general overview of characteristics present in many implementations. For a thorough discussion, see the work by Holland[196] and Goldberg.[197]

Genetic algorithms are a method of function minimization (or maximization), and are completely task independent. One has only to supply the evaluation function to be optimized. A high-level search is performed via an iterative procedure, in which each iteration is termed a generation. An initially random population of potential solutions is allowed to mate and produce offspring. The new generation is evaluated, ranked by performance, and a percentage of the population is eliminated from the gene pool. The remaining candidates compose the new population, which then repeat the procedure until the entire population contains solutions with superior performance. With each successive generation, the population is selected such that the performance of the members is reflected in their representation. For example, if a solution containing a particular trait performs twice as well as some other, the population will contain twice as many members with the beneficial trait.

Each member of the population is characterized by its binary representation. In order to sample the entire search space adequately, variations in the genetic content of the population must be introduced. These variations take the form of operators, and

perform the genetic function of mating. The number of possible operators is growing rapidly, and is too large to mention here. Two of the most important and basic operators are crossover and mutation. Crossover is achieved by picking a random point in two binary strings, and switching the string beyond this point. An example is

$$\begin{array}{l} p1 = 001 \wr 1100 \\ p2 = 100 \wr 0011 \end{array} \quad \text{crossover} \mapsto \quad \begin{array}{l} o1 = 001 \wr 0011 \\ o2 = 100 \wr 1100 \end{array} \tag{D.1}$$

where p is the parent, o is the offspring, and $\wr$ represents the randomly chosen crossover point. Mutation consists of picking a random digit in a string, and then flipping it. This can be seen below, where the randomly selected digit is in braces

$$p = 11101[0]0 \qquad \text{mutation} \mapsto \qquad o = 11101[1]0. \tag{D.2}$$

The purpose of the genetic operators is to constantly provide new species to the population, which could possibly outperform existing members. In doing this, the operators are sampling the entire space without prejudice, leading to a well-balanced rapidly converging optimization.

Genetic algorithms are effective and efficient means of sampling large spaces. However, their true utility is searching spaces that are multidimensional, noisy, or discontinuous. The heuristic nature of the algorithms prevents flawed decisions regarding search direction. Gradient methods are superior for simple searches in which initial conditions, or constraints begin the search in the appropriate area. However with little information about the problem, these methods are often trapped in local minima. Genetic algorithms have a much better chance to find the global minimum. Numerous packaged programs are available that can easily be implemented for a particular problem without requiring much knowledge about the inner workings of the code. The many beneficial features of genetic algorithms makes them attractive for scientific studies.

APPENDIX E
INTERBAND TRANSITIONS

In a layered semiconductor material, the z-axis is designated as the growth direction. Carriers feel the effects of confinement in this dimension because of the band gap misalignment of the different materials in the structure. In the perpendicular dimensions, carriers are considered as "free" leading to a wave function of the form $e^{ik_x x}\, e^{ik_y y}\, \phi(z)$. The in-plane carrier motion is described by a two-dimensional vector $\vec{r} = (x, y)$, and bi-dimensional wave vector $\vec{k} = (k_x, k_y)$. Assuming the lattice periodic function, $u^{\alpha}(\vec{r})$, is the same in both materials, a Schrödinger equation can be formulated giving the total wave function of the charge carriers as

$$|\Phi^{\alpha}_{n,k}\rangle = \frac{e^{i\vec{k}\cdot\vec{r}}}{\sqrt{A}}\, \phi^{\alpha}_{n}(z), \tag{E.1}$$

where α labels the carrier type, e for electrons and h for heavy holes.[198] As described previously, the portion of the wave function describing the confined dimension satisfies a one-dimensional, effective-mass Schrödinger equation

$$\left[-\frac{\hbar^2}{2m^*_{\alpha}}\frac{d^2}{dz^2} + V^{\alpha}(z) \pm eFz\right]\phi^{\alpha}_{n}(z) = E^{\alpha}_{n}\, \phi^{\alpha}_{n}(z), \tag{E.2}$$

where V is the QW potential, m^* is the effective mass in the growth dimension, and F is a dc field. The dc field interaction term is negative for holes and positive for electrons. The total energy expressions for the electrons and holes are

$$E^{e}_{n,k} = E^{e}_{n} + \frac{\hbar^2 k^2}{2m^*} \qquad \text{and} \qquad E^{h}_{n,k} = E^{h}_{n} - \frac{\hbar^2 k^2}{2m^*} \tag{E.3}$$

where $k^2 = k_x^2 + k_y^2$. Recall that the effective masses are not usually equivalent in the growth direction and the perpendicular dimensions for a given carrier type.

In the absence of a laser field, all of the dimensions of the wavefunction can be propagated independently. However, laser excitation couples them. Interband transitions, such as the ones modeled here ($e \leftarrow h$), have matrix elements of the form

$$\langle \Phi^{e}_{n,k} |\, \vec{\mu} \cdot \vec{\varepsilon} \,| \Phi^{h}_{n,k} \rangle, \tag{E.4}$$

where

$$\vec{\mu} = \hat{x}\,\mu_x + \hat{y}\,\mu_y + \hat{z}\,\mu_z. \tag{E.5}$$

The laser field takes the form

$$\vec{\varepsilon} = (\hat{y} + \hat{z})\varepsilon_x + (\hat{x} + \hat{z})\varepsilon_y + (\hat{x} + \hat{y})\varepsilon_z, \tag{E.6}$$

where

$$\varepsilon_i = E\cos(\omega t + k_i i) \qquad \text{and} \qquad i = x, y, z. \tag{E.7}$$

This gives the dot product as in Equation (E.4) as

$$\vec{\mu} \cdot \vec{\varepsilon} = (\mu_y + \mu_z)\varepsilon_x + (\mu_x + \mu_z)\varepsilon_y + (\mu_x + \mu_y)\varepsilon_z. \tag{E.8}$$

In this work, the field is assumed to propagate in the z direction so $\varepsilon_x = \varepsilon_y = 0$. Equation (E.4) becomes

$$\frac{1}{A} \int d\vec{r}\, e^{-i\vec{k}'\cdot\vec{r}} (\mu_x + \mu_y)\, e^{i\vec{k}\cdot\vec{r}} \int dz\, \phi^{e*}_{n}\, \varepsilon_z\, \phi^{h}_{n}, \tag{E.9}$$

where the electronic wave vector has been designated with a prime. It is reasonable to assume that the dipole moments in x and y are constants because those dimensions describe free particles that are allowed to reside anywhere in that plane. The selection rule stating that $k' = k$ is enforced to ensure energy conservation and vertical transitions, leading to the dipole matrix elements of the form

$$(\mu_x + \mu_y) \int dz\, \phi^{e*}_{n} \varepsilon_z\, \phi^{h}_{n}. \tag{E.10}$$

This transition term involves only the states in the confined dimension (envelope functions). It is identical to the expression one would obtain by treating only the z-dimension, with the field interaction term $(\mu_x + \mu_y)\,\varepsilon_z$ as the time-dependent perturbation. This term can be further simplified by assuming a $x-$polarized field, for example, which eliminates μ_y in the above expression. In addition, one can ignore the spatial variation in the field $(k_z z)$ by making a long-wavelength approximation. This yields transitions terms similar to

$$\mu_x \langle \phi_n^e | \phi_n^h \rangle E \cos(\omega t), \tag{E.11}$$

where a constant multiplies the overlap of the envelope functions, and scales the field. The preceding equation is a common form for interband transition terms.[145] The result of this expression is that the perpendicular dimensions are uncoupled, and the wave packet in the confined dimension can be propagated independently.

APPENDIX F
PULSE CHIRPING LIMITATIONS

Laser pulses can be described by two equivalent domains related to each other through a Fourier transform. In both domains, the pulse width is an important property. In the time domain, this quantity is the full width at half maximum (FWHM), while in the frequency domain it is the bandwidth (BW). A linear sweep of the laser frequency in time (pulse chirping) has no effect on the FWHM in the time domain. However, there is an inherent relationship between the chirp rate and the BW. Care must be taken when varying the chirp parameter to remain within the physical limitations of a given laser system, and not to create BW.

A complex laser pulse can be represented mathematically as

$$E(t) = E_o \exp\left[-\frac{(t-\bar{t})^2}{2\Gamma^2} - \frac{ib\,(t-\bar{t})^2}{2} - i\bar{\omega}\,(t-\bar{t})\right], \tag{F.1}$$

where E_o is the amplitude, $\bar{t}$ is the center time, Γ is the temporal width, b is the linear chirp, and $\bar{\omega}$ is the center frequency. The complex conjugate of $E(t)$, which is required to make the field real, is dropped from the following analysis in accord with the RWA (Appendix B). When referring to pulse width, one typically considers the pulse intensity given by

$$|E(t)|^2 = E_o^2 \exp\left[-\frac{(t-\bar{t})^2}{\Gamma^2}\right]. \tag{F.2}$$

The FWHM is found by setting Equation (F.2) equal to $E_o^2/2$, solving for $(t-\bar{t})$, and then multiplying by two. The amplitude factors on both sides of the equation cancel, which sets the exponential term equal to one half. The factor of two accounts for the total width of the Gaussian distribution. This leads to an expression for the

FWHM of the above pulse as

$$\text{FWHM} = \Gamma\sqrt{\ln 16}. \tag{F.3}$$

Setting $\bar{t} = 0$ and taking the Fourier transform of Equation (F.1) gives

$$E(\omega) = E_o^{\omega} \exp\left[-\frac{(\bar{\omega}-\omega)^2}{2\gamma^2} + \frac{i\eta(\bar{\omega}-\omega)^2}{2}\right], \tag{F.4}$$

where

$$E_o^{\omega} = E_o\sqrt{\frac{2\pi}{\left(\frac{1}{\Gamma^2} + ib\right)}}, \tag{F.5}$$

$$\gamma^2 = \left[\frac{1}{\Gamma^2} + (\Gamma b)^2\right], \qquad \text{and} \qquad \eta = \frac{b}{\left(\frac{1}{\Gamma^4} + b^2\right)}. \tag{F.6}$$

Using the same steps as for the time domain, the FWHM of $|E(\omega)|^2$ is

$$\text{BW} = \gamma\sqrt{\ln 16}, \tag{F.7}$$

where BW denotes the bandwidth. BW is a function of the pulse width and the linear chirp in the time domain. For transform-limited pulses ($b = 0$) the bandwidth is

$$\text{BW} = \frac{\sqrt{\ln 16}}{\Gamma_o}, \tag{F.8}$$

where Γ_o designates the temporal width of the original, transform-limited pulse.

Chirping a pulse should not increase or decrease the bandwidth. Therefore the bandwidth of the original laser pulse must equal the bandwidth after the chirp. Enforcing this condition (i.e., $1/\Gamma_0 = \gamma$) yields an expression for the chirp as

$$b = \pm\sqrt{\frac{1}{(\Gamma\,\Gamma_0)^2} - \frac{1}{\Gamma^4}}. \tag{F.9}$$

The maximum (minimum) of this function occurs when $\Gamma = \Gamma_0\sqrt{2}$ giving a maximum chirp rate of

$$b_{max} = \pm\frac{1}{2\,\Gamma_0^2}. \tag{F.10}$$

This is the largest value the linear chirp can be without changing the bandwidth of the corresponding transform-limited pulse.

REFERENCES

[1] S. A. Rice and M. Zhao, *Optical Control of Molecular Dynamics*, John Wiley & Sons, Inc., New York, NY, 2000.

[2] A. P. Heberle, W. W. Rühle, and K. Köhler, Phys. Stat. Sol. B **173**, 381 (1992).

[3] A. P. Heberle, W. W. Rühle, M. G. W. Alexander, and K. Köhler, Semicond. Sci. Technol. **7**, B421 (1992).

[4] P. Voisin, J. Bleuse, C. Bouche, S. Gaillard, C. Alibert, and A. Regreny, Phys. Rev. Lett. **61**, 1639 (1988).

[5] E. E. Mendez, F. Agulló-Rueda, and J. M. Hong, Phys. Rev. Lett. **60**, 2426 (1988).

[6] K. Leo, J. Shah, E. O. Göbel, T. C. Damen, S. Schmitt-Rink, W. Schäfer, and K. Köhler, Phys. Rev. Lett. **66**, 201 (1991).

[7] K. Leo, T. C. Damen, J. Shah, E. O. Göbel, and K. Köhler, Appl. Phys. Lett. **57**, 19 (1990).

[8] T. Dekorsy, P. Leisching, K. Köhler, and H. Kurz, Phys. Rev. B **50**, 8106 (1994).

[9] P. Leisching, P. H. Bolivar, W. Beck, Y. Dhaibi, F. Brüggermann, R. Schwedler, H. Kurz, K. Leo, and K. Köhler, Phys. Rev. B. **50**, 14389 (1994).

[10] H. G. Roskos, M. C. Nuss, J. Shah, K. Leo, D. A. B. Miller, A. M. Fox, S. Schmitt-Rink, and K. Köhler, Phys. Rev. Lett. **68**, 2216 (1992).

[11] P. C. M. Planken, M. C. Nuss, I. Brener, K. W. Goossen, M. S. C. Luo, S. L. Chuang, and L. Pfeiffer, Phys. Rev. Lett. **69**, 3800 (1992).

[12] C. Waschke, H. G. Roskos, R. Schwedler, K. Leo, H. Kurz, and K. Köhler, Phys. Rev. Lett. **70**, 3319 (1993).

[13] A. Bonvalet, J. Nagle, V. Berger, A. Migus, J.-L. Martin, and M. Joffe, Phys. Rev. Lett. **76**, 4392 (1996).

[14] C. P. Holfeld, F. Löser, M. Sudzius, K. Leo, D. M. Whittaker, and K. Köhler, Phys. Rev. Lett **81**, 874 (1998).

[15] S. T. Cundiff, A. Knorr, J. Feldmann, S. W. Koch, E. O. Göbel, and H. Nickel, Phys. Stat. Sol. B **188**, 307 (1995).

[16] R. Binder and M. Lindberg, Phys. Rev. B **61**, 2830 (2000).

[17] J. Faist, F. Capasso, D. L. Sivco, C. Sirtori, A. L. Hutchinson, and A. Y. Cho, Science **264**, 553 (1994).

[18] T. Ooogarah, H. Liu, E. Dupont, Z. Wasilewski, and M. Byloos, Semicond. Sci. Technol. **17**, L41 (2002).

[19] D. Hofstetter, M. Beck, and J. Faist, Appl. Phys. Lett. **81**, 2683 (2002).

[20] D. M. Mittleman, S. Hunsche, L. Boivin, and M. C. Nuss, Opt. Lett. **22**, 904.

[21] P. Y. Han, G. C. Han, and X.-C. Zhang, Opt. Lett. **25**, 242.

[22] S. D. Gunapala and S. V. Bandara, in *Semiconductors and Semimetals*, edited by H. C. Liu and F. Capasso, page 270, Academic Press, San Diego, 2000.

[23] K. Tajima, S. Nakamura, and Y. Sugimoto, Appl. Phys. Lett. **67**, 3709.

[24] O. Wada, Opt. Quantum Electron. **32**, 453.

[25] E. Pazy, I. D'Amico, P. Zanardi, and F. Rossi, Phys. Rev. B **64**, 195320 (2001).

[26] E. Biolatti, R. Iotti, P. Zanardi, and F. Rossi, Phys. Rev. Lett. **85**, 5647 (2000).

[27] Z. Kis and R. Renzoni, Phys. Rev. A **65**, 032318 (2002).

[28] J. Roland and N. Cerf, Phys. Rev. A **65**, 042308 (2002).

[29] D. J. Tannor and S. A. Rice, J. Chem. Phys. **83**, 5013 (1985).

[30] D. J. Tannor, R. Kosloff, and S. A. Rice, J. Chem. Phys. **85**, 5805 (1986).

[31] A. Messiah, *Quantum Mechanics*, Wiley & Sons, New York, 1958.

[32] E. J. Heller, J. Chem. Phys. **62**, 1544 (1975).

[33] E. J. Heller, Acc. Chem. Res. **14**, 368 (1981).

[34] E. J. Heller, R. L. Sundberg, and D. Tannor, J. Phys. Chem. **86**, 1822 (1982).

[35] S. Y. Lee and E. J. Heller, J. Chem. Phys. **71**, 4777 (79).

[36] T. Baumert, J. Helbing, and G. Gerber, Adv. Chem. Phys. , 47 (1997).

[37] T. Baumert, M. Grossner, R. Thalweiser, and G. Gerber, Phys. Rev. Lett. **67**, 3753 (1991).

[38] E. D. Potter, J. L. Herek, S. Pedersen, Q. Liu, and A. H. Zewail, Nature **355**, 66 (1992).

[39] J. L. Herek, A. Materny, and A. H. Zewail, Chem. Phys. Lett. **228**, 15 (1994).

[40] M. Shapiro and P. Brumer, J. Chem. Phys. **84**, 4103 (1986).

[41] P. Brumer and M. Shapiro, Chem. Phys. Lett. **126**, 541 (1986).

[42] C. K. Chan, P. Brumer, and M. Shapiro, J. Chem. Phys. **94**, 2688 (1991).

[43] C. Chen, Y. Y. Yin, and D. S. Elliott, Phys. Rev. Lett. **64**, 507 (1990).

[44] C. Chen and D. S. Elliott, Phys. Rev. Lett. **65**, 1737 (1990).

[45] S. M. Park, S. P. Lu, and R. J. Gordon, J. Chem. Phys. **94**, 8622 (1991).

[46] S. Lu, S. M. Park, Y. Xie, and R. J. Gordon, J. Chem. Phys. **96**, 6613 (1996).

[47] V. D. Kleiman, L. Zhu, X. Li, and R. J. Gordon, J. Chem. Phys. **102**, 5863 (1995).

[48] V. D. Kleiman, L. Zhu, J. Allen, and R. J. Gordon, J. Chem. Phys. **103**, 10800 (1995).

[49] L. C. Zhu, V. Kleiman, X. N. Li, S. P. Lu, K. Trentelman, and R. J. Gordon, Science **270**, 77 (1995).

[50] L. Zhu, K. Suto, J. A. Fiss, R. Wada, T. Seideman, and R. J. Gordon, Phys. Rev. Lett. **79**, 4108 (1997).

[51] J. A. Fiss, L. C. Zhu, K. Suto, G. Z. He, and R. J. Gordon, Chem. Phys. **48**, 601 (1998).

[52] A. P. Peirce, M. A. Dahleh, and H. Rabitz, Phys. Rev. A **37**, 4950 (1988).

[53] M. Zhao and S. A. Rice, J. Chem. Phys. **95**, 2465 (1991).

[54] R. Demiralp and H. Rabitz, Phys. Rev. A **47**, 809 (1993).

[55] M. Dahleh, A. P. Peirce, and H. Rabitz, Phys. Rev. A **42**, 1065 (1990).

[56] V. Ramakrishna, M. V. Salapaka, M. Dahleh, H. Rabitz, and A. Peirce, Phys. Rev. A **51**, 960 (1995).

[57] P. Gross, D. Neuhauser, and H. Rabitz, J. Chem. Phys. **96**, 2834 (1992).

[58] R. Kosloff, S. A. Rice, P. Gaspard, S. Tersigni, and D. J. Tannor, Chem. Phys. **139**, 201 (1989).

[59] J. Somlói, V. A. Kazakov, and D. J. Tannor, Chem. Phys. **172**, 85 (1993).

[60] I. R. Sola, J. Santamaria, and D. J. Tannor, J. Phys. Chem. A **102**, 4301 (1998).

[61] W. Zhu, J. Botina, and H. Rabitz, J. Chem. Phys. **108**, 1953 (1998).

[62] W. Zhu and H. Rabitz, J. Chem. Phys. **109**, 385 (1998).

[63] J. M. Geremia, W. Zhu, and H. Rabitz, J. Chem. Phys. **113**, 10841 (2000).

[64] K. Sundermann and R. Vivie-Riedle, J. Chem. Phys. **110**, 1896 (1999).

[65] Y. J. Yan, R. E. Gillilan, R. M. Whitnell, K. R. Wilson, and S. Mukamel, J. Phys. Chem. **97**, 2320 (1993).

[66] J. L. Krause, R. M. Whitnell, K. R. Wilson, Y. J. Yan, and S. Mukamel, J. Chem. Phys. **99**, 6562 (1993).

[67] B. Kohler, V. V. Yakovlev, J. Che, J. L. Krause, M. Messina, K. R. Wilson, N. Schwentner, R. M. Whitnell, and Y. J. Yan, Phys. Rev. Lett. **74**, 3360 (1995).

[68] J. L. Krause, M. Messina, K. R. Wilson, and Y. J. Yan, J. Phys. Chem. **99**, 13736 (1995).

[69] P. Gross, H. Singh, H. Rabitz, K. Mease, and G. M. Huang, Phys. Rev. A **47**, 4593 (1993).

[70] Z. Lu and H. Rabitz, J. Phys. Chem. **99**, 1995 (1995).

[71] Y. Chen, P. Gross, V. Ramakrishna, H. Rabitz, and K. Mease, J. Chem. Phys. **102**, 8001 (1995).

[72] R. Kosloff, A. D. Hammerich, and D. J. Tannor, Phys. Rev. Lett **69**, 2172 (1992).

[73] V. S. Malinovsky, C. Meier, and D. J. Tannor, Chem. Phys. **221**, 67 (1997).

[74] V. S. Malinovsky and D. J. Tannor, Phys. Rev. A **56**, 4929 (1997).

[75] R. S. Judson and H. Rabitz, Phys. Rev. Lett. **68**, 1500 (1992).

[76] G. J. Tóth, A. Lőrincz, and H. Rabitz, J. Chem. Phys. **101**, 3715 (1994).

[77] M. Q. Phan and H. Rabitz, Chem. Phys. **217**, 389 (1997).

[78] M. Q. Phan and H. Rabitz, J. Chem. Phys. **110**, 34 (1999).

[79] T. Feurer, A. Glaß, T. Rozgonyi, R. Sauerbrey, and G. Szabo, Chem. Phys. **267**, 223 (2001).

[80] C. J. Bardeen, V. V. Yakovlev, K. R. Wilson, S. D. Carpenter, P. M. Weber, and W. S. Warren, Chem. Phys. Lett. **280**, 151 (1997).

[81] A. Assion, T. Baumert, M. Bergt, T. Brixner, B. Kiefer, V. Seyfried, M. Strehle, and G. Gerber, Science **282**, 919 (1998).

[82] C. Daniel, J. Full, L. González, C. Kaposta, M. Krenz, C. Lupulescu, J. Manz, S. Minemoto, M. Oppel, P. Rosendo-Francisco, S. Vajda, and L. Wöste, Chem. Phys. **267**, 247 (2001).

[83] T. C. Weinacht, J. Ahn, and P. H. Bucksbaum, Nature **397**, 233 (1999).

[84] B. J. Pearson, J. L. White, T. C. Weinacht, and P. H. Bucksbaum, Phys. Rev. A **63**, 63412 (2001).

[85] R. J. Levis, G. M. Menkir, and H. Rabitz, Science **292**, 709 (2001).

[86] U. Gaubatz, P. Rudecki, S. Schiemann, and K. Bergmann, J. Chem. Phys. **92**, 5363 (1990).

[87] K. Bergmann and B. W. Shore, in *Molecular dynamics and spectroscopy by stimulated emission pumping*, edited by H. L. Dai and R. W. Field, pages 315–373, World Scientific, Singapore, 1995.

[88] K. Bergmann, H. Theuer, and B. W. Shore, Rev. Mod. Phys. **70**, 1003 (1998).

[89] D. Bohm, *Quantum Theory*, Prentice-Hall, New Jersey, 1951.

[90] L. Allen and J. H. Eberly, *Optical Resonance and Two-Level Atoms*, John Wiley & Sons, Inc., New York, NY, 1975.

[91] T. Halfmann and K. Bergmann, J. Chem. Phys. **104**, 7068 (1996).

[92] J. Oreg, F. T. Hioe, and J. H. Eberly, Phys. Rev. A **29**, 690 (1984).

[93] B. W. Shore, K. Bergmann, J. Oreg, and S. Rosenwaks, Phys. Rev. A **44**, 7442 (1991).

[94] G. W. Coulston and K. Bergmann, J. Chem. Phys. **96**, 3467 (1992).

[95] J. Martin, B. W. Shore, and K. Bergmann, Phys. Rev. A **54**, 1556 (1996).

[96] M. M. T. Loy, Phys. Rev. Lett. **32**, 814 (1974).

[97] M. M. T. Loy, Phys. Rev. Lett. **41**, 473 (1978).

[98] S. Chelkowski, A. Bandrauk, and P. B. Corkum, Phys. Rev. Lett. **65**, 2355 (1990).

[99] A. Chelkowski and A. D. Bandrauk, J. Chem. Phys. **99**, 4279 (1993).

[100] J. S. Melinger, A. Hariharan, S. R. Gandhi, and W. S. Warren, J. Chem. Phys. **95**, 2210 (1991).

[101] J. S. Melinger, S. R. Gandhi, A. Hariharan, D. Goswami, and W. S. Warren, J. Chem. Phys. **101**, 6439 (1994).

[102] Y. B. Band and O. Magnes, Phys. Rev. A **50**, 584 (1994).

[103] Y. B. Band, Phys. Rev. A **50**, 5046 (1994).

[104] I. R. Solá, V. S. Malinovsky, B. Y. Chang, and K. Bergmann, Phys. Rev. A **59**, 4494 (1999).

[105] B. M. Garraway and K. A. Suominen, Phys. Rev. Lett. **80**, 932 (1998).

[106] I. R. Solá, J. Santamaría, and V. S. Malinovsky, Phys. Rev. A **61**, 043413 (2000).

[107] B. Y. Chang, I. R. Solá, J. Santamaría, V. S. Malinovsky, and J. L. Krause, J. Chem. Phys. , 8820 (2001).

[108] B. Y. Chang, I. R. Solá, V. S. Malinovsky, and J. Santamaría, J. Chem. Phys. **113**, 4901 (2000).

[109] M. Shapiro and P. Brumer, J. Chem. Phys. **95**, 8658 (1991).

[110] Y. Fujimura, L. González, K. Hoki, J. Manz, and Y. Ohtsuki, Chem. Phys. Lett. **306**, 1 (1999).

[111] E. Charron, A. Giusti-Suzor, and F. H. Mies, Phys. Rev. Lett **75**, 2815 (1995).

[112] M. Leibscher and I. S. Averbukh, Phys. Rev. A **63**, 43407 (2001).

[113] C. M. Dion, A. D. Bandrauk, O. Atabek, A. Keller, H. Umeda, and Y. Fujimura, Chem. Phys. Lett. **302**, 215 (1999).

[114] K. Hoki and Y. Fujimura, Chem. Phys. **267**, 187 (2001).

[115] M. V. Korolkov and G. K. Paramonov, Phys. Rev. A **57**, 4998 (1998).

[116] I. V. Andrianov and G. K. Paramonov, Phys. Rev. A **59**, 2134 (1999).

[117] M. V. Korolkov and G. K. Paramonov, Phys. Rev. A **56**, 3860 (1997).

[118] E. M. Hiller and J. A. Cina, J. Chem. Phys. **105**, 3419 (1996).

[119] M. Messina, K. R. Wilson, and J. L. Krause, J. Chem. Phys. **104**, 173 (1996).

[120] C. J. Bardeen, J. Che, K. R. Wilson, V. V. Yakovlev, A. P. Apkarian, C. C. Martens, R. Zadoyan, B. Kohler, and M. Messina, J. Chem. Phys. **106**, 8486 (1997).

[121] A. P. Heberle, J. J. Baumberg, and K. Köhler, Phys. Rev. Lett. **75**, 2598 (1995).

[122] A. P. Heberle, J. J. Baumberg, T. Kuhn, and K. Köhler, Phys. B **272**, 360 (1999).

[123] T. Dekorsy, W. Kütt, T. Pfeifer, and H. Kurz, Europhys. Lett. **23**, 223 (1993).

[124] M. U. Wehner, M. H. Ulm, D. S. Chemla, and M. Wegener, Phys. Rev. Lett. **80**, 1992 (1998).

[125] A. Bartels, T. Dekorsy, H. Kurz, and K. Köhler, Appl. Phys. Lett. **72**, 2844 (1998).

[126] X. Hu and W. Pötz, Phys. Rev. Lett. **82**, 3116 (1999).

[127] P. C. M. Planken, I. Brener, M. C. Nuss, M. S. C. Luo, and S. L. Chuang, Phys. Rev. B. **48**, 4903 (1993).

[128] M. S. C. Luo, S. L. Chuang, P. C. M. Planken, I. Brener, and M. C. Nuss, Phys. Rev. B. **48**, 11043 (1993).

[129] I. Brener, P. C. M. Planken, M. C. Nuss, M. S. C. Luo, S. L. Chuang, L. Pfeiffer, D. E. Leaird, and A. M. Weiner, J. Opt. Soc. Am. B **11**, 2457 (1994).

[130] A. M. Weiner, J. Opt. Soc. Am. B **11**, 2480 (1994).

[131] W. Pötz, App. Phys. Lett. **72**, 3002 (1998).

[132] E. Dupont, P. B. Corkum, H. C. Liu, M. Buchanan, and Z. R. Wasilewski, Phys. Rev. Lett. **74**, 3596 (1995).

[133] R. Atanasov, A. Hache, J. L. P. Hughes, H. M. van Driel, and J. Sipe, Phys. Rev. Lett. **76**, 1703 (1996).

[134] A. Haché, Y. Kostoulas, R. Atanasov, J. L. P. Hughes, J. E. Sipe, and H. M. van Driel, Phys. Rev. Lett. **78**, 306 (1997).

[135] A. Dargys, Phys. Stat. Sol. B **219**, 401 (2000).

[136] J. L. Krause, D. H. Reitze, G. D. Sanders, A. V. Kuznetsov, and C. J. Stanton, Phys. Rev. B **57**, 9024 (1998).

[137] J. Kunde, B. Baumann, S. Arlt, F. Morier-Genoud, U. Siegner, and U. Keller, Appl. Phys. Lett. **77**, 924 (2000).

[138] W. Pötz, Phys. Rev. Lett. **79**, 3262 (1997).

[139] W. Pötz, Appl. Phys. Lett. **71**, 395 (1997).

[140] X. Hu and W. Pötz, Phys. Stat. Sol. **204**, 350 (1997).

[141] N. H. Bonadeo, J. Erland, D. Gammon, D. Park, D. S. Katzer, and D. G. Steel, Science **282**, 1473 (1998).

[142] U. Hohenester, F. Troiani, E. Molinari, G. Panzarini, and C. Macchiavello, Appl. Phys. Lett. **77**, 1864 (2000).

[143] J. L. Krause, Adv. Quantum Chem. **35**, 249 (1999).

[144] G. Bastard, *Wave Mechanics Applied to Semiconductor Heterostructures*, Halsted Press, New York, NY, 1988.

[145] A. V. Kuznetsov, G. D. Sanders, and C. J. Stanton, Phys. Rev. B **52**, 12045 (1995).

[146] J. C. Light, I. P. Hamilton, and J. V. Lill, J. Chem. Phys. **82**, 1400 (1985).

[147] W. S. Warren, H. Rabitz, and M. Dahleh, Science **259**, 1581 (1993).

[148] D. J. Tannor and S. A. Rice, Adv. Chem. Phys. **70**, 441 (1988).

[149] M. Shapiro and P. Brumer, Int. Rev. Phys. Chem. **13**, 187 (1994).

[150] J. L. Krause, R. M. Whitnell, K. R. Wilson, and Y. J. Yan, in *Femtosecond Chemistry*, edited by J. Manz and L. Wöste, pages 743–779, VCH, Weinheim, 1995.

[151] J. D. Grefenstette, GENESIS v5.0, Copyright (c), 1990.

[152] K. L. Shuford and J. L. Krause, Int. J. Quant. Chem. **77**, 393 (2000).

[153] E. J. Heller, J. Chem. Phys. **64**, 63 (1976).

[154] R. B. Gerber, M. A. Ratner, and V. Buch, Chem. Phys. Lett. **91**, 173 (1982).

[155] N. Makri and W. H. Miller, J. Chem. Phys. **86**, 1451 (1987).

[156] N. Makri and W. H. Miller, J. Chem. Phys. **87**, 5781 (1987).

[157] R. H. Bisseling, R. Kosloff, R. B. Gerber, M. A. Ratner, L. Gibson, and C. Cerjan, J. Chem. Phys. **87**, 2760 (1987).

[158] M. Messina and R. D. Coalson, J. Chem. Phys. **90**, 4015 (1989).

[159] P. Aceituno, H. Cruz, and A. Hernández-Cabrera, Phys. Rev. B **54**, 17677 (1996).

[160] A. Hernández-Cabrera, Phys. E **4**, 65 (1999).

[161] K. Leo, Semicond. Sci.Tech. **13**, 249 (1998).

[162] A. M. Fox, D. A. B. Miller, G. Livescu, J. E. Cunningham, J. E. Henry, and W. Y. Jan, Phys. Rev. B. **42**, 1841 (1990).

[163] D. A. B. Miller, D. S. Chemla, T. C. Damen, A. C. Gossard, W. Wiegmann, T. H. Wood, and C. A. Burrus, Phys. Rev. B **32**, 1043 (1985).

[164] G. Bastard, E. E. Mendez, L. L. Chang, and L. Esaki, Phys. Rev. B **26**, 1974 (1982).

[165] C. Leforestier, R. H. Bisseling, C. Cerjan, M. D. Feit, R. A. Friesner, A. Guldberg, A. Hammerich, G. Jolicard, W. Karrlein, H. Meyer, N. Lipkin, O. Roncero, and R. Kosloff, J. Comput. Phys. **94**, 59 (1991).

[166] R. Kosloff, J. Phys. Chem. **92(8)**, 2087 (1988).

[167] K. L. Shuford and J. L. Krause, J. Appl. Phys. **91**, 6533 (2002).

[168] R. C. Miller, D. A. Kleinman, W. T. Tsang, and A. C. Gossard, Phys. Rev. B **24**, 1134 (1981).

[169] J. Shah, *Ultrafast Spectroscopy of Semiconductors and Semiconductor Nanostructures*, Springer, New York, NY, 1999.

[170] T. Meier, G. von Plessen, P. Thomas, and S. W. Koch, Phys. Rev. Lett. **73**, 902 (1994).

[171] P. Leisching, T. Dekorsy, H. J. Bakker, and H. Kurz, Phys. Rev. B **51**, 18015 (1995).

[172] L. Schultheis, A. Honold, J. Kuhl, K. Köhler, and C. W. Tu, Phys. Rev. B **34**, 9027 (1986).

[173] D. H. Auston, K. P. Cheung, and P. R. Smith, Appl. Phys. Lett. **45**, 284 (1984).

[174] K. L. Shuford and J. L. Krause, J. Phys. Chem. A **106**, 10818 (2002).

[175] C. Fattinger and D. Grischkowlky, Appl. Phys. Lett. **53**, 1480 (1988).

[176] B. B. Hu, J. T. Darrow, X. C. Zhang, and D. H. Auston, Appl. Phys. Lett. **56**, 886 (1990).

[177] A. M. Weiner, J. P. Heritage, and E. M. Kirschner, J. Opt. Soc. Am. B **5**, 1563 (1988).

[178] C. W. Hillegas, J. X. Tull, D. Goswami, D. Strickland, and W. Warren, Opt. Lett. **19**, 737 (1994).

[179] M. M. Wefers and K. A. Nelson, Opt. Lett. **18**, 2032 (1993).

[180] P. W. Milonni and J. H. Eberly, *Lasers*, John Wiley & Sons, Inc., New York, NY, 1988.

[181] J. N. Heyman, R. Kersting, and K. Unterrainer, Appl. Phys. Lett. **72**, 644 (1998).

[182] Y. Liu, S. Park, and A. M. Weiner, Opt. Lett. **21**, 1762 (1996).

[183] A. S. Weling, B. B. Hu, N. M. Froberg, and D. H. Auston, Appl. Phys. Lett. **64**, 137 (1994).

[184] V. van Exter, C. Fattinger, and D. Grischkowsky, Appl. Phys. Lett. **55**, 337 (1989).

[185] D. You, R. R. Jones, D. Dykaar, and P. Bucksbaum, Opt. Lett. **18**, 290 (1993).

[186] C. Raman, M. F. DeCamp, and P. H. Bucksbaum, Opt. Express **1**, 186 (1997).

[187] J. S. Melinger, S. R. Gandhi, A. Hariharan, J. X. Tull, and W. S. Warren, Phys. Rev. Lett. **68**, 2000 (1992).

[188] S. Kallush and Y. B. Band, Phys. Rev. A **61**, 41401 (2000).

[189] E. E. Aubanel and A. D. Bandrauk, J. Phys. Chem. **97**, 12620 (1993).

[190] A. Bandrauk, editor, *Molecules in Laser Fields*, Marcel Dekker, Inc., New York, NY, 1994.

[191] R. Binder and M. Lindberg, Phys. Rev. Lett. **81**, 1477 (1998).

[192] K. L. Shuford and J. L. Krause, J. Phys. D **36**, 439 (2003).

[193] J. J. Baumberg, A. P. Heberle, K. Köhler, and K. Ploog, J. Opt. Soc. Am. B **13**, 1246 (1996).

[194] J.-W. Wu, Solid State Comm. **67**, 911.

[195] S. Adachi, J. Appl. Phys. **58**, R1 (1985).

[196] J. H. Holland, *Adaptation in Natural and Artificial Systems*, University of Michigan Press, Ann Arbor, 1975.

[197] D. E. Goldberg, *Genetic Algorithms in Search, Optimization, and Machine Learning*, Addison-Wesley, 1989.

[198] M. Helm, in *Semiconductors and Semimetals*, edited by H. C. Liu and F. Capasso, page 1, Academic Press, San Diego, 2000.

BIOGRAPHICAL SKETCH

Kevin L. Shuford was born on February 3rd 1976 in Clifton Forge, Virginia. He was the first and only son of Charles and Cheryll Shuford, following two daughters. His early years were spent in the mountain town of Covington, and later in the coastal area of Williamsburg. When Kevin was 5 years old, he and the family moved to Wilmington, North Carolina. The beach life was part of his daily routine growing up. He enjoyed activities such as surfing, fishing, boating, and water skiing. Other sports were also a central theme. Kevin played organized baseball and soccer, and also enjoyed basketball, football, golf, mountain biking, and skateboarding.

Kevin's primary education consisted of elementary, middle, and high school at College Park, D.C. Virgo, and New Hanover, respectively. After completing high school, he attended the University of North Carolina at Wilmington. Originally, Kevin was to transfer to another university to follow in his father's footsteps and study engineering. These plans changed after completing a chemistry course that he found particularly interesting. Kevin became involved in undergraduate chemistry research with Dr. Michael Messina, and found the experience extremely gratifying. He never transferred, and received a B.S. in Chemistry from UNCW in 1998.

Kevin's education continued in the chemistry graduate program at the University of Florida. He found physical chemistry most appealing, and spent the next 5 years studying dynamics in semiconductors under the direction of Dr. Jeffrey Krause. In 2003, Kevin received a Ph.D. in Chemistry. Kevin is currently continuing his research career at the University of Florida, and is actively pursuing several possible employment opportunities.

I certify that I have read this study and that in my opinion it conforms to acceptable standards of scholarly presentation and is fully adequate, in scope and quality, as a dissertation for the degree of Doctor of Philosophy.

Jeffrey L. Krause, Chair
Associate Professor of Chemistry

I certify that I have read this study and that in my opinion it conforms to acceptable standards of scholarly presentation and is fully adequate, in scope and quality, as a dissertation for the degree of Doctor of Philosophy.

N. Yngve Öhrn
Professor of Chemistry

I certify that I have read this study and that in my opinion it conforms to acceptable standards of scholarly presentation and is fully adequate, in scope and quality, as a dissertation for the degree of Doctor of Philosophy.

Erik B. Deumens
Scientist of Chemistry

I certify that I have read this study and that in my opinion it conforms to acceptable standards of scholarly presentation and is fully adequate, in scope and quality, as a dissertation for the degree of Doctor of Philosophy.

John R. Reynolds
Professor of Chemistry

I certify that I have read this study and that in my opinion it conforms to acceptable standards of scholarly presentation and is fully adequate, in scope and quality, as a dissertation for the degree of Doctor of Philosophy.

David H. Reitze
Professor of Physics

This dissertation was submitted to the Graduate Faculty of the Department of Chemistry in the College of Liberal Arts and Sciences and to the Graduate School and was accepted as partial fulfillment of the requirements for the degree of Doctor of Philosophy.

August 2003

Dean, Graduate School